MEMS GYROSCOPES WITH CAPACITIVE ENHANCEMENT

A THESIS SUBMITTED TO
THE GRADUATE SCHOOL OF NATURAL AND APPLIED SCIENCES
OF
MIDDLE EAST TECHNICAL UNIVERSITY

BY

EMRE ERSOY

IN PARTIAL FULFILLMENT OF THE REQUIREMENTS
FOR
THE DEGREE OF MASTER OF SCIENCE
IN
MECHANICAL ENGINEERING

FEBRUARY 2022

Approval of the thesis:

MEMS GYROSCOPES WITH CAPACITIVE ENHANCEMENT

submitted by **EMRE ERSOY** in partial fulfillment of the requirements for the degree of **Master of Science** in **Mechanical Engineering, Middle East Technical University** by,

Prof. Dr. Halil Kalıpçılar
Dean, Graduate School of **Natural and Applied Sciences** ________________

Prof. Dr. M. A. Sahir Arıkan
Head of the Department, **Mechanical Engineering** ________________

Assoc. Prof. Dr. Kıvanç Azgın
Supervisor, **Mechanical Engineering, METU** ________________

Examining Committee Members:

Assoc. Prof. Dr. Ender Yıldırım
Mechanical Engineering, METU ________________

Assoc. Prof. Dr. Kıvanç Azgın
Mechanical Engineering, METU ________________

Prof. Dr. Haluk Külah
Electrical and Electronics Eng., METU ________________

Assist. Prof. Dr. Hakan Çalışkan
Mechanical Engineering, METU ________________

Assist. Prof. Dr. Erdinç Tatar
Electrical and Electronics Eng., Bilkent University ________________

Date: 08.02.2022

I hereby declare that all information in this document has been obtained and presented in accordance with academic rules and ethical conduct. I also declare that, as required by these rules and conduct, I have fully cited and referenced all material and results that are not original to this work.

Name Last name : Emre Ersoy

Signature :

ABSTRACT

MEMS GYROSCOPES WITH CAPACITIVE ENHANCEMENT

Ersoy, Emre
Master of Science, Mechanical Engineering
Supervisor: Assoc. Prof. Kıvanç Azgın

February 2022, 95 pages

This thesis reports development of a novel capacitive enhancement approach for MEMS gyroscopes with in-plane drive motion. The study includes design, fabrication, post-processing, and test steps of the MEMS device and enhancement setup. The gyroscope consists of two identical masses which were connected by a diamond shape coupling mechanism. This coupling mechanism provides mode ordering in drive mode. The gyroscope is designed to be mode-matched in order to achieve higher displacements in the sense mode. Therefore, the sense mode resonance frequency is selected higher than drive mode so that the dedicated frequency tuning electrodes can adjust the frequencies to match them. Beside from that, to decrease the mechanical noise the structure is designed to be larger and thicker than the conventional gyroscopes with a boosted proof mass. Despite the thicker structure providing larger capacitive area, the aspect ratio in the silicon etching limits the minimum capacitive gap and obstruct reaching higher signal-to-noise ratio (SNR) values. Therefore, a post-processing approach is developed to eliminate the minimum achievable gap limitation. Both drive and sense electrodes are designed to be within the limits of the aspect ratio and both drive and sense

electrodes are post-processed after the fabrication. The designed structure is verified by performing simulations in the COMSOL environment.

The fabrication of the gyroscope is conducted in the METU MEMS Center. The device layer of an SOI wafer is micromachined and bonded to a substrate wafer which provides bonding regions (anchors) and electrode wiring. The fabricated devices have a footprint of 48 mm x 21 mm with a 400 µm thickness. The drive capacitive gaps of the gyroscopes are tested before the post-processing in a vacuum environment with the constructed read-out electronics. The quality factors are between 700-800 under 0.075 mTorr for the drive mode. After the capacitive enhancement, the 25 µm capacitive gaps of the sense electrodes are enhanced to 1.4 µm and drive fingers are engaged with an average gap of 5.5 µm. As a result of the capacitive enhancement process, the achieved capacitance increase in the sense mode is approximately 11.5 times with respect to the initial value.

Keywords: Gyroscope, Post-processing, Capacitive enhancement.

ÖZ

KAPASİTİF İYİLEŞTİRİLMİŞ MEMS DÖNÜÖLÇERLER

Ersoy, Emre
Yüksek Lisans, Makina Mühendisliği
Tez Yöneticisi: Doç. Dr. Kıvanç Azgın

Şubat 2022, 95 sayfa

Bu tez, düzlem içi tahrik hareketine sahip MEMS dönüölçerleri için yeni bir kapasitif iyileştirme yaklaşımının geliştirildiğini bildirmektedir. Çalışma, MEMS cihazının tasarım, üretim, üretim sonrası işlem ve test adımlarını ve kapasitif iyileştirme düzeneğini içermektedir. Dönülöçer, elmas şeklindeki bir bağlaşım mekanizması ile birbirine bağlanan iki özdeş kütleden oluşur. Bu bağlaşım mekanizması, sürüş modunda mod düzenlemesi sağlar. Dönüölçer, algılama modunda daha yüksek deplasmanlar elde etmek için mod eşlenebilir olacak şekilde tasarlanmıştır. Bu nedenle, algılama modu rezonans frekansı, sürüş modundan daha yüksek seçilmiş, böylece frekans ayarlama elektrotları, frekansları birbirine eşleyecek şekilde ayarlayabilir. Bunun yanı sıra, mekanik gürültüyü azaltmak için yapı, arttırılmış sismik kütlesi ile geleneksel dönüölçerlerden daha büyük ve kalın olacak şekilde tasarlanmıştır. Daha büyük kapasitif alan sağlayan daha kalın yapıya rağmen, silikon aşındırmadaki en boy oranı, minimum kapasitif boşluğu sınırlar ve daha yüksek sinyal-gürültü oranı (SNR) değerlerine ulaşılmasını engeller. Bu nedenle, elde edilebilecek minimum boşluk sınırlamasını ortadan kaldırmak için bir üretim sonrası işlem yaklaşımı geliştirilmiştir. Hem sürüş hem de algılama elektrotları, en-boy oranı sınırları içinde olacak şekilde tasarlanmış ve üretimden sonra üretim sonrası işlem

gerçekleştirilmiştir. Tasarlanan yapı, COMSOL ortamında simülasyonlar yapılarak doğrulanmıştır.

Dönüölçerin üretimi ODTÜ MEMS Merkezi'nde gerçekleştirilmektedir. Bir SOI alttaşı cihaz katmanı olarak işlenir ve yapıştırma bölgeleri (ankorlar) ve elektrot kablajı sağlayan bir alt tabaka alttaşına bağlanır. Üretilen cihazlar 48 mm x 21 mm ayak izine ve 400 μm kalınlığa sahiptir. Dönüölçerlerin sürüş modu kapasitif boşlukları, oluşturulmuş okuma elektroniği devreleri ile vakum ortamında üretim sonrası işlemden önce test edilmiştir. Kalite faktörü, sürüş modu için sırasıyla 0.075 mTorr altında 700-800 arasında bulunmuştur. Üretim sonrası işlem gerçekleştirildikten sonra, algılama elektrotlarının 25 μm olan kapasitif boşlukları 1,4 μm'ye düşürülmüş ve sürüş parmak yapıları ortalama 5,5 μm boşlukla devreye alınmıştır. Sonuç olarak, algılama elektrotlarında başlangıçtaki seviyeye göre yaklaşık 11,5 kat kapasitans artışı gözlemlenmiştir.

Anahtar Kelimeler: Dönüölçer, Üretim sonrası işlem, Kapasitif iyileştirme.

"What we do in life echoes in eternity…"

Maximus Decimus Meridius

To my lovely wife, Nisa.

ACKNOWLEDGMENTS

Firstly, I would like to thank to my thesis advisor Assoc. Prof. Dr. Kıvanç Azgın who supported and guided me during this research.

I am glad to have technical assistance and advices from Orhan Akar, special thanks to his help for this work. Besides from that, I also appreciate METU MEMS CENTER employees Ahmet Murat Yağcı, Murat Demirpolat, Ertuğ Şimşek, Baran Utku Tekin, Taylan Töral for their effort. Especially, thanks to Büşra Erdoğan and Batuhan Beşcan for their great support and effort.

I would like to thank to my colleagues; Ahmet Gülsaran, Atakan Tevlek, Bahar Atik, Bekir Gürel Dimez, Buğrahan Gülcüler, Emrah Dirican, Meltem Okan, for their assistance.

Lastly, I am very grateful to my family with their endless support in my life. Special thanks to Elif Nisa Ersoy for her infinite support, patience, and love.

TABLE OF CONTENTS

ABSTRACT v

ÖZ vii

ACKNOWLEDGMENTS x

TABLE OF CONTENTS xi

LIST OF TABLES xiii

LIST OF FIGURES xiv

1 INTRODUCTION 1

1.1 Overview of Capacitive Enhancement Processes 1

1.1.1 In-Process Methods 3

1.1.2 Post-Process Methods 5

1.2 Gyroscope Studied in This Thesis 7

1.3 Research Objectives and Thesis Organization 11

2 VIBRATORY MEMS GYROSCOPE THEORY 13

2.1 Mechanical Model of Gyroscope 13

2.2 Mechanics of Drive Mode 14

2.3 Mechanics of Sense Mode with Coriolis Coupling 17

2.4 Electrostatic Actuation and Sensing 23

2.5 Summary 32

3 DESİGN OF VIBRATORY MEMS GYROSCOPE 33

3.1 Flexure Elements 33

3.2 Electrostatic Force Compensation and Tuning Electrodes 38
3.2.1 Forced Feedback Electrodes 38
3.2.2 Quadrature Cancellation Electrodes 38
3.2.3 Sense Frequency Tuning Electrodes 39
3.2.4 Drive Frequency Tuning Electrodes 40
3.3 Finite Element Analysis 41
3.4 Fabrication 44
3.5 Summary 59
4 CAPACITIVE ENHANCEMENT PROCESSING 61
4.1 Capacitive Enhancement Methodology 61
4.1.1 Sense Mode Capacitive Enhancement 65
4.1.2 Drive Mode Capacitive Enhancement 68
4.2 Summary 69
5 TEST RESULTS 71
5.1 Read-out Electronics and Characterization Test Setup 71
5.2 Capacitive Enhancement Application 76
5.3 Characterization After Capacitive Enhancement 82
6 CONCLUSION AND FUTURE WORKS 87
REFERENCES 91

LIST OF TABLES

TABLES

Table 1.1. Comparison of post-process methods in the literature............................ 9

Table 3.1. Bonding trials with different parameters. 57

Table 5.1. Capacitive enhancement results of the sense mass 2/1 with 40 kHz, 0.1 V_{pp} AC signal. 81

Table 5.2. Comparison of achieved parameters. 85

LIST OF FIGURES

FIGURES

Figure 1.1. Oxidation matching. (a) After etching. (b) Oxidation of electrodes. (c) Removal of electrodes. (d) Obtaining sub-micron gaps [4]. 3
Figure 1.2. Some of the in-process methods. (a) Epitaxial gap tuning [11]. (b) High aspect ratio DRIE [2]. (c) Drive comb fingers with wavy gaps [10]. 5
Figure 1.3. SEM image of post-processed comb fingers [13]. 7
Figure 1.4. Comparison of minimum achievable capacitive gap 10x scale up of a gyroscope. 8
Figure 1.5. The designed gyroscope that is studied in this thesis........................... 10
Figure 2.1. A schematic view of a vibratory MEMS gyroscope. 14
Figure 2.2. Simple mass-spring-damper representation of drive mode.................. 14
Figure 2.3. Simple mass-spring-damper representation of sense mode. 17
Figure 2.4. Relations of position vectors with respect to the inertial and non-inertial reference frames. 18
Figure 2.5. Visualization of three fictitious forces on two out of phase masses. 20
Figure 2.6. Sense mode displacement due to Coriolis Force in (a) miss-match and (b) mode-match cases [25]. 22
Figure 2.7. Capacitance for parallel-plates. 24
Figure 2.8. Varying overlap type fingers. 26
Figure 2.9. Driving of varying overlap area type electrodes. 27
Figure 2.10. The differential drive of varying overlap area type electrodes. 28
Figure 2.11. Visualization of varying gap type electrodes. 29
Figure 3.1. The double-folded single-sided flexure element. 34
Figure 3.2. Deflected double-folded single-sided flexure element. 35
Figure 3.3. Cantilever beam with a concentrated load boundary condition. 36
Figure 3.4. Visualization of quadrature errors. 39
Figure 3.5. Drive mode shape of the gyroscope. 41
Figure 3.6. Sense mode shape of the gyroscope. 42

Figure 3.7. Near mode shapes to the operational frequencies, (a) out of plane mode shape and (b) in-phase mode shape of the gyroscope. 43
Figure 3.8. The overall fabrication process of the gyroscope. 45
Figure 3.9. The visualization of buried oxide after 400 microns device etching... 46
Figure 3.10. SEM image of the substrate wafer after anchor and bump are etched. 47
Figure 3.11. Microscope image (a) and SEM images (b) & (c) of the substrate wafer after metallization. 49
Figure 3.12. Substrate wafer after through-hole is formed. 50
Figure 3.13. The eutectic bonding process. 51
Figure 3.14. DRIE deep narrow etches optimization. 53
Figure 3.15. End of buried oxide in the wide gaps after the device etch is completed. 54
Figure 3.16. Protection of buried oxide difference in the sense fingers. 54
Figure 3.17. An SEM image from the drive fingers. 55
Figure 3.18. A cross-section view of a bonded stack. 56
Figure 3.19. Different fracture points after the razor blade test, (a) indicates a stronger bond and (b) indicates a weaker bond. 58
Figure 3.20. Quality measurement setup of the bonding process. 58
Figure 4.1. Capacitive Enhancement Methodology. 62
Figure 4.2. Physik Instrumente N-565 Linear Stage [36]. 62
Figure 4.3. Designed lever mechanism. 63
Figure 4.4. A simplified version of the designed gyroscope showing the contact points. 64
Figure 4.5. The overall assembly design of capacitive enhancement mechanism.. 64
Figure 4.6. Overall manufactured system. 65
Figure 4.7. Capacitive enhancement positioning adjustment for sense mode. 67
Figure 4.8. Capacitive enhancement positioning adjustment for drive mode......... 69
Figure 5.1. Fabricated device connected to the device PCB. 72
Figure 5.2. Characterization PCB and related electronic circuit units on it........... 72

Figure 5.3. Schematic view of a characterization setup. 73
Figure 5.4. Characterization setup. 74
Figure 5.5. Drive mode frequency response of Device-2 Gyroscope-2. 75
Figure 5.6. Designed capacitive enhancement PCB with the related electronic component attached. 76
Figure 5.7. Overall capacitive enhancement setup. 77
Figure 5.8. Capacitive enhancement of the sense fingers. (a) before capacitive enhancement, (b) after capacitive enhancement. 78
Figure 5.9. Capacitance increase visualization of the sense mass. (a) Before the enhancement process, (b) after the enhancement process. 79
Figure 5.10. Balance of capacitive enhancement. (a) After the enhancement process unbalanced capacitance, (b) after balancing operation...80
Figure 5.11. Capacitive enhancement of the drive fingers. (a) before capacitive enhancement, (b) after capacitive enhancement. 82
Figure 5.12. The difference of designed and fabricated drive mode comb fingers. 82
Figure 5.13. Drive mode frequency response test results after capacitive enhancement process under 40 V proof mass and 0.225 mTorr. 83
Figure 5.14. Sense mode frequency response test results after capacitive enhancement process under 25 V proof mass and 0.345 mTorr. 84

CHAPTER 1

INTRODUCTION

1.1 Overview of Capacitive Enhancement Processes

Within the past few years, increase in the demand of the miniaturized products boosts the popularity of MEMS devices. It is desired smaller, lighter, less power consuming, and more reliable devices especially in consumer products, navigation and guidance applications. Although MEMS devices are small in size, low cost and have low power consumption, they exhibit relatively low performance to their competitors in the market. Therefore, improving the accuracy of these devices is one of the main motivation sources of the literature.

Capacitive enhancement is one of the methods to improve the performance of the devices. It is achieving higher capacitances by extending the capabilities of the fabrication processes. Having high capacitances suppress the electro-mechanical noises which lead to increase in the SNR. The performance of the device is highly influenced by the capacitance so that increasing the capacitance enables to enhance the performance. The capacitance formula for a simple parallel plate is,

$$C = \varepsilon_0 \frac{Area}{Gap} \qquad 1.1$$

As it can be seen in Equation 1.1, there are several ways to increase the capacitance of a device. These terms are designed for maximizing the capacitance to increase the efficiency of the device. In most cases, the permittivity of the ambient is preferred vacuum which is as closest as the free space, so that better quality factors can be achieved. The second term, the area of the plates is designed to increase the capacitance in the boundaries of structural strength and design criteria. For the in-plane working designs, it is also possible to enhance the area by increasing the

thickness of the device layer. The thickness of the device will also increase the proof mass which leads to a decrease in the mechanical noise as indicated in [1]. Generally, that kind of bulk structures are formed by deep reactive ion etching (DRIE). While the dry chemical etch cycle which is combined with the ion bombardment etches the silicon, a protective polymer layer is deposited on the sidewalls to protect them in the passivation cycle. That etch and passivation cycles provide deep silicon etches [2]. However, there is a limit for aspect ratio, which is the minimum achievable gap with respect to depth of it. Although having thicker devices supply better mechanical noises and wider plate area, due to aspect ratio limitation, the gap of plates needs to be wider for them. That blocks the third them in Equation 1.1 which is the capacitive gap. However, the performance of a system can be increased enormously by decreasing the capacitive gaps while having a thicker device. Therefore, there are many kinds of research in the literature that will exceed the aspect ratio limitations and obtain better results.

Realizing submicron gaps is desired for a long time. It is difficult to achieve sub-micron gaps with the standard microfabrication techniques and control the gap resolution. There are different approaches to overcome that topic. These researches can be grouped in two categories which are “Post-Process Methods” and “In-Process Methods”. In-process methods contain the optimization of the fabrication process or adding another step to decrease the capacitive gaps. On the other hand, post-process methods include after-fabrication improvements.

In 1991-92, Hirano and Furuhata comes up with the idea that consist of both in-process and post-process methods. They proposed to adjust the finger gaps with a method which is called as oxidation matching. The structure of fingers is designed not engaged in the beginning and with zero or negative gaps. The gaps were then achieved with the ability of consuming silicon in thermal oxidation. Growing and removing thermal oxidation enables to control the width of the gap in a high resolution. The fingers can be positioned after the oxidation matching as engaged with an actuator. Figure 1.1 illustrates the overall oxidation matching process. In this way, the need for high driving voltage reduces while keeping the output force high

so that the integration of these chips to the circuits will be much easier. Hirano achieved up to 0.2-0.4 microns gaps by applying negative gaps to the non-engaged structure. Hirano and Furuhata also proved that sub-micron gaps can be achieved beyond lithography and etch capabilities [3], [4].

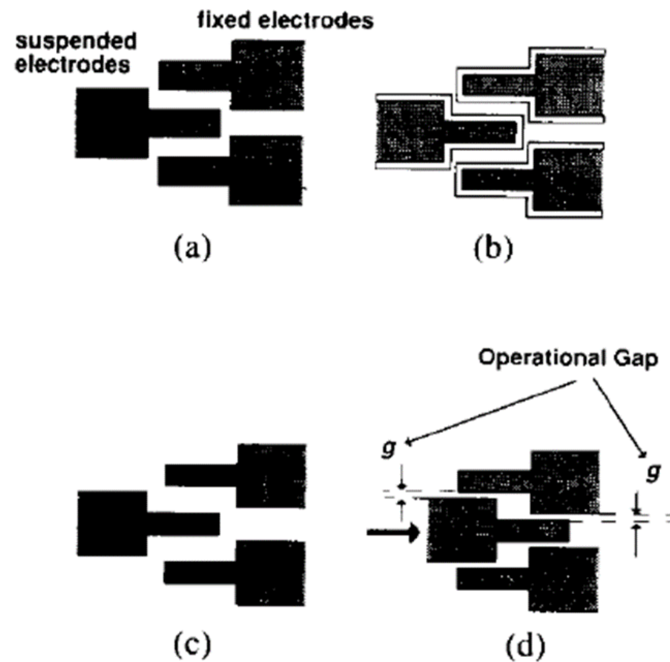

Figure 1.1. Oxidation matching. (a) After etching. (b) Oxidation of electrodes. (c) Removal of electrodes. (d) Obtaining sub-micron gaps [4].

1.1.1 In-Process Methods

In 2000, Ayazi proposes a new fabrication method that defeats the previous high aspect ratio technologies [5]. High aspect ratio combined poly and single crystal silicon (HARPSS) is a polysilicon trench fill operation that allows thick (hundreds of microns) devices to have sub-micron capacitive gaps. Sub-micron gaps can be achieved by low-pressure chemical vapor deposition (LPCVD) of sacrificial layer oxide and polysilicon. Ayazi achieved 1.2 microns capacitive gaps in 80 microns thick device. Later, Reuter et al realized a gap reduction by creating compressive stress on a bistable mechanism. The compressive stress is generated by the

deposition of thermal oxide, tungsten, and aluminum. Reuter obtained 1 micron gap which leads to 9 times greater capacitance than the DRIE limit of 3-micron gap for that structure with nearly same size of chip area [6]. In 2007, Pourkamali and Ayazi realize 1:460 aspect ratio with the HARPSS and prove that up to 10x larger aspect ratio than the state of art DRIE tools [7]. In the same year, Abdolvand improves the anisotropy of the DRIE in narrow trenches up to 1:40 ratios by inserting the argon de-passivation step [8]. The capacitance of a device can be improved by integrating the idea into the process steps. Although that can be possible by implementing a new step or optimization of process steps, structural modification of design can also be a method. In that manner, Pyatishev proposed a novel comb finger design which has a wavy side profile. The wider gaps in the profile, 5 microns, etches faster and helps to etch the near narrow gaps, 2 microns. The results show that there is a 60% increase in capacitance with respect to conventional variable drive fingers [9]. In 2012, Owen and Najafi optimize the DRIE process parameters. By ramping pressure, step duration, and bias power, they achieved up to 97.3 aspect ratios for 3-micron trenches [2]. That proves that optimization of process parameters can increase the achievable aspect ratios which leads to minimization of deep trench widths. Later, Ng reaches ultra-high aspect ratios which are beyond 1:500. After the DRIE operation, an epitaxial gap tuning process is realized. That combination of DRIE and epitaxial growing can obtain 100 nm width capacitive gaps without the loss of trench depth [10].

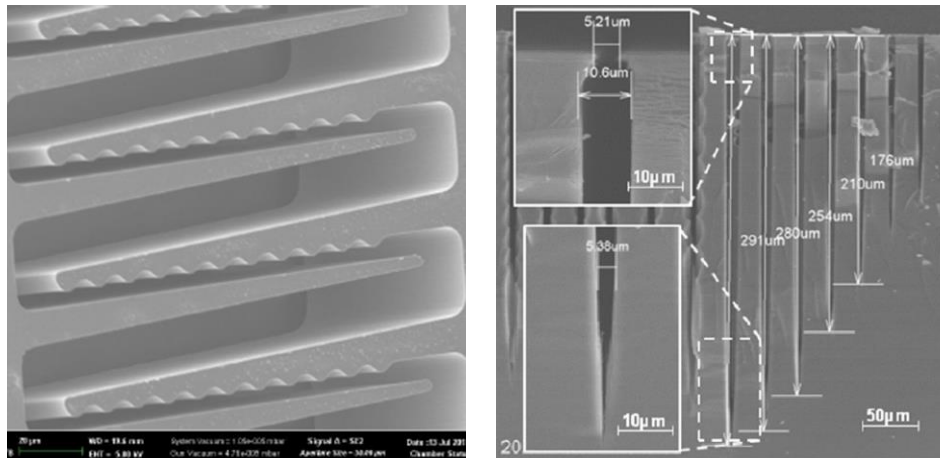

(a) (b)

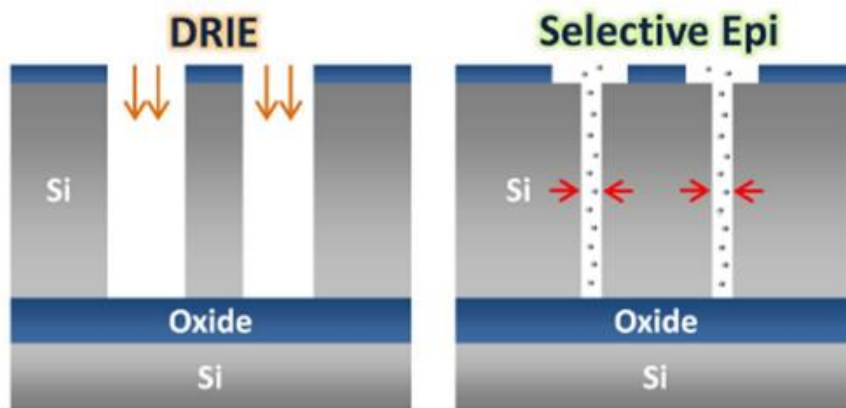

(c)

Figure 1.2. Some of the in-process methods. (a) Epitaxial gap tuning [11]. (b) High aspect ratio DRIE [2]. (c) Drive comb fingers with wavy gaps [10].

1.1.2 Post-Process Methods

Capacitive trenches can be improved also after the fabrication of the device. In that sense, trenches are designed and manufactured within the limits of the DRIE aspect ratio. However, with the post-process methods the capacitive gaps can be decreased. Obtaining such a feature necessaries a movable electrode which will be fixed later. After the fabrication processes are done, the capacitive trenches are adjusted to the working position which will be narrower gaps than the processed ones. To adjust the

gaps there should be an actuation mechanism to push the movable electrodes and a lock mechanism to fix these electrodes in the working position.

In 2003, Galayko proposes to decrease the initial fabricated gap by applying the pull-in voltage and using stoppers to adjust the working capacitive gaps. By using that method capacitive gaps are reduced from 3 microns to 0.2-0.4 microns for a 15 microns thick device with electrostatic pull-in voltage, ~24V [12]. The method provides better resolution than the lithography resolution and compensates structural layer over-etching errors. However, there will be also alignment and over-etching issues which result in 0.2-micron gap to 0.27 and 0.4-microns gap to 0.57 microns. After one year, Acar tries to enhance the capacitance by using a thermal actuator with the help of a ratchet mechanism [13]. The implemented system can reduce the 10 microns gap to the 1-2 microns gap. That leads to 7.22 times higher force in the drive mode compared to the conventional structure. Similarly, in 2009, Pyatishev realized a capacitive enhancement with a bistable mechanism. DRIE trenches are decreased from 5 microns to 2 microns [14]. Pyatishev did not use a fix mechanism. Although the bistable drive vibrates, the amplitude of it is much smaller than the primary oscillations. Later, Chen reports that after pull-in voltages the boundary conditions of the structure tend to change which provides an opposite frequency capability [15]. A different post-process approach was carried out by Nowack with the idea of permanent locking without the need for an extra force mechanism. Applying 50-70V pull in voltage the structure's position is adjusted to be permanent locking. The welding process to fix the electrodes is obtained by an electrical discharge with the help of a capacitor (10 megaohms, 100-300V). As a result, the initial electrode gap width between vertical comb electrodes was reduced to 385 nm from 4500 nm, with a final aspect ratio of 150. Beside from the gap reduction, Nowack utilizes a scallop removal technique which will lead to smoothing and paralleling the sidewalls [16]. As it can be seen in Nowack's method, electrostatic actuation is a convenient way for post-assembly structures. In 2013, Kuppireddi suggest decreasing the capacitive gap with the power of pull-in voltage and arranging the position with the help of the mechanic stoppers [17]. In the same manner, Ng,

Toan, Li reports narrow capacitive gaps can be achieved with an electrostatic pull-in beyond lithograph / etch capabilities [18]–[20]. Later, Pyatishev implements a bistable mechanism to the electrostatic actuator and acquire 2.5 times better actuator capacity compared to similar actuators. Lastly, in 2019, Elsayed achieved 870000 Q-factor by using a pull-in mechanism and the applied pull-in voltage also allows 10 times wider range for tuning the working frequency rather than the traditional electrodes [21].

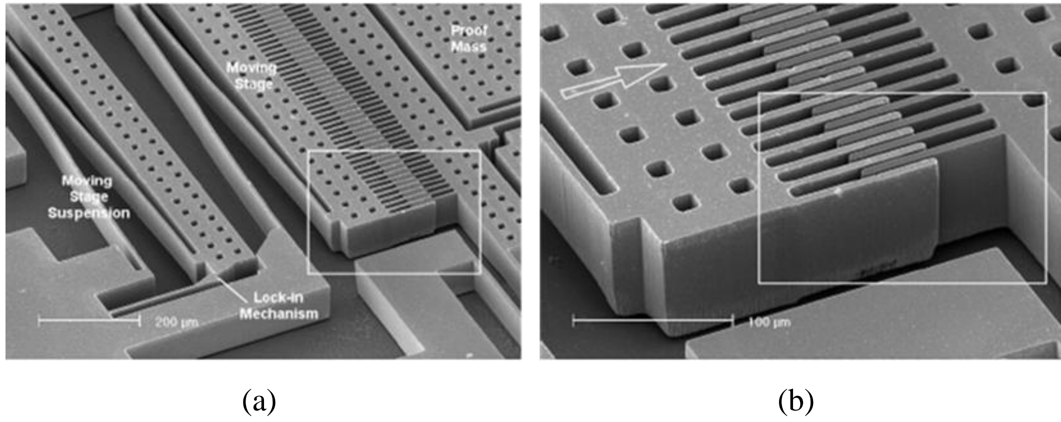

(a) (b)

Figure 1.3. SEM image of post-processed comb fingers [13].

1.2 Gyroscope Studied in This Thesis

Mechanical noise is one of the major noises in the gyroscope which limits the performance of it. Therefore, while designing the gyroscope it is desired to keep the mechanical noise as low as possible. The mechanical noise of a mode-matched gyroscope can be expressed as [22],

$$\Omega_{mech} = \frac{\sqrt{4k_B T \frac{m_s w_s}{Q_s}}}{2m_{pm} w_d X_d} \quad 1.2$$

Equation 1.2 states that increasing the proof mass, vibration frequency, and amplitude suppress the mechanical noise, substantially. Therefore, it is aimed to have a larger and thicker gyroscope which will provide a massive proof mass to decrease the mechanical noise. However, when it is tried to increase the size of the structure,

the minimum achievable capacitive gap also increases due to aspect ratio limitation. In METU MEMS Center, that ratio is nearly 1:40 which leads a minimum achievable gap for a 40 µm thick device nearly 1 µm. When the size of the structure increased ten times, the minimum achievable capacitive gap also increases ten times and becomes 10 µm. Figure 1.4 illustrates the minimum achievable capacitive gap with respect to 10x scaled up structure.

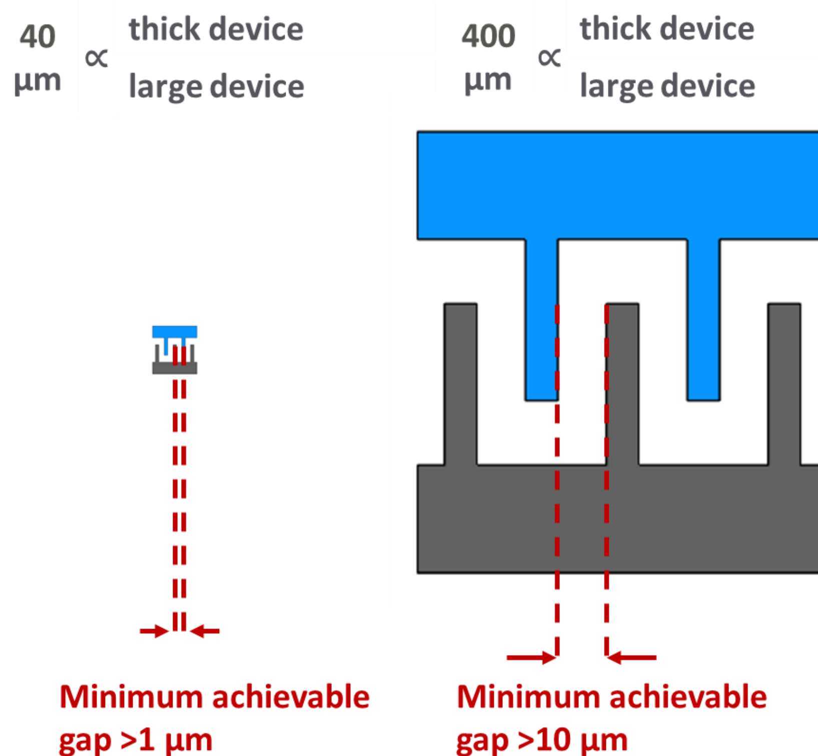

Figure 1.4. Comparison of minimum achievable capacitive gap 10x scale up of a gyroscope.

Although designing a ten times bigger structure provides a massive proof mass, the aspect ratio limits the potential improvement of the capacitance values despite having larger capacitive areas. For that reason, a post-process capacitive enhancement process is planned for the designed gyroscope to overcome the aspect ratio limitation. Table 1.1 summarizes the post-processed researches in the literature with proposed methods, electrode types and features. As it can be seen (Table 1.1), the proposed approach investigates capacitive enhancement for such a thick and

large structures for the first time. Beside from that, the post-process method is also a novel method to satisfy the force requirements of such a thick device.

Table 1.1. Comparison of post-process methods in the literature.

	Device Thickness	Post-Process Method	Electrode Type	Capacitive Gap	Features
[13]	100 µm	Thermal Act. ratchet	Comb Fingers Parallel Plates	10 µm → 1 µm 10 µm → 1-2 µm	7.22 times larger driving force
[16]	57 µm	Elec. Act. M-arc welding	Parallel Plates	4.5 µm → 385 nm	13x larger driving force
[17]	4 µm	Elec. Pull Stoppers	Parallel Plates	2.5 µm → 250 nm	45 dB increase
[18]	5 µm	Elec. Pull Stoppers	Parallel Plates	400 nm → 100 nm	21 dB increase Motional-R decrease 200x Q-factor (0.01 Pa): 64 000 → 49 000
[20]	25 µm	Elec. Pull Stoppers	Parallel Plates	2 µm → 0.5 µm	23 dB increase @20V Q-factor decreased from 970 000 to 27 000
[19]	40 µm	Elec. Pull Stoppers	Parallel Plates	900 nm → 200 nm	-
[14]	90 µm	Elec. Act. Bi-stable	Comb Fingers	12 µm → 2 µm	Increased capacity factor 2.5 Q-factor: 60 000 (0.12mTorr)
[21]	10 µm	Elec. Pull Stoppers	Parallel Plates	2 µm → 200 nm	Q-factor (1mTorr):870 000 60x decrease motion R -33 dB insertion loss
This Work	400 µm	Ext. Act. Epoxy	Comb Fingers Parallel Plates	12 µm → 2 µm 25 µm → 2 µm	8x increase in the drive force 12.5x increase in the sense capacitance

Figure 1.5 shows the designed gyroscope that is studied in this thesis. Two identical masses are connected with a diamond shape coupling mechanism. The device is

designed to be 400 microns thick with a 48 mm x 21 mm footprint which is quite bigger than the conventional gyroscopes. The reason behind the massive gyroscope is suppressing the mechanical noise by enhancing the proof mass. Beside from this, the gyroscope will have also higher capacitance due to large proof mass with deep thickness. However, the DRIE aspect ratio problem limits the achievable minimum gap that will create huge capacitances. Therefore, capacitive fingers of the device are designed to be not engaged in the mask. These fingers will be engaged after the fabrication with a post-process capacitive enhancement. To carry out this process normally fixed masses are designed to be suspended for the enhancement process. That masses are fixed with epoxy after the enhancement process. There are four sense and two drive masses that will be engaged with post-process.

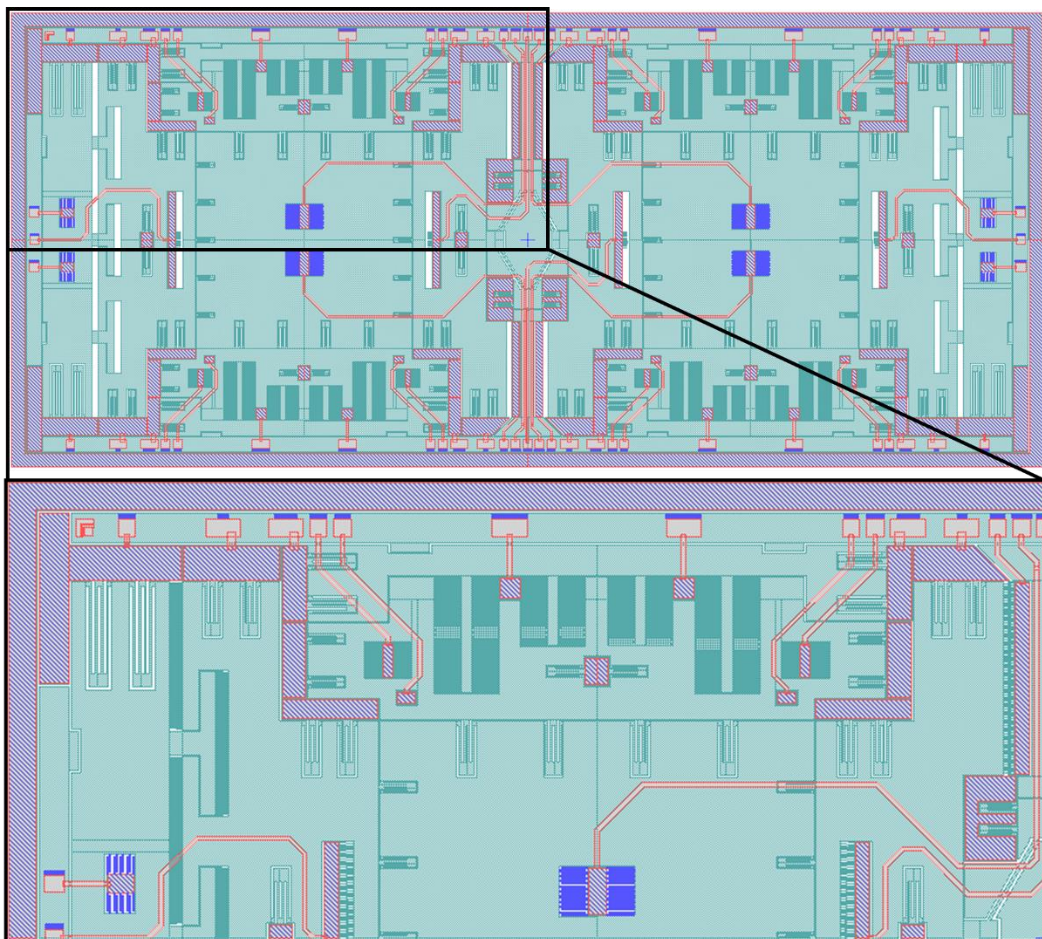

Figure 1.5. The designed gyroscope that is studied in this thesis.

The device wafer is formed with an SOI wafer and then bonded to the substrate wafer which is for metal lines and anchor points. In Figure 1.5, the blue paint indicates the anchor points while the red one stands for metallization.

1.3 Research Objectives and Thesis Organization

The main objective of this work is realizing capacitive enhancement in the drive and sense electrodes that will reach huge capacitances beyond the fabrication limitations. Parallel to that, side objectives can be listed as follows:

1. Designing a gyroscope with a thicker and larger mass. Since the mechanical noise of the gyroscope can be suppressed with a larger proof mass, that will decrease overall noise. That device should also be compatible with the capacitive enhancement process.
2. Modelling the gyroscope mathematically so that the effect of each parameter can be visualized. Realizing FEM analysis for the verification of the designed gyroscope whether it matches with the mathematical model. That will also provide useful information for the designing part.
3. Planning and performing a suitable fabrication procedure for the larger and thicker gyroscopes. The process steps require optimizations to achieve such devices.
4. Realizing a post-process method that will enhance the capacitance of the device. Achieving narrow capacitive gaps, balancing the fingers with respect to each other, and then fixing them with a suitable method.
5. Performing frequency response tests for the characterization of the devices. The performance of the devices is analysed and compared with the designed parameters.

The summary of the content and organization of this thesis are presented below:

Chapter 2 includes the mathematical model of the gyroscopes. Drive and sense mode equations are derived. Moreover, electrostatic actuation and sensing mechanisms are expressed in detail.

Chapter 3 describes the design parameters of the gyroscope. Flexion elements, electrostatic force compensation, and tuning electrodes are summarized. FEM simulations of the designed drive and sense mode frequencies are presented. Finally, detailed fabrication steps, optimizations, encountered problems, and possible solutions to them.

Chapter 4 presents the overall capacitive enhancement processing. Proposed capacitive enhancement methodology, designed capacitive enhancement mechanism is explained. The enhancement process of the sense and drive mass is expressed.

Chapter 5 describes the characterization and post-process tests setups which are used for the fabricated gyroscopes. Designed PCB assemblies, frequency response test setup, and results of the fabricated devices are shown. Besides, capacitive enhancement process setup and improvement results are presented.

CHAPTER 2

VIBRATORY MEMS GYROSCOPE THEORY

In this chapter, the mechanical and electrostatical models of the gyroscope are presented. Section 2.1 introduces the schematic view of a gyroscope. In Section 2.2 and 2.3, it is presented the mechanics of drive mode and sense mode, respectively. Section 2.4 demonstrates the electrostatic actuation and sensing methods. Lastly, Section 2.5 briefly summarizes this chapter.

2.1 Mechanical Model of Gyroscope

In all resonating gyroscopes, it is essential that a driving mechanism for continuous vibration of the proof mass and a sensing mechanism to pick the Coriolis coupling [23]. Since there is a need for a vibration mechanism on both the drive and sense axis, an appropriate suspension system is also required. That suspension system is designed to isolate the drive mode vibration of proof mass from the sense mass so that, the decoupled sense mechanism does not be affected and the cross-talk between the modes is minimized. Otherwise, there would be an offset generated by the gyroscope itself even without any angular output. In Figure 2.1, a simplified perspective view of a gyroscope structure is shown. Clearly, the proof mass has 2 DOF so that the Coriolis coupling can be generated between two modes. The other two masses, the drive and sense mass, are decoupled. Although that decoupling seems to be realized with rollers, it is designed with flexible beams to avoid friction. That flexible beams will be discussed in CHAPTER 3.

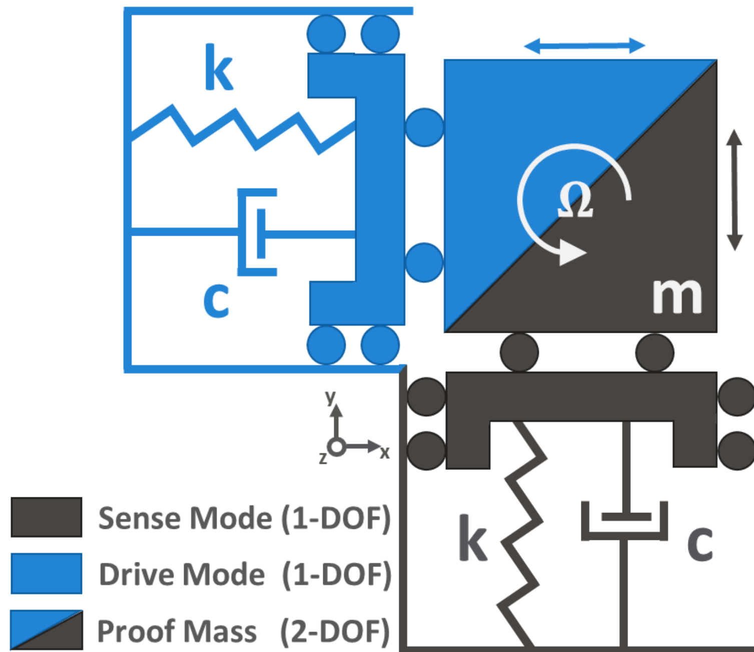

Figure 2.1. A schematic view of a vibratory MEMS gyroscope.

2.2 Mechanics of Drive Mode

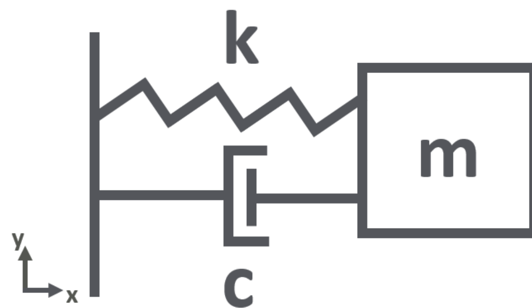

Figure 2.2. Simple mass-spring-damper representation of drive mode.

In order to exert Coriolis force, the proof mass must be in a motion otherwise the Coriolis force will be zero. This motion can be provided by the continuous vibration of the proof mass with the movable drive blocks together [24]. Therefore, the overall drive mode can be modelled as a vibrating mass, spring, damper system.

$$m_d\ddot{x} + c_d\dot{x} + k_d x = F_d\, sin(wt) = Im[F_d e^{iwt}] \qquad 2.1$$

$$m_d\ddot{x} + c_d\dot{x} + k_d x = F_d e^{iwt} \qquad 2.2$$

Here in Equation 2.1, m_d is the drive mode mass which consists of drive mass and proof mass because they both vibrate together. The overall spring constant is k_d, structural and air damping in the drive mode is c_d and t stands for time. Lastly, F_d is the driving force acting on the system along the x-axis and w is the frequency of the applied force. The applied force is assumed to be a harmonic sine function for simplification of the response but, it is written in the equations in a general form. Assuming the solution is in the form of,

$$x(t) = Xe^{iwt} \qquad 2.3$$

by putting the Equation 2.3 into Equation 2.2,

$$-w^2 m_d X e^{iwt} + iwc_d X e^{iwt} + k_d X e^{iwt} = F_d e^{iwt} \qquad 2.4$$

and arranging the Equation 2.4 into regular form,

$$(-w^2 m_d + iwc_d + k_d) X e^{iwt} = F_d e^{iwt} \qquad 2.5$$

then the response can be found as,

$$X = \frac{F_d}{k_d - w^2 m_d + iwc_d} \qquad 2.6$$

Also, the response can be separated as static deflection and complex response,

$$X = \frac{F_d/k_d}{(1 - \frac{w^2}{{w_d}^2}) + i(2\zeta_d \frac{w}{w_d})} = H(w)\frac{F_d}{k_d} \qquad 2.7$$

where,

$$H(w) = \frac{1}{1 - \frac{w^2}{{w_d}^2} + i2\zeta_d \frac{w}{w_d}} \qquad 2.8$$

$$\zeta_d = \frac{c_d}{2\sqrt{m_d w_d}} \;\&\; w_d = \sqrt{\frac{k_d}{m_d}} \qquad 2.9$$

The above equation, w_d represents natural frequency and ζ_d is the ratio of effective damping to the critical damping of the drive mode. The frequency response magnitude and phase can also be found,

$$|H(w)| = \frac{1}{\sqrt{(1-\frac{w^2}{{w_d}^2})^2 + (2\zeta_d \frac{w}{w_d})^2}} \tag{2.10}$$

$$\phi = tan^{-1}(\frac{2\zeta_d \frac{w}{w_d}}{1-\frac{w^2}{{w_d}^2}}) \tag{2.11}$$

Then, the response can be expressed as,

$$x(t) = \frac{F_d}{k_d}|H(w)|e^{i(w_d t-\phi)} \tag{2.12}$$

Note that, the solution that has been found in Equation 2.12 is the steady-state solution of the drive mode. The transient part of the solution is not important because in the drive mode a steady vibration is required. In the response, F_d/k_d term is the static deflection part and that is the solution of the constant DC force excitation. $|H(w)|$ is the magnification factor of the system and ϕ is the phase of the response. If the excitation force is a sine function as indicated in the beginning,

$$x(t) = \underbrace{\frac{F_d}{k_d}|H(w)|}_{X} sin(w_d t-\phi) \tag{2.13}$$

When drive mode excited at its resonance frequency ($w = w_d$), magnification turns into,

$$|H(w)| = \frac{1}{2\zeta_d} = Q_d \tag{2.14}$$

where Q_d is the quality factor and it can be expressed as,

$$Q_d = \frac{\sqrt{m_d k_d}}{c_d} \tag{2.15}$$

at resonance frequency, phase can be expressed as,

$$\phi = tan^{-1}(\frac{2\zeta_d}{0°}) = 90° \tag{2.16}$$

Then, the response at resonance frequency,

$$x(t) = \underbrace{\frac{F_d Q_d}{k_d}}_{X} sin(w_d t - 90°) = -X\, cos(w_d t) \tag{2.17}$$

$$\dot{x}(t) = X_d w_d\, sin(w_d t) \tag{2.18}$$

The drive mass is assumed to be driven at its natural resonance frequencies because at resonance frequency the magnification factor is maximized. That provides the system largest vibration amplitude with lower power consumption. However, in that case, ζ_d has a significant effect. Mostly, $\zeta_d < 1$ case is desirably due to the need for continuous vibrations in the drive mode. Beside from that, Equation 2.18 implies that there is a 90° phase shift between actuation force and response.

2.3 Mechanics of Sense Mode with Coriolis Coupling

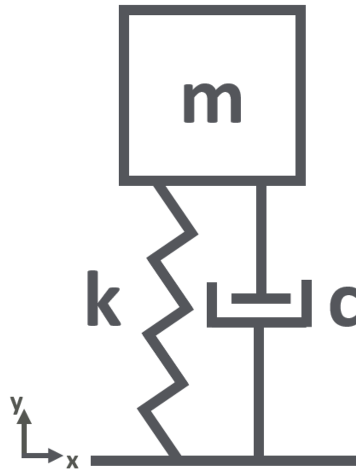

Figure 2.3. Simple mass-spring-damper representation of sense mode.

In in-plane gyroscopes, the manoeuvres of the body are assumed to occur with a planar motion. In that way, the sense mode can also be simplified as a different mass, spring, and damper system. However, this time instead of driving force it is under the effect of Coriolis, Centrifugal, and Tangential forces which are self-induced fictitious forces to simplify the system.

The principle of the gyroscope is detecting the angular velocity so that the overall body can be supposed to be on a non-inertial reference frame $F_a(A)$ with an angular

velocity $\overrightarrow{W}_{A/O}$ with respect to the inertial reference frame $F_o(O)$. If the center of mass of the sense mode is assumed to be on the point P, the position of the body can be written as,

$$\vec{r} = \vec{r}^{\iota} + \vec{r}^{o} \qquad 2.19$$

The relations of these vectors can be seen in Figure 2.4.

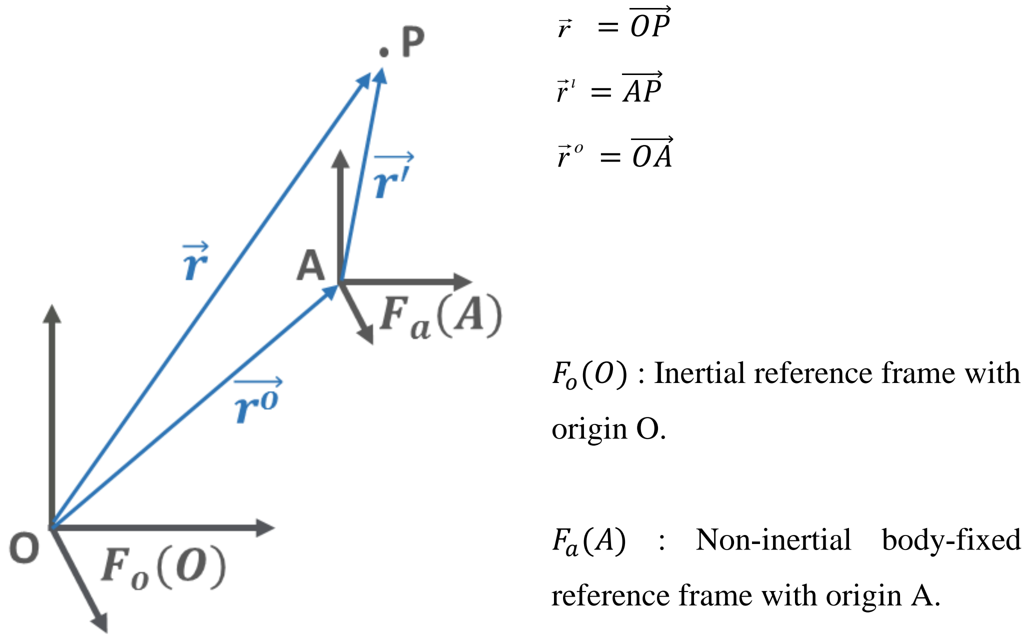

Figure 2.4. Relations of position vectors with respect to the inertial and non-inertial reference frames.

To achieve the velocity and acceleration information about the body, the time derivative of the Equation 2.19 can be taken,

$$D_O\vec{r} = D_A\vec{r}^{\iota} + \overrightarrow{W}_{A/O}\; x\; \vec{r}^{\iota} + D_O\vec{r}^{o} \qquad 2.20$$

Note that, there are additional terms in the Equation 2.20. That is because of the $F_a(A)$ frame is actually rotating with $\overrightarrow{W}_{A/O}$ and the point P is defined in that frame. By taking another time derivative for achieving the acceleration of the body,

$$\begin{aligned} D_O{}^2\vec{r} = D_A\left[D_A\vec{r}^{\iota} + \overrightarrow{W}_{A/O}\; x\; \vec{r}^{\iota}\right] + \overrightarrow{W}_{A/O}\; x\; \left[D_A\vec{r}^{\iota} + \overrightarrow{W}_{A/O}\; x\; \vec{r}^{\iota}\right] \\ + D_O{}^2\vec{r}^{o} \end{aligned} \qquad 2.21$$

$$D_O{}^2\vec{r} = D_A{}^2\vec{r}^{\iota} + (D_A\vec{W}_{A/O})x\vec{r}^{\iota} + \vec{W}_{A/O}(D_A\vec{r}^{\iota}) + \vec{W}_{A/O}x(D_A\vec{r}^{\iota}) + \vec{W}_{A/O}x(\vec{W}_{A/O}x\vec{r}^{\iota}) + D_O{}^2\vec{r}^{o} \quad 2.22$$

Making the necessary arrangements,

$$D_O{}^2\vec{r} = D_A{}^2\vec{r}^{\iota} + \left(D_A\vec{W}_{A/O}\right) x\, \vec{r}^{\iota} + \vec{W}_{A/O}(D_A\vec{r}^{\iota}) + \vec{W}_{A/O}\, x\, (D_A\vec{r}^{\iota}) + \vec{W}_{A/O}\, x\, (\vec{W}_{A/O}\, x\, \vec{r}^{\iota}) + D_O{}^2\vec{r}^{o} \quad 2.23$$

Rearranging the Equation 2.23 and using $\vec{W}_{A/O} = \vec{\Omega}$ for simplification,

$$\vec{a}_{P_{(F_o(O))}} = \underbrace{\vec{a}_{P_{(F_a(A))}}}_{\substack{Acc.\ of\ P \\ w.r.t.\ inertial \\ frame(A)}} + \underbrace{2\vec{\Omega}\, x\, \dot{\vec{v}}_{P_{(F_a(A))}}}_{Coriolis\ Acc.\ of\ P} + \underbrace{\dot{\vec{\Omega}}\, x\, \vec{r}_{P/A}}_{\substack{Tangential \\ Acc.\ of\ P}} + \underbrace{\vec{\Omega}\, x(\vec{\Omega}\, x\, \vec{r}_{P/A})}_{\substack{Centripetal \\ Acc.\ of\ P}} + \underbrace{\vec{a}_{A_{(F_o(O))}}}_{\substack{Acc.\ of \\ Non-inertial \\ ref.frame(A) \\ w.r.t. \\ inertial frame(O)}} \quad 2.24$$

In Equation 2.24, all the acceleration terms of the particle P moving on a non-inertial frame with respect to an inertial frame are summarized. Those acceleration terms can be used as fictitious forces as if they are acting on the body. However, different from the overall sense mass, proof mass (m_{PM}) should be considered because all the fictitious forces are directly coupled with the proof mass.

$$m_{PM}\vec{a}_{P_{(F_o(O))}} - m_{PM}\vec{a}_{P_{(F_a(A))}} - m_{PM}[2\vec{\Omega}x\dot{\vec{r}}_{P_{(F_a(A))}}] + m_{PM}[\dot{\vec{\Omega}}x\vec{r}_{P/A}] + m_{PM}[\vec{\Omega}x(\vec{\Omega}x\vec{r}_{P/A})] = 0 \quad 2.25$$

where,

$$F_{Coriolis} = -2m_{PM}(\vec{\Omega}x\dot{\vec{r}}_{P_{(F_a(A))}}) \quad 2.26$$

$$F_{Tangential} = -m_{PM}(\dot{\vec{\Omega}}x\vec{r}_{P/A}) \quad 2.27$$

$$F_{Radial} = -m_{PM}\vec{\Omega}x(\vec{\Omega}x\vec{r}_{P/A}) \quad 2.28$$

Notice that, among all the terms of Equation 2.26-2.27-2.28 only the Coriolis force is linearly proportional with the applied rotation. Centripetal acceleration terms are dependent on the position vector $\vec{r}$. That results in position-dependent response in

the sense mode. On the other hand, the tangential acceleration term is proportional. In that case, sensing the time-invariant rotations would not be possible. Therefore, to construct a more reliable sense mechanism preferring the Coriolis acceleration terms will be wise. Moreover, the cross product of the Coriolis acceleration term results in a vector that is perpendicular with rotation and velocity vectors. That idea is the fundamental principle of vibratory gyroscopes [23]. However, it is needed to reject the centripetal, tangential forces and utilize the Coriolis force for the complete gyroscope. Visualization of these three forces with respect to a stationary observer can be seen in the Figure 2.5. Elimination of the unwanted accelerations (linear accelerations inc.) could be realized by driving two separate masses out of phase and reading them differentially. Therefore, from this point, other acceleration terms will not be included in the equations.

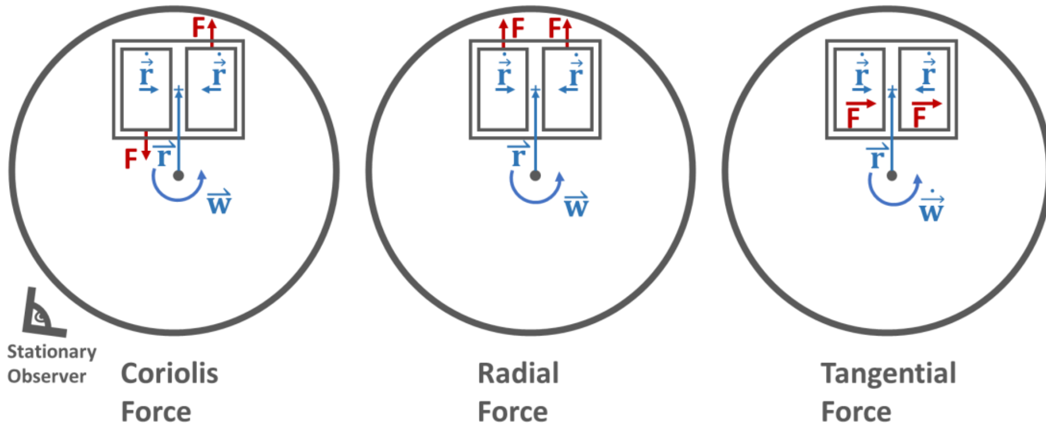

Figure 2.5. Visualization of three fictitious forces on two out of phase masses.

$$m_s\ddot{y} + c_s\dot{y} + k_s y = F_{coriolis} \qquad 2.29$$

As in the drive mode equations, m_s is the sense mode mass, $c_s$is structural and air damping in the sense mode and k_s is the overall spring constant along with the sense mode. Coriolis force is expressed as,

$$F_{coriolis} = -2m_{pm}\Omega_z\dot{x} \qquad 2.30$$

where,

m_{pm}: Proof mass

m_s : Proof mass + Sense mass

Excitation of the sensor can be assumed in the form of,

$$F_d(t) = -F_d \, sin(\, w_d t) \quad 2.31$$

$$X(t) = X_d \, cos(\, w_d t) \quad 2.32$$

$$\Omega_z(t) = \Omega_z \, cos(\, w_z t) \quad 2.33$$

by putting above equations into Equation 2.30,

$$F_{coriolis}(t) = 2 m_{pm} \Omega_z X_d w_d (sin(\, w_d t) \, cos(\, w_z t)) \quad 2.34$$

and using sine multiplication formula,

$$F_{coriolis}(t) = m_{pm} \Omega_z X w_d (sin(\,(w_d + w_z)t) + sin(\,(w_d - w_z)t)) \quad 2.35$$

by re-arranging Coriolis force in the exponential form,

$$F_{coriolis}(t) = Im\left[F_s(e^{i(w_d+w_z)t} + e^{i(w_d-w_z)t})\right] \quad 2.36$$

The response of the sense mode will be as in the drive mode,

$$Y = \frac{F_{coriolis}/k_s}{(1 - \frac{w^2}{{w_s}^2}) + (i2\zeta_s \frac{w}{w_s})} \quad 2.37$$

but, Coriolis force cause response with two different frequencies,

$$Y(w_d + w_z) = \frac{F_s/k_s}{(1 - \frac{(w_d + w_z)^2}{{w_s}^2}) + (i2\zeta_s \frac{(w_d + w_z)}{w_s})} \quad 2.38$$

$$Y(w_d - w_z) = \frac{F_s/k_s}{(1 - \frac{(w_d - w_z)^2}{{w_s}^2}) + (i2\zeta_s \frac{(w_d - w_z)}{w_s})} \quad 2.39$$

Those two frequencies are equally separated from w_d by w_z. In this case, there are two different options to operate the vibratory gyroscopes which are mode-match and miss-match. While in the mode-matching frequencies of sense and drive modes are matched, in miss-matching there is an arranged frequency split between them. Both of the methods have their advantages. The mode-matching method tries to maximize the mechanical output of the system. That leads to suppress the electrical noise

significantly which plays an important role when determining the system performance [22]. In miss matching, sense displacement is not as high as in mode matching. However, generally, it is more stable and preferred for wide bandwidth requirements. In this thesis, a mode-matched case is preferred due to high sensitivity.

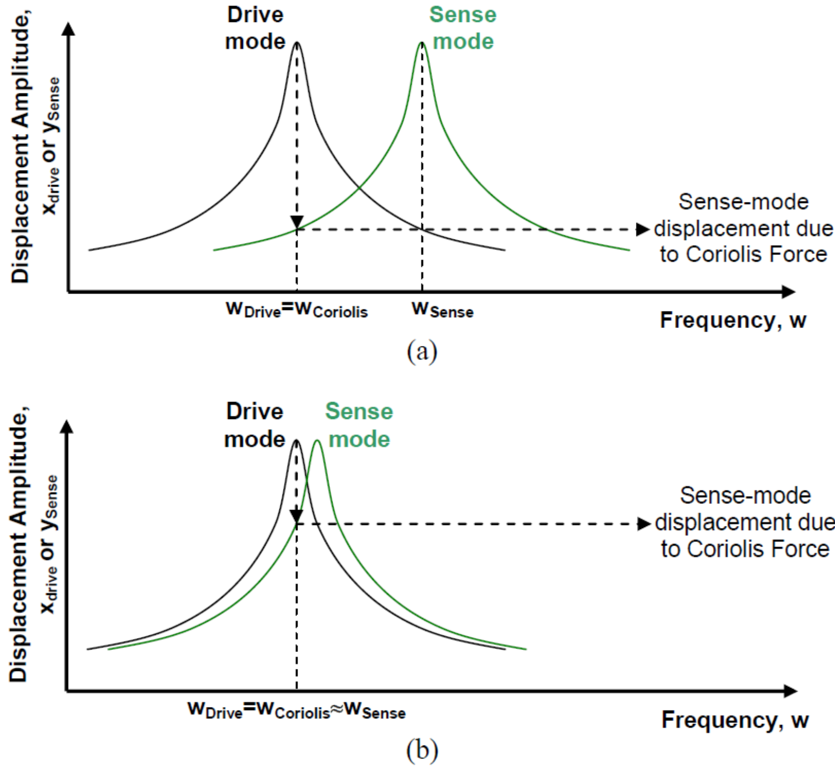

Figure 2.6. Sense mode displacement due to Coriolis Force in (a) miss-match and (b) mode-match cases [25].

If we make assumptions $w_d \simeq w_s$ and $w_d >> w_z \rightarrow w_z = 0$. Solution turns into,

$$Y = Y(w_d + w_z) + Y(w_d - w_z) \qquad 2.40$$

$$Y = 2\frac{m_{pm}X_d\Omega_z w_d}{k_s} Q_S\, sin(w_d t - \psi) \qquad 2.41$$

where,

$$\psi = tan^{-1}\frac{2\xi_s}{0} = 90° \qquad 2.42$$

by using Equations 2.41 & 2.42,

$$Y = 2\frac{m_{pm}X_d\Omega_z w_d}{k_s}Q_S\, sin(\, w_d t - 90°) \qquad 2.43$$

$$Y = -2\frac{m_{pm}X_d\Omega_z w_d}{k_s}Q_S\, cos(\, w_d t) \qquad 2.44$$

$$\dot{Y} = 2\frac{m_{pm}X_d\Omega_z {w_d}^2}{k_s}Q_S\, sin(\, w_d t) \qquad 2.45$$

One can notice that the quality factor term (Q_S) exists as in the drive mode equations. Quality factor amplifies the sense mode deflections so that sensitivity is magnified. Beside from that, the Coriolis force is directly proportional to the drive response (X), so having high-quality factor in the drive will boost the Coriolis force. Increasing Coriolis magnitude will also increase the sensitivity, significantly. As in Equation 2.15, the quality factor is inversely proportional to the damping factor. A small value of damping coefficient will cause a higher quality factor. The fewer air particles will provide a lower damping coefficient. Therefore, operating the gyroscope in the vacuum ambient will be assure the best quality factor.

2.4 Electrostatic Actuation and Sensing

The basic principle of electrostatic actuation lies on the neutralization tendency of the two parallel plates. The parallel plates are repelling each other when they are biased at different potentials. The attraction force is used to generate a motion on the plates if at least one of them have one or more degree of freedom in the direction of the generated force. On the other hand, the change in the capacitance can also be monitored with the electrostatic sensing.

Although electrostatic forces are not often used for macroscopic operations, they are really popular in micro-scale operations. Having large surface-to-volume ratios and sub-micron gaps forms huge capacitances with respect to their small masses. That is why they are used widely for actuation and sensing in MEMS technology. Beside from that, the simplicity of the implementation, low power consumption rates, low

drift, low-temperature sensitivity, and fast response also plays an important role on the popularity of electrostatic methods [26].

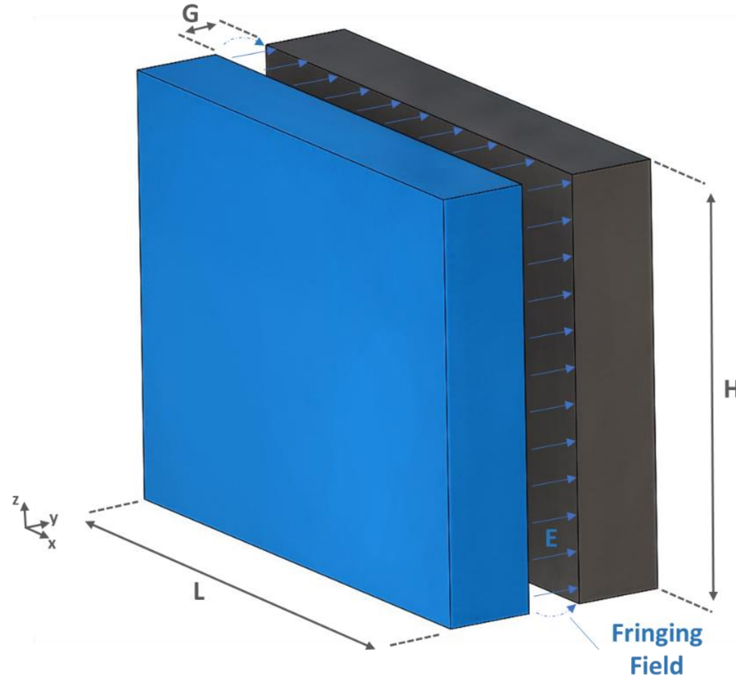

Figure 2.7. Capacitance for parallel-plates.

Capacitance for parallel plates as in Figure 2.7 can be expressed as,

$$C = \varepsilon_0 \alpha \frac{Area}{Gap} = \varepsilon \alpha \frac{L(x)H(z)}{G(y)} \quad 2.46$$

and the motion of each direction can be assumed as,

$$L(x) = L_0 + x \quad 2.47$$

$$H(z) = H_0 - z \quad 2.48$$

$$G(y) = G_0 - y \quad 2.49$$

In the above equations (Equations 2.47-2.48-2.49), while $L(x)$ & $H(z)$ represents overlap length & height of the parallel plates, $G(y)$ stands for the capacitive gap between two plates. In addition to that, L_0, H_0 and G_0 terms state their initial values, respectively. Lastly, ε_0 is the permittivity of the free space and α is the fringing field

factor. Although the fringing field effect is changing slightly with the displacement, it is assumed constant to simplify the further equations. The attraction force that is created by two parallel plates can be derived from the energy equation for a capacitor. The energy equation for a capacitor,

$$E = \frac{1}{2} C V^2 \tag{2.50}$$

By taking the derivative of Equation 2.50, electrostatic force can be found as,

$$F_{electrosatic} = \frac{\partial E}{\partial r} = \frac{1}{2}\frac{\partial C}{\partial r} V^2 \tag{2.51}$$

$$F_{e,x} = \frac{\partial E}{\partial x} = \frac{1}{2}\frac{\partial C}{\partial x} V^2 = \frac{1}{2}\alpha\varepsilon_0 \frac{H_o}{D_o} V^2 \tag{2.52}$$

$$F_{e,y} = \frac{\partial E}{\partial y} = \frac{1}{2}\frac{\partial C}{\partial y} V^2 = \frac{1}{2}\alpha\varepsilon_0 \frac{H_0 L_0}{(D_0 - y)^2} V^2 \tag{2.53}$$

$$F_{e,z} = \frac{\partial E}{\partial z} = \frac{1}{2}\frac{\partial C}{\partial z} V^2 = -\frac{1}{2}\alpha\varepsilon_0 \frac{L_0}{D_0} V^2 \tag{2.54}$$

In the derived equations, it can be seen that while x & z-directions are independent of position, the y-direction is inversely proportional with the attraction force. That is because the rate of change of capacitance in the x and z-directions are constant but not in y-direction. This means sensitivity along y-direction is higher compared to other directions, but worse linearity is the trade-off [24]. Using the capacitive parallel plates in y-direction called as varying gap type electrodes. Beside from this, in the x and z-directions, the situations are vice versa. While the linearity is high, sensitivity is low. This type of usage is called as varying overlap area electrodes. That difference may help to construct a high-performance gyroscope. Although the varying gap type has a nonlinearity, which is a challenging problem, since the displacement in the sense mass is in the order of a few angstroms, the nonlinear graph can be assumed as linear in such a small portion. On the other hand, in the drive mode, major concern is linearity so that using varying overlap type for that will be more reasonable [22].

For both types, the capacitors are designed with comb fingers which have a large length to width ratio to be compact. Most of the time, the fingers are rectangular shape but they can be changed with respect to the application purpose.

In the varying-overlap area type electrodes, the capacitance is,

$$C = \frac{2n\varepsilon(L_0 + x)h}{g} \qquad 2.55$$

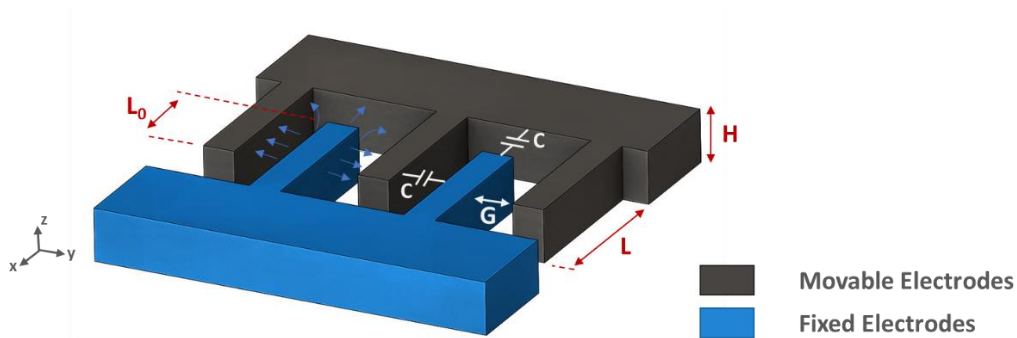

Figure 2.8. Varying overlap type fingers.

and by using Equation 2.52, electrostatic force can be shown as,

$$F_x = \frac{\partial E}{\partial x} = \frac{n\varepsilon h}{g} V^2 \qquad 2.56$$

In Equation 2.56, V represents the applied potential and n is the number of engaged fingers on the one side of the electrodes. As stated before, the proof mass should be in a continuous motion to acquire the Coriolis force. In the vibratory gyroscopes that motion is the vibration of the drive mode in the resonance frequency. Normally, applying a potential difference to the electrodes provides a unidirectional force that is insufficient for the vibration of the body, continuously. However, if the drive axis of the gyroscope is driven sinusoidally, the speed and amplitude must be reputable and insensitive to environmental factors [26]. Therefore, applying DC voltage to movable electrodes and fixed electrodes AC voltage will provide these sinusoidal movements as in Figure 2.9.

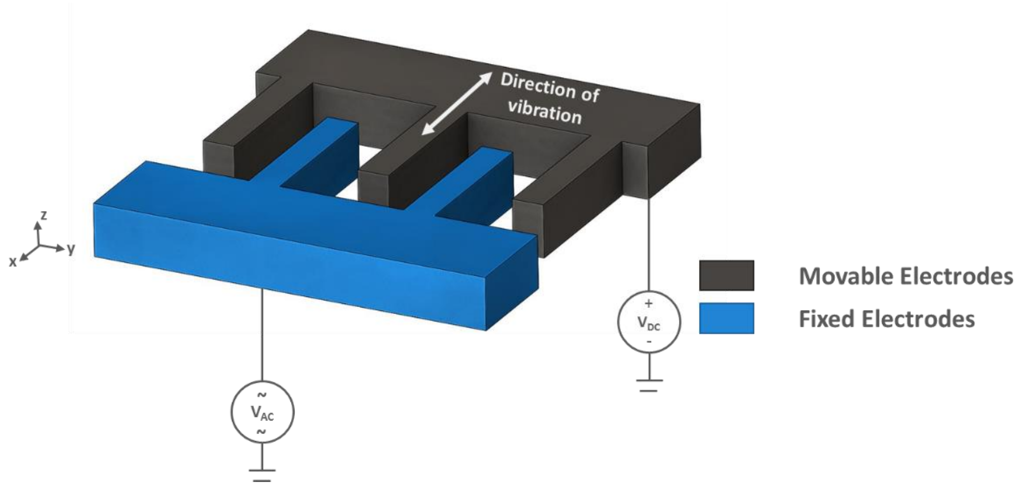

Figure 2.9. Driving of varying overlap area type electrodes.

If it is applied DC voltage to movable electrodes and AC voltage to fixed electrodes, the force equation in Equation 2.56 turns into,

$$F_x = \frac{\partial E}{\partial x} = \frac{n\varepsilon h}{g}(V_{AC} - V_{DC})^2 \qquad 2.57$$

where,

$$V_{AC} = v_{ac}\, sin(wt) \qquad 2.58$$

Then, the obtained force is,

$$F_x = \underbrace{\frac{n\varepsilon h}{g}\left(\frac{{v_{ac}}^2}{2} + {V_{DC}}^2\right)}_{DC\ Term} - \underbrace{\frac{n\varepsilon h}{g} 2V_{DC} v_{ac}\, sin(wt)}_{Sinusoidal\ (at\ w)\ Term} - \underbrace{\frac{1}{2}\frac{n\varepsilon h}{g} cos(2wt)}_{\substack{Double\ Freq.\\ (at\ 2w)\ Term}} \qquad 2.59$$

Notice that, in Equation 2.59, there are two more terms other than desired frequency of the force which is the sinusoidal (at w) term. To obtain a fine and neat vibration in the drive mode these terms can be eliminated with a differential drive by applying the two movable electrodes out of phase signals. This type of application can be visualized from Figure 2.10.

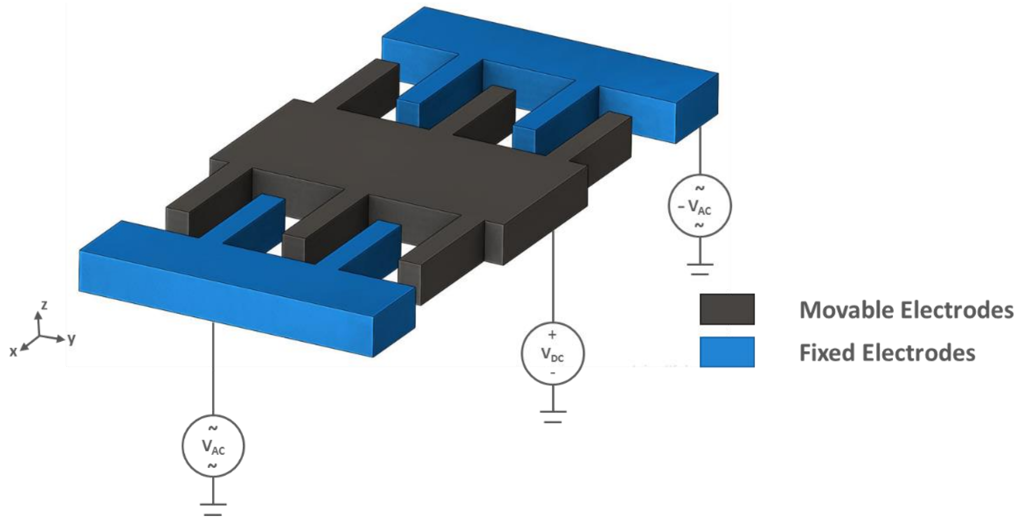

Figure 2.10. The differential drive of varying overlap area type electrodes.

For the differential drive application, the force created by comb fingers,

$$F_x = \frac{n\varepsilon h}{g}(V_{DC} - V_{AC})^2 - \frac{n\varepsilon h}{g}(-V_{DC} - V_{AC})^2 \qquad 2.60$$

If the Equation 2.60 is written in an explicit form,

$$\begin{aligned} F_x = {} & \left[\frac{n\varepsilon h}{g}\left(\frac{{v_{ac}}^2}{2} + {V_{DC}}^2\right)\right] - \left[\frac{n\varepsilon h}{g} 2V_{DC}v_{AC}\, sin(wt)\right] \\ & - \left[\frac{1}{2}\frac{n\varepsilon h}{g} cos(2wt)\right] - \left[\frac{n\varepsilon h}{g}\left(\frac{{v_{ac}}^2}{2} + {V_{DC}}^2\right)\right] \\ & - \left[\frac{n\varepsilon h}{g} 2V_{DC}v_{AC}\, sin(wt)\right] + \left[\frac{1}{2}\frac{n\varepsilon h}{g} cos(2wt)\right] \end{aligned} \qquad 2.61$$

By executing necessary cancellations, the Equation 2.61 turns into,

$$F_x = -\frac{4n\varepsilon h V_{DC} v_{AC}}{g} sin(wt) \qquad 2.62$$

In the derived equation, not only the DC and double frequency terms are canceled out but also the force is doubled at the desired frequency. That provides a neat vibration in the drive mode.

For the actuation of electrodes, it is mainly more advantageous to use varying overlap area type fingers because one can easily notice that it is more linear than varying gap types. However, while increasing the linearity, the sensitivity is reduced. On the other hand, in the sense mode, varying gap type electrodes are more advantageous. The displacements that are occurred in the sense mode should be able to be detected by the electrodes. Since the established displacement is really small, the sensing ability should also be able to detect such a small displacement. That is why it is desired to have varying overlap area type electrodes in the sense mode because they are more sensitive as can be seen in Equation 2.54. Although the non-linearity behavior of this type of electrodes is challenging, the occurred displacement due to Coriolis force is in the order of a few Angstroms. That is much smaller than the capacitive gap. So that, it can be behaved as a linear in such a small portion of a non-linear graph. Figure 2.11 demonstrates the varying gap type electrodes that are used in the sense mode.

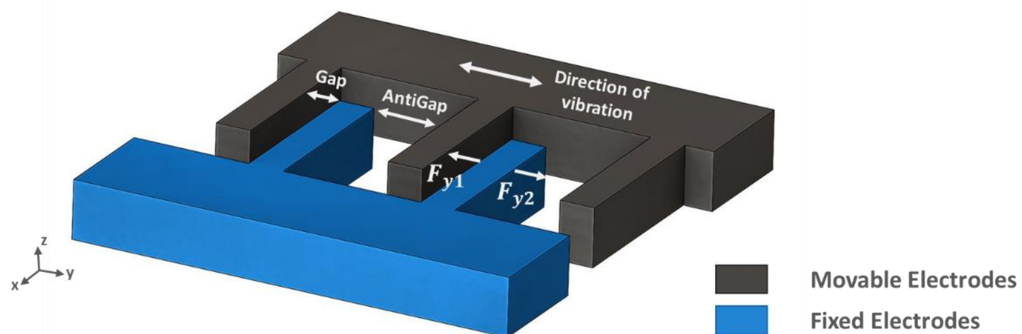

Figure 2.11. Visualization of varying gap type electrodes.

The capacitive sensing mechanism is relayed on converting the displacement of capacitive electrodes to voltage output. The current passing through due to the change of the capacitance between the movable and fixed electrodes can be monitored and that current can be converted to voltage with an op-amp. That conversion will be discussed in CHAPTER 5. The general expression of the current passing through the linear capacitors is,

$$q = CV \quad 2.63$$

$$i = \frac{\partial q}{\partial t} = \frac{\partial (CV_{DC})}{\partial t} = \frac{\partial C}{\partial t} V_{DC} + \frac{\partial V_{DC}}{\partial t} C \quad 2.64$$

In Equation 2.63-2.64, q is the charge in the capacitors, C is the capacitance, and V is the potential difference between the capacitor plates. In this case, V is inserted as V_{DC} because it is applied to the proof mass as indicated in Figure 2.10. Note that, the second portion of the equation can be denied since the time derivative of the V_{DC} is zero. So that, the current is directly related to the change in the capacitance. Then the equation turns into,

$$i = \frac{\partial C}{\partial x} \dot{x} V_{DC} \quad 2.65$$

Since the movable mass is also a vibrating mass,

$$x = A\, sin(wt) \quad 2.66$$

The output current then,

$$i = \frac{\partial C}{\partial x} A w V_{DC}\, cos(wt) \quad 2.67$$

Equation 2.67 shows that the output current amplitude is a function of the vibration frequency of the sense mass and there is a 90° phase between x and i. It can also be noticed that the magnitude of the capacitance change with the physical displacement amplifies the output current. These are all help to increase the sensitivity of the gyroscope. Beside from these, designing the two plates with gap and anti-gap lets the system have a reduced capacitance per length but, otherwise the chance of capacitance in each side would cancel each other. Therefore, the capacitors are designed to be closer to one side to decrease the anti-gap capacitor effect. It can also be understood with the force equation of the varying-gap type electrodes. Equation 2.54 can be simplified by assuming $y \ll D_{Gap}$,

$$F_{y,net} = F_{y1} - F_{y2} = \frac{1}{2} \alpha \varepsilon_0 n H_0 L_0 \left[\frac{1}{{D_{Gap}}^2} - \frac{1}{{D_{Anti-Gap}}^2} \right] {V_{DC}}^2 \quad 2.68$$

Equation 2.68 shows that it is generated a net force between the capacitors and that force can be adjusted with the V_{DC}. This force helps to adjust the drive and sense

oscillating frequencies to the mode-match case as discussed before. The generated force can be modelled as an electrostatic spring. That phenomenon is called as "electrostatic spring effect" or "negative spring". It can be achieved by taking derivative of the Equation 2.54 with respect to y,

$$k_e(y) = \frac{\partial F}{\partial y} = -\frac{\varepsilon_0 H_0 L_0}{(G_0 - z)^3} {V_{DC}}^2 \qquad 2.69$$

Note that Equation 2.69 is very non-linear. However, it can be linearized for small y displacements with respect to gap, G_0.

$$k_e(y) = \frac{\partial F}{\partial y} = -\frac{\varepsilon_0 H_0 L_0}{{G_0}^3} {V_{DC}}^2 \qquad 2.70$$

The reason of the electrostatic spring is also called as negative spring is the negative sign in the equation. Unlike the ordinary mechanical springs, it tries to pull each other electrodes and tends to increase with the increasing y. Since the electrostatic spring also affects the total spring coefficient and resonance frequency of the sense mode also, the resonance frequency can be calculated with respect to the effective spring constant. The effective spring constant equals to,

$$k_{eff} = k_{mech} - k_e \qquad 2.71$$

$$k_{eff} = k_{mech} - \alpha \varepsilon_0 n H_0 L_0 \left[\frac{1}{(D_{Gap} - y)^3} - \frac{1}{(D_{Anti-Gap} + y)^3}\right] {V_{DC}}^2 \qquad 2.72$$

Then the sense mode resonance frequency can be expressed as,

$$w_s = \sqrt{\frac{k_s}{m_s}} = \sqrt{\frac{k_{mech} - \alpha \varepsilon_0 n H_0 L_0 \left[\frac{1}{(D_{Gap} - y)^3} - \frac{1}{(D_{Anti-Gap} + y)^3}\right] {V_{DC}}^2}{m_s}} \qquad 2.73$$

It should be noted that in the sense mode the static electrostatic force will cause a deflection on the structure. Moreover, there is a specific V_{DC} at which the electrostatic spring reaches the mechanical spring at magnitude. After that point, the

electrodes can be collapsed onto each other which is called pull-in. That voltage can be calculated by equating the mechanic and electrostatic spring constants force to each other. It is expressed in [24],

$$F_e + F_{mech} = 0 \tag{2.74}$$

$$V_{Pull-in} = \sqrt{\frac{8k_s {D_{Gap}}^3}{27\alpha\varepsilon_0 H_0 L_0}} \tag{2.75}$$

2.5 Summary

In this section, the working principles of the drive and sense mode are presented. The overall acceleration terms and method of rejecting the unwanted ones are explained. Moreover, electrostatic actuation and sensing methods are analysed. Electrostatic forces, their effects on the body are shown. The electrostatic spring effect and its advantages are explained.

CHAPTER 3

DESİGN OF VIBRATORY MEMS GYROSCOPE

In this chapter, the design parameters of the gyroscope and fabrication steps are presented. In Section 3.1, flexure elements that are used in the gyroscope are examined. Their use of advantages and equations that will help to model the gyroscope is clarified. In Section 3.2, electrostatic force compensation and tuning methods and their function in the gyroscope are explained. In Section 3.3, FEM analysis of the primary modes and near mode shapes that can affect the drive and sense modes are shown. In Section 3.4, the overall fabrication process is presented step by step. Parameters that are used and problems encountered in the fabrication are explained, in detailly. Lastly, Section 3.5 briefly summarizes this chapter.

3.1 Flexure Elements

Flexure elements provide suspension for the gyroscope to vibrate in the desired directions. They are one of the main decision elements of the sensitivity, operational frequency, and many others. There are so many options for a flexure element in terms of its shape and connection types in the literature. However, double-folded single-sided flexures are preferred due to their linearity in a wide working range.

Beside from that, flexure elements also provide decoupling of the sense and drive electrodes. It behaves like a roller and isolates the drive and sense mode from each other. So that, while the proof mass has 2 degrees of freedom movement capability, sense and drive electrodes have only one.

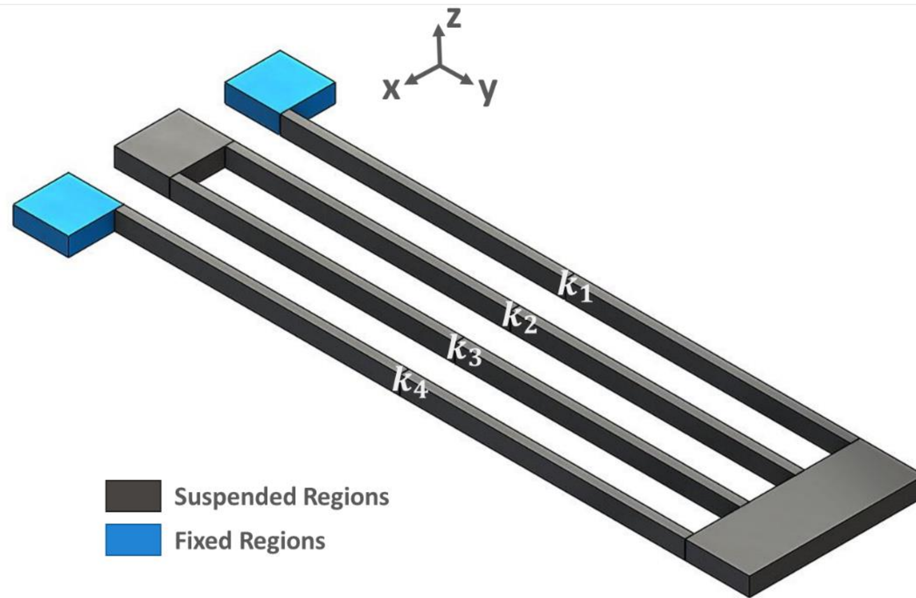

Figure 3.1. The double-folded single-sided flexure element.

The double-folded single-sided flexures can be seen in Figure 3.1. All four beams are connected to an upper truss which is assumed to be rigid. That means, under an applied force, four beams are presumed to have the total deflection. While there is a series connection between inner and outer beams, each pair are connected parallel to each other, $k_1//k_4 - k_2//k_3$. In that way, the overall spring constant can be calculated as,

$$\text{Assuming } k_1 = k_2 = k_3 = k_4 = k \qquad 3.1$$

$$k_t = \left[\frac{1}{k_1 + k_4} + \frac{1}{k_2 + k_3}\right]^{-1} = k \qquad 3.2$$

Although the overall spring constant is equal to the spring constant of a single beam, the spring constant calculation of that single beam is a little tricky. In Figure 3.2 the shape of a double-folded single-sided flexure can be observed while deflected. Every single beam can be modelled as two beams which have a fixed-end beam with concentrated load boundary conditions. That means every single beam on the spring consists of a two-unit beam connected serially.

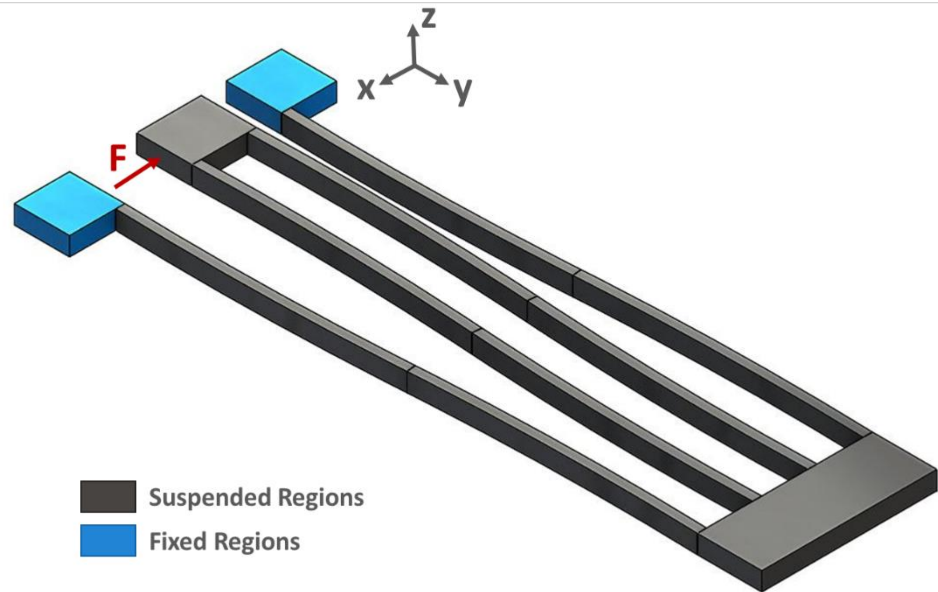

Figure 3.2. Deflected double-folded single-sided flexure element.

In Figure 3.3 a cantilever beam with a concentrated load boundary condition is illustrated. For a cantilever beam that is loaded at the end of its length, the deflection can be calculated as [27],

$$y = \frac{Fx^2}{6EI}(x - 3L) \tag{3.3}$$

In the above equation (Equation 3.3), y stands for the amount of deflection with respect to distance from the fixed point which is represented by x. F is the applied concentrated force, E is the elastic modulus of the material, which is silicon in this case, and I represent the area moment of inertia. The maximum deflection occurs at the end of the beam so that,

$$x = L_u \tag{3.4}$$

$$y_{max} = -\frac{F{L_u}^3}{3EI} \tag{3.5}$$

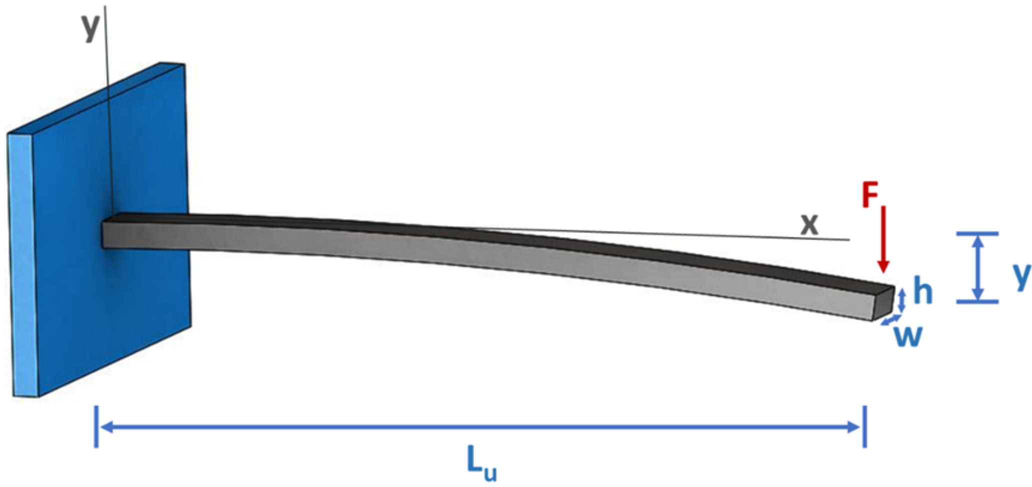

Figure 3.3. Cantilever beam with a concentrated load boundary condition.

The spring constant of a concentrated end load cantilever beam can be calculated as,

$$k_{unit} = \frac{F}{\lambda_{max}} \tag{3.6}$$

$$k_{unit} = \frac{3EI}{{L_u}^3} \tag{3.7}$$

Since every single beam on the double ended single-sided flexure element is consist of two-unit beams which is connected serially,

$$k_{beam,x} = k_x = \frac{k_{unit,x}}{2} \tag{3.8}$$

$$k_x = \frac{3EI_x}{2{L_u}^3} \tag{3.9}$$

Total length of the unit beam is $L_u = L/2$ then,

$$k_x = \frac{12EI_x}{L^3} \tag{3.10}$$

The overall spring constant is equal to the spring constant of the beam as proved in Equation 3.2,

$$k_{t,x} = \frac{12EI_x}{L^3} \tag{3.11}$$

where,

$$I_x = \frac{1}{12} h w^3 \quad 3.12$$

Note that, the spring constant in the z-direction is depend on the same mechanics as in the x-direction. Only the area moment of inertia should change with respect to the related axis.

$$k_{t,z} = \frac{12 E I_z}{L^3} \quad 3.13$$

where,

$$I_z = \frac{1}{12} w h^3 \quad 3.14$$

However, in the y-direction, the calculation of the spring constant is different. Every single beam spring constant of an axially loaded beam is [27],

$$k = \frac{AE}{L} \quad 3.15$$

where A represents cross section area of the beam,

$$A = hw \quad 3.16$$

The overall spring constant of the double-folded single-sided flexure element in the y-direction is again equal to the spring constant of the single beam as in Equation 3.2. Then, the spring constant in the y-direction is,

$$k_{t,y} = \frac{Ehw}{L} \quad 3.17$$

Notice that, the overall spring constant along y-direction is much larger than in the other directions. Therefore, it is assumed that the double-folded single-sided flexure elements behave like a roller in the system because deflection in the y-direction is nearly zero. That property allows designing of a decoupled drive and sense mechanisms. So that, the continuous vibration of the drive mode affects the sense mode in a minimized way. Besides from that, this type of flexure element is free to move in the y-direction. That means the beams can expand freely and can relieve the thermal stress on the flexure elements. This property is also as important as the decoupling. The operational frequency will be steadier.

3.2 Electrostatic Force Compensation and Tuning Electrodes

In the layout of a device, although every unit is placed as if perfectly matching, there will be fabrication imperfections that will cause an imbalance in the structure. Despite the advanced optimization of process parameters, non-uniform etch is always present in the fabrication process. Beside from that, the change in the environmental conditions influences the characteristics of the device. These may lead mismatch in the resonance frequencies, unbalanced forces on the device and etc. Therefore, there is a need for correcting these errors and tuning the frequencies of the structure to maximize its performance.

3.2.1 Forced Feedback Electrodes

The main idea of the forced feedback electrodes is generating a force that counteracts the sense mode displacement due to Coriolis force. The displacement of the sense body is suppressed so that the sense mass cannot move. That feature improves the scale factor of the rate output [24], [28]. Since the potential voltage that is required to generate the stopping force is proportional to the Coriolis acceleration on the body, it is used as an output of the system. Therefore, the overall sense mass is controlled in a closed-loop system.

3.2.2 Quadrature Cancellation Electrodes

In MEMS fabrication, unfortunately, the processes are rarely perfect despite the best human efforts. The pattern transfer may not be proper, mask generation may lead to some errors, sidewalls of the DRIE process will not be perfectly vertical or smooth [26]. Consequently, the manufactured body may suffer from these fabrication errors. In the drive mode, the continuous unbalanced vibration of the body may couple into sense mode. Figure 3.4 illustrates this coupling due to uneven suspension in each side. That is called quadrature error and it is one of the main obstacles for better

gyroscope performance especially for bias instability and angle random walk (ARW) [24]. Therefore, quadrature cancellation electrodes are designed to decrease these errors as soon as possible.

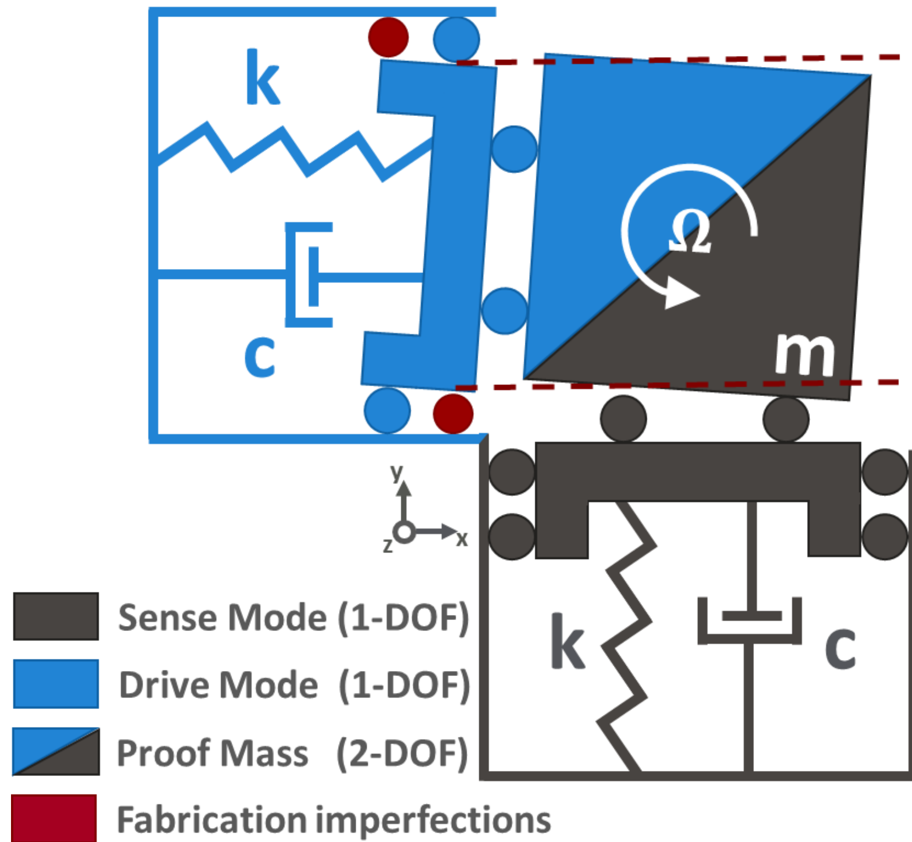

Figure 3.4. Visualization of quadrature errors.

Quadrature cancellation electrodes work as varying gap electrodes and generate an electrostatic force against the quadrature error. That force helps to correct the drive mode vibration and reduces the coupling to the sense mode.

3.2.3 Sense Frequency Tuning Electrodes

A negative spring effect can be used for tuning the structure to operate the system in the desired frequency which is most probably natural frequency for gyroscopes. The negative spring effect can be considered as softening the total stiffness. Therefore,

changing the applied voltage of the frequency tuning electrodes will change the total stiffness so that it will change the whole system's natural frequency. In this way, electrodes can be tuned. Generally, the stiffness of the springs is designed for natural frequencies, perfectly. However, due to fabrication errors, unpredictable damping or etc., these frequencies deviate and change the behaviour of the structure. Frequency tuning helps to regain the operational frequency to operate in designed frequency by adjusting the attraction force of the electrodes. For these reasons, operational frequencies are designed above the desired operational frequency. That is because the tuning electrodes only soften the springs. Therefore, the sense frequency tuning process also plays an important role to increase sensitivity.

Sense frequency tuning electrodes are used mainly tuning the sense mode frequency to the drive mode frequency for mode matching. Actually, it is also possible to match these frequencies by adjusting the proof mass voltage. However, changing proof mass voltage is undesired because it will also affect the characteristics of the system [22].

3.2.4 Drive Frequency Tuning Electrodes

The electrostatic spring effect can be modelled as stiffness by taking the derivative of the electrostatic force as in Equation 2.70. However, taking the derivative of electrostatic force in x and z-directions equals zero. That means for varying overlap area electrostatic spring effect is not found [24]. Unfortunately, using varying gap types is not desired for drive mode due to excessive vibration displacements. Designing the drive frequency electrodes as a comb triangle that provides varying finger lengths may be a solution for that problem [29]. The triangular shape of comb arrays allows varying the number of fingers which is provided by the varying lengths of fingers. That feature enables to generate a force in the drive frequency tuning electrodes that provides tuning ability to the system.

3.3 Finite Element Analysis

The finite element analysis of the designed structure is simulated in a COMSOL environment. The primary resonant mode shapes are analysed and optimized, iteratively. The analyses are realized excluding the finger structures due to the simplicity of the model. However, their masses are added to the bodies where they are attached to for the accuracy of the analyses.

Figure 3.5 illustrates the drive mode shape and the frequency of the designed gyroscope. Drive mode frequency is designed as the first mode shape with the lowest frequency. The double mass is coupled with a diamond spring in the drive mode to equate their motion. That coupling also ensures out of phase motion has a lower frequency than the in-phase motion. As stated in CHAPTER 2, the gyroscope is designed to be operated in out of phase due to rejecting feature of acceleration terms other than Coriolis acceleration.

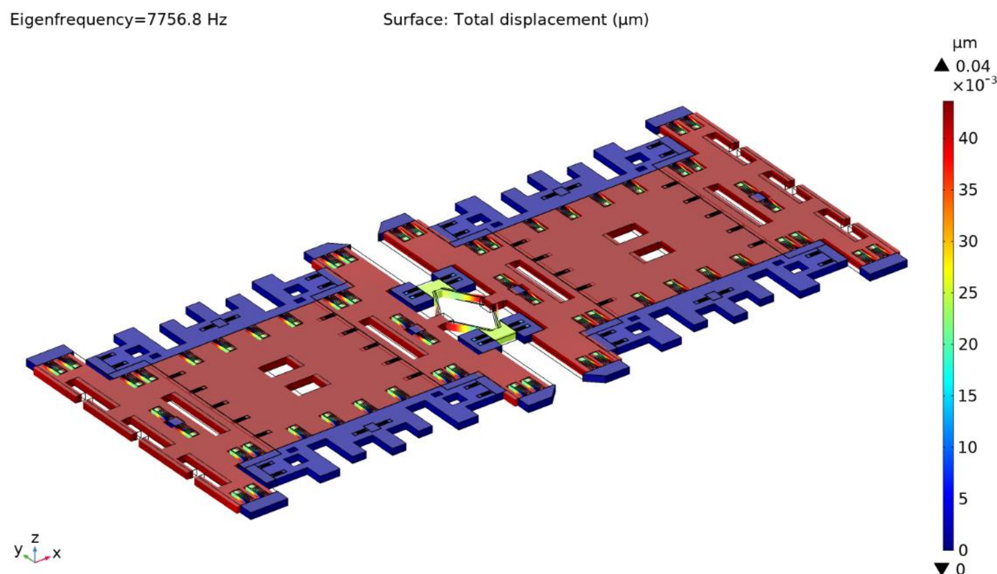

Figure 3.5. Drive mode shape of the gyroscope.

In Figure 3.6, the sense mode shape of the gyroscope is shown. Due to the lack of coupling mechanism in the sense mode shapes are two separate modes in the analysis. Although both masses are designed to be identical, little differences in the

node analysis made a small difference in their frequencies. The sense mode frequency is designed to be a little bit higher than the drive mode for operating the gyroscope in mode matched. That difference will disappear with the electrostatic spring back effect and the frequency tuning electrodes will make the fine-tuning.

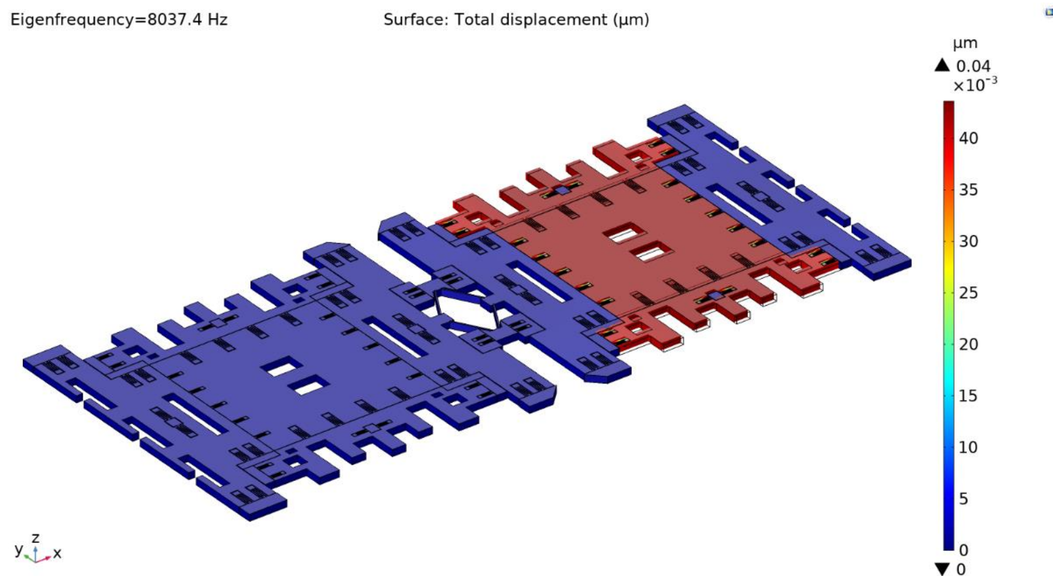

Figure 3.6. Sense mode shape of the gyroscope.

The mode shapes that are close to operational frequencies are also studied. Figure 3.7 shows the near mode shapes to the operational frequencies. They are designed to be far enough to the operational frequencies. Notice that, in Figure 3.7 (b) the delayed in phase mode due to the coupling mechanism can be seen.

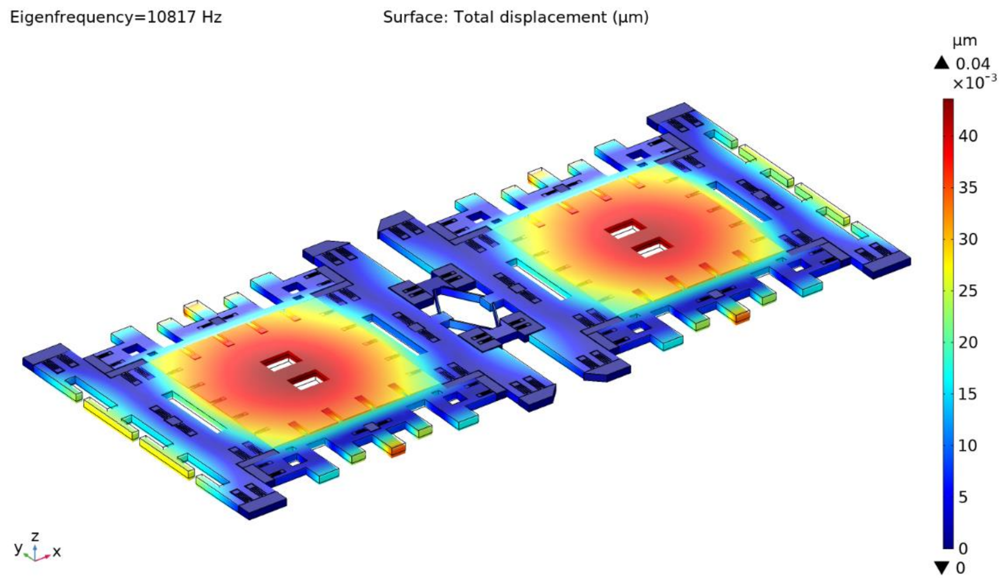

(a)

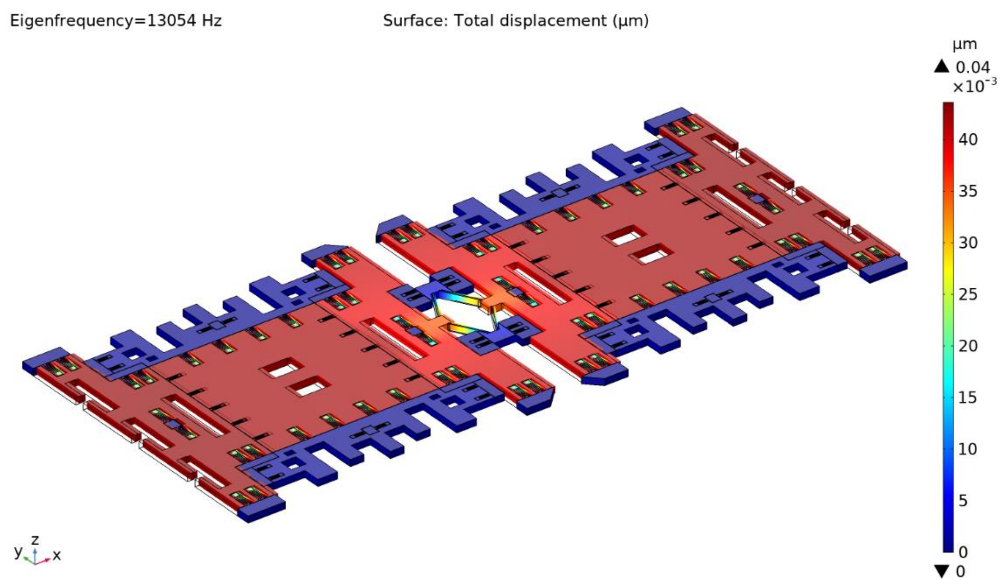

(b)

Figure 3.7. Near mode shapes to the operational frequencies, (a) out of plane mode shape and (b) in-phase mode shape of the gyroscope.

3.4 Fabrication

The overall fabrication process of the gyroscope can be summarized in Figure 3.8. The fabrication process starts with a piranha cleaning (1:1, Sulfuric Acid: Hydrogen Peroxide, H_2SO_4:H_2O_2) so that contamination is minimized.

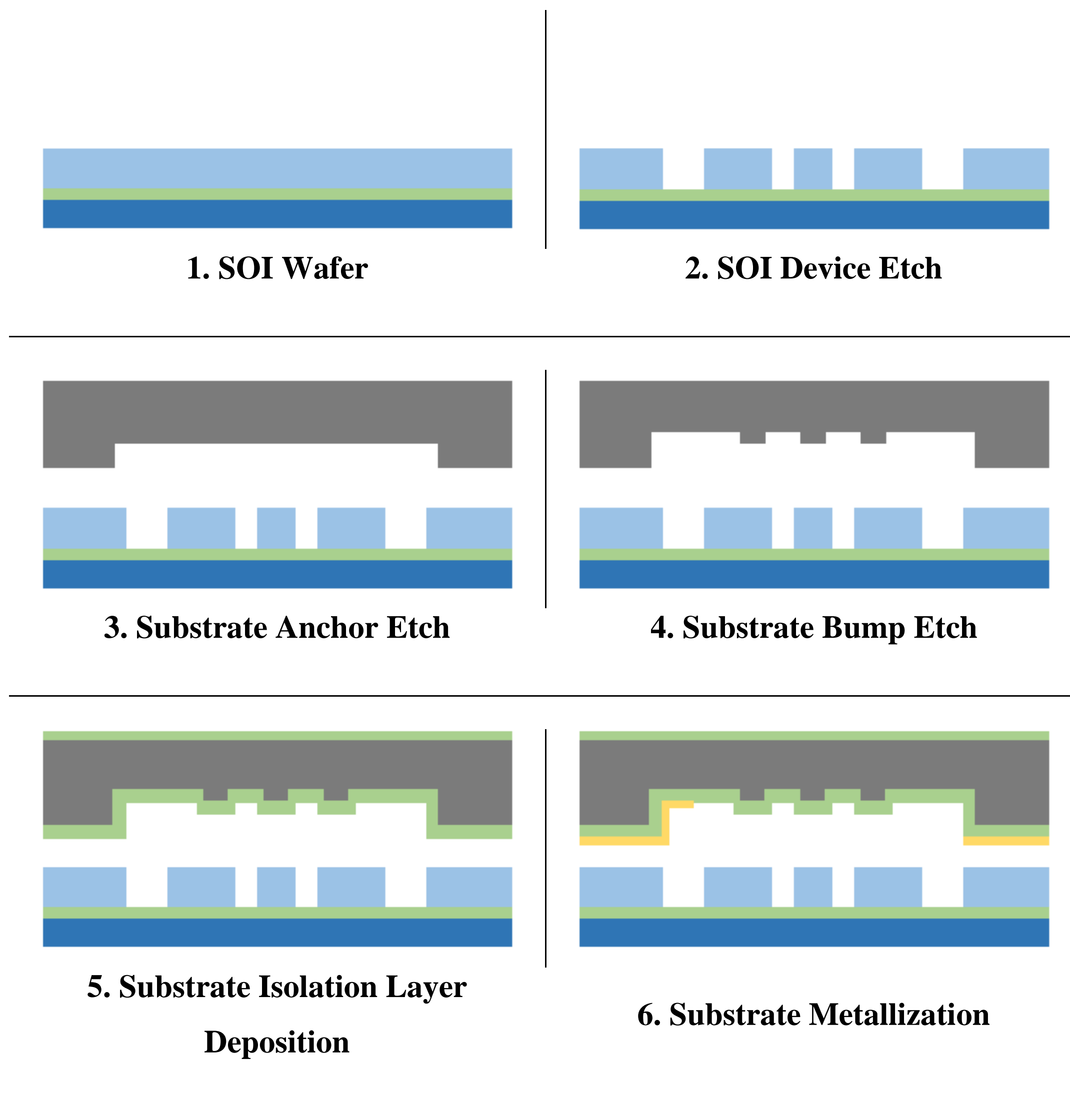

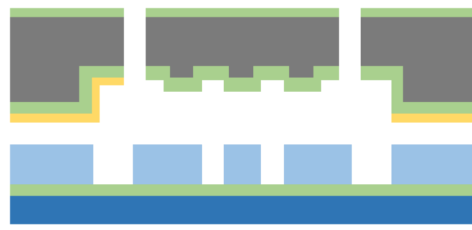

7. Substrate Through Hole Etch

8. Eutectic Bonding

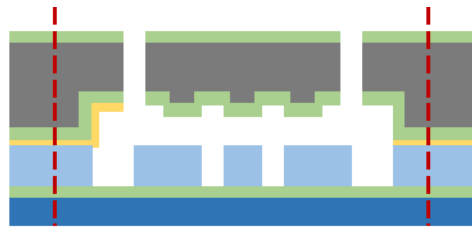

9. Dicing

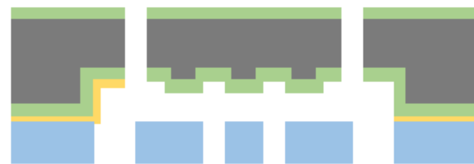

10. Handle Layer Removal & Releasing

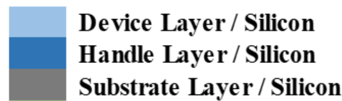

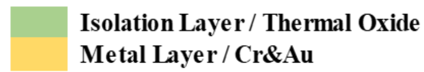

Figure 3.8. The overall fabrication process of the gyroscope.

Later, a 400 µm device layer (<0.005 Ω-cm, p++ type, <111>), 1 µm buried oxide and 100 µm handle layer (<0.005 Ω-cm, p++ type, <111>) SOI wafer is used to form the device. However, achieving a 400 µm deep silicon etch is not an easy task. While forming the deep structures, the wafer is exposed to plasma long time so that a thick hard mask which consists of 1 µm thermal oxide and SPR 220-7 PR (Photoresist), is used on the device side. Then, the wafer is etched by DRIE (Deep Reactive Ion Etching) with a high aspect ratio recipe. In the DRIE process, the width of the trenches affects the etch rate. While wider gaps etch faster, narrow gaps make it slow. That is called DRIE Lag [30]. 1 µm buried oxide in the SOI wafer provides an etch stop layer so that, the narrow gaps can reach the wider gaps by means of depth. In Figure 3.9, the visualization of the buried oxide underneath the device layer is illustrated after the device etch is completed.

Achieving 400 microns depth etches is another issue for the gyroscope. Unlike the conventional gyroscopes, the gyroscope that is used in this thesis needs nearly 10 times deep etches. A new recipe that can handle this requirement is developed and optimized for that reason. However, while achieving such deep etches, the platen power of the DRIE needs to be higher than 150 W which also leads poor side wall scallop profile and buried oxide etch of the SOI wafer. Those problems will be discussed, later.

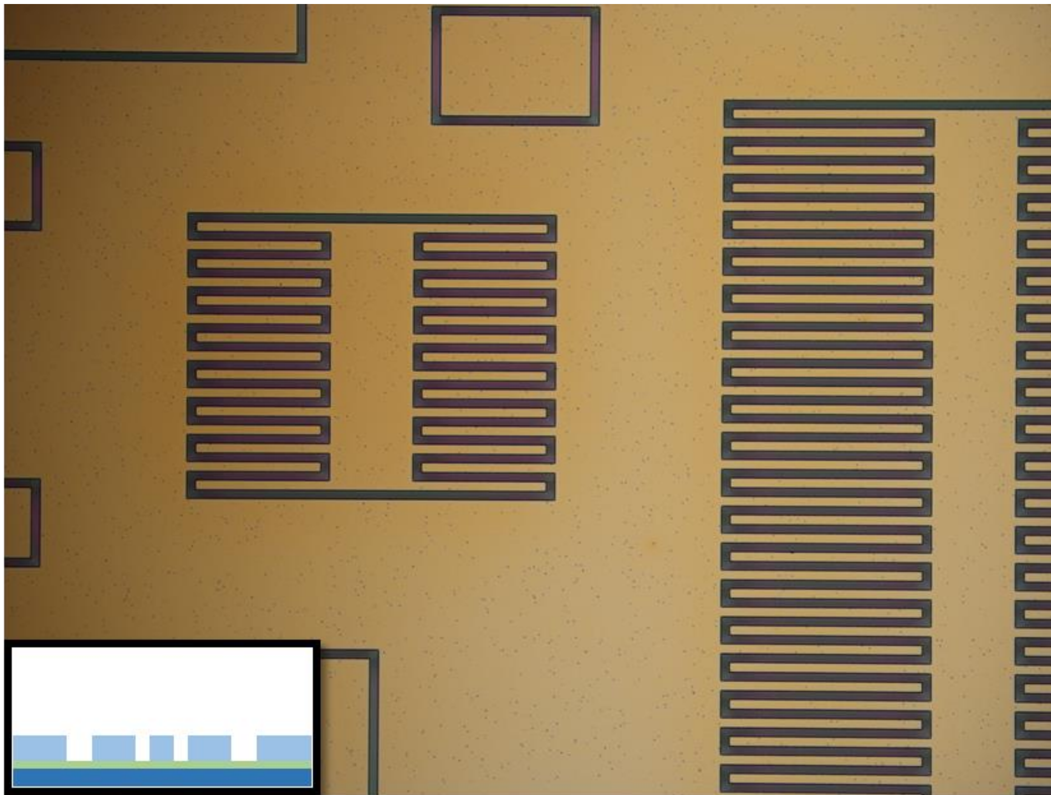

Figure 3.9. The visualization of buried oxide after 400 microns device etching.

The third step begins with a DSP (Double Side Polished) substrate wafer. It is a p-type, standard low resistive (<0.005 Ω-cm), <111> oriented wafer. A substrate wafer is used for fixing the required structures and carrying the necessary electrical connections. The substrate wafer is coated with PR as a masking layer. Around 8 μm anchor height is etched by DRIE so that, while maintaining the fixed structures on the anchor points, the suspended masses would move freely. With the fourth step, 2-

3 microns substrate bump etch is realized in the same manner. The bumps provide a higher surface from the metallization which will be deposited in the sixth step. Therefore, in the bonding step, if the suspended body deflects, the possibility of the stiction to the substrate wafer is minimized because the bumps will keep away the suspended mass from the metal lines. In Figure 3.10, an SEM image of the substrate wafer after anchor and bump are etched can be seen.

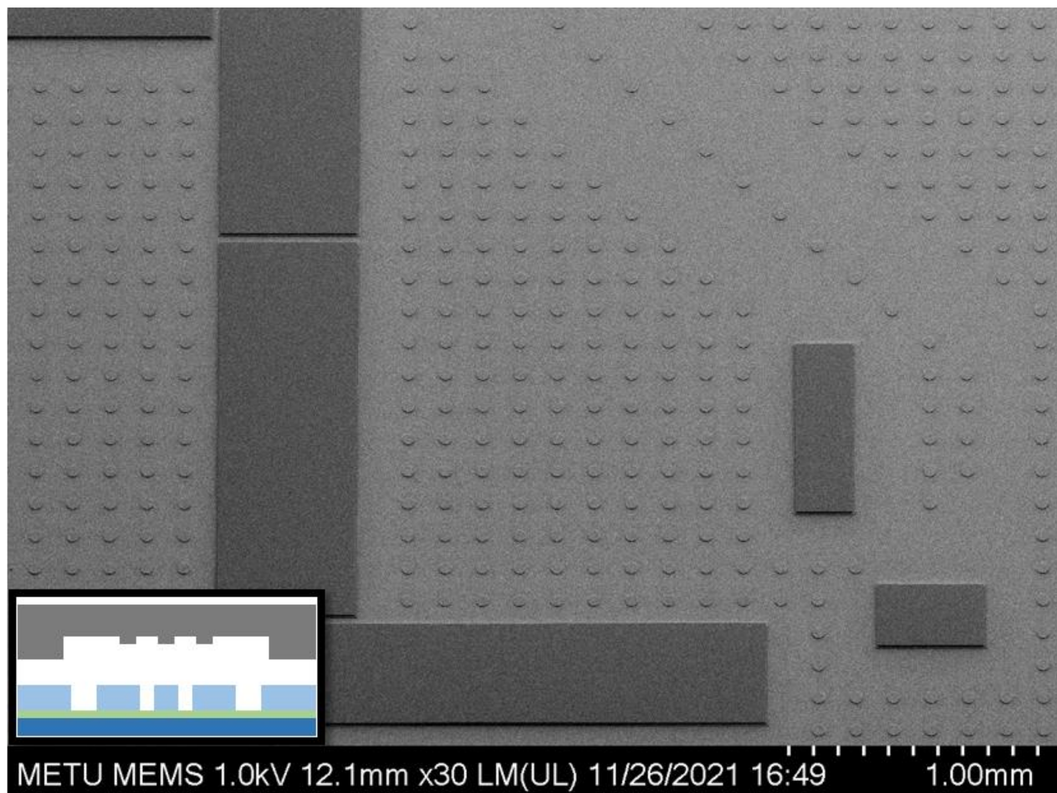

Figure 3.10. SEM image of the substrate wafer after anchor and bump are etched.

Later, a thermal oxide is grown as the isolation layer. Before it, an additional cleaning process is also required. This cleaning step includes RCA1 and RCA2 solutions. At 1000 °C thermal oxidation step is applied to grow 1.5 μm SiO2. This layer provides isolation between the metal lines that will be formed in the next step. The thermal oxide also grows on the surface of the bumps so that the stiction of the suspended mass to the bumps can be prevented. Au is used as a metal connection line but, the adhesion of the gold on the silicon oxide is not reliable. Therefore, before the 300 nm Au deposition, 50 nm Cr is deposited to increase that bond strength. The

deposition process is made with a sputtering system. However, since the anchor step is formed by DRIE, there will be perpendicular 8 μm steps for the metal connections. The metal deposition must cover all the anchor topsides and maintain the connection with the contact pads. Therefore, in the metal mask that lines are designed wider in the points of the anchor joints to prevent electrical disconnections. In the fabrication, anchors could also be formed via a wet etch process. That provides the metal line a sloping road, not a steep one. On the other hand, the metals could be deposited with an evaporator. That would also compensate the disconnection probability because despite sputtering, evaporation has better sidewall coverage due to non-directional deposition. However, in the fabrication step, it is more practical to use DRIE for the anchors and sputter technique for the metallization in the METU MEMS Center. After the deposition of the metals, the metal mask is used to give form the required metal lines. SPR 220-7 PR is patterned on the surface of the wafer and hard-baked at 120 °C for about 30 minutes with the ramp-up time is included. That step is essential to increase the durability of the PR mask because a wet etch is realized to the wafer. First, the Au deposition and then Cr is etched in the beakers with commercial Au and Cr etchant, respectively. Then, the PR masked is cleaned with O2 plasma and PRS 2000 solution. Figure 3.11 illustrates the metallization of the substrate wafer.

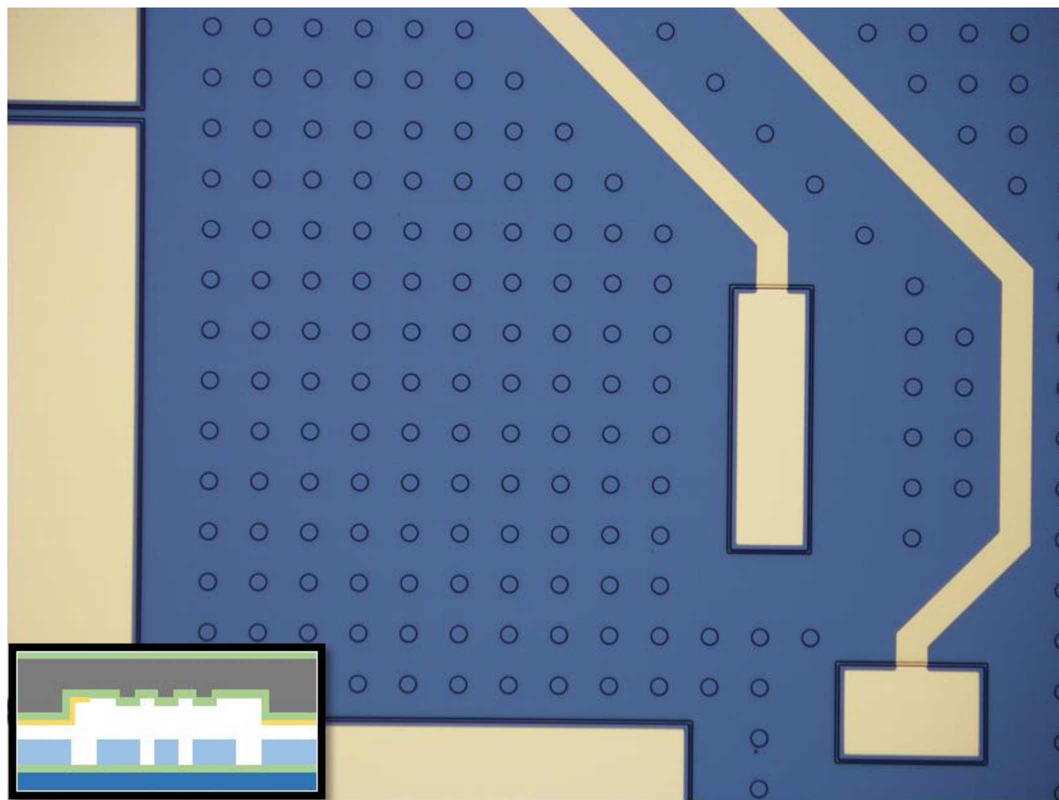

(a)

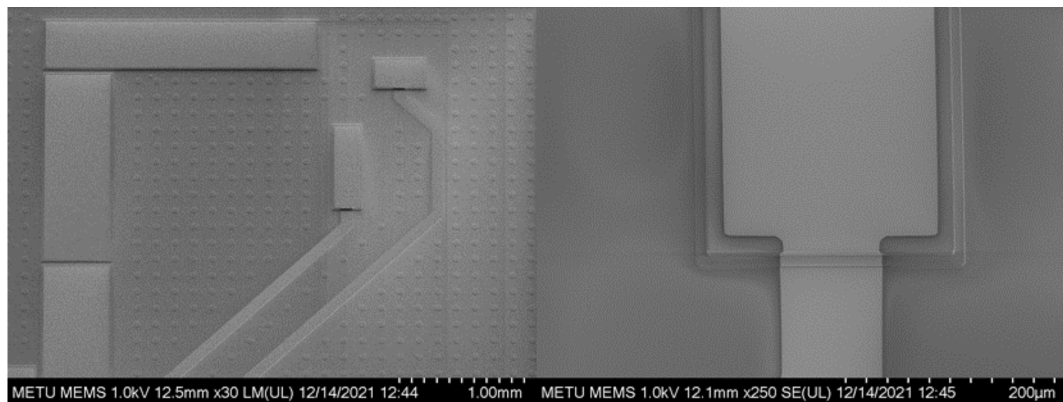

(b) (c)

Figure 3.11. Microscope image (a) and SEM images (b) & (c) of the substrate wafer after metallization.

The last mask that will be implemented on the substrate wafer is for forming the through-holes. 2000 μm x 1600 μm rectangle holes are required for the capacitive enhancement pins to reach the device layer from the bottom side of the wafer. Again, an SPR 220-7 PR mask is patterned for this step. Then, the wafer is etched thoroughly

which is around 500 µm thickness with the DRIE. The DRIE machine cools the wafer from the bottom side with helium gas while performing the etches. Otherwise, the wafer etch uniformity would be decreased. However, in the through-hole step sealing the helium gas at the bottom side of the wafer is not applicable due to through-holes. Therefore, an alumina wafer is placed under the substrate wafer for the conservation of the helium pressure. After the through holes are formed, the PR mask is cleaned with O2 plasma and PRS 2000 solution. In Figure 3.12, the through-hole etch on the substrate wafer can be visualized.

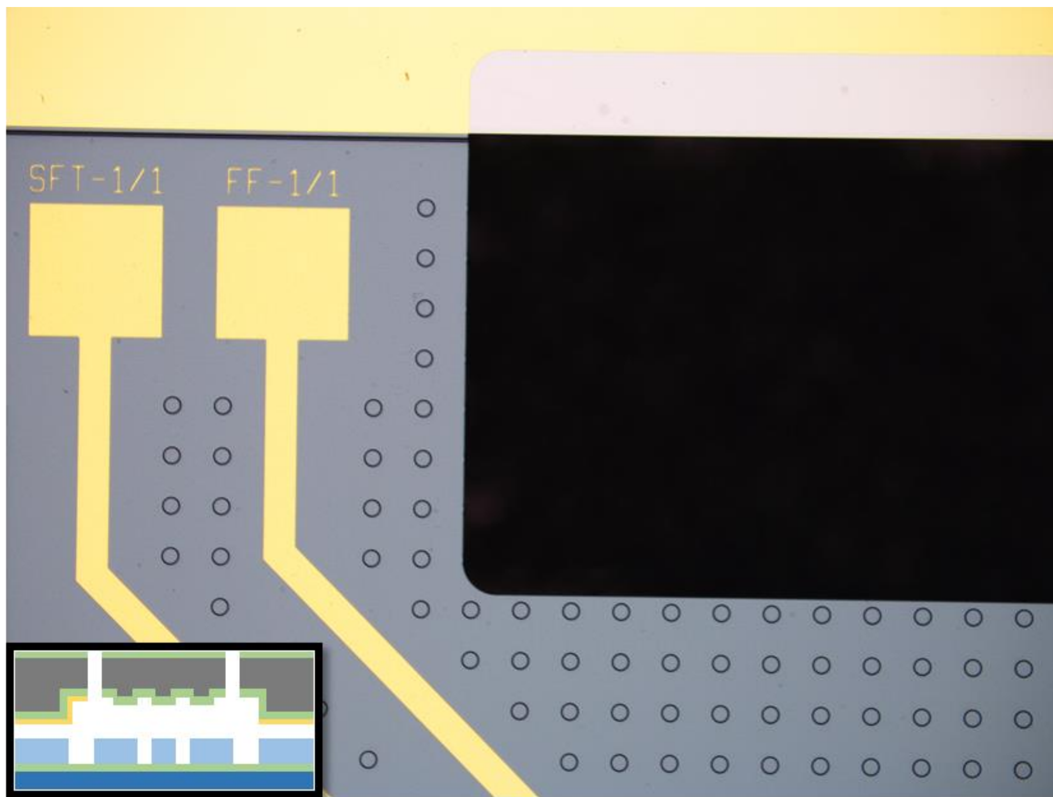

Figure 3.12. Substrate wafer after through-hole is formed.

That was the last step for the substrate wafer preparation and the wafers are ready to bond. Both SOI and substrate wafer are cleaned with a piranha solution (1:1 Sulfuric Acid: Hydrogen Peroxide, H_2SO_4:H_2O_2). However, while the SOI wafer is held in the solution for 30 minutes, the substrate wafer is held for around 10 minutes because the piranha solution attacks the metallization even if the etch rate is low. Later, the

SOI wafer is dipped into the BHF solution (1:5, HF: Peroxide) to remove the oxide on the surface of the wafer. BHF solution also reaches the buried oxide that is exposed after the second step (device layer etch). However, if the oxide on the SOI wafer surface is less than the buried oxide, the duration of the etch would not be enough to complete the etch all of the buried oxide. In the eighth step, Figure 3.13, the SOI and substrate wafer are aligned with EVG 6200 Aligner Machine and transported to the EVG 520 IS Wafer Bonder Machine. Au/Si eutectic bonding is applied at 400 °C with 1.7 MPa.

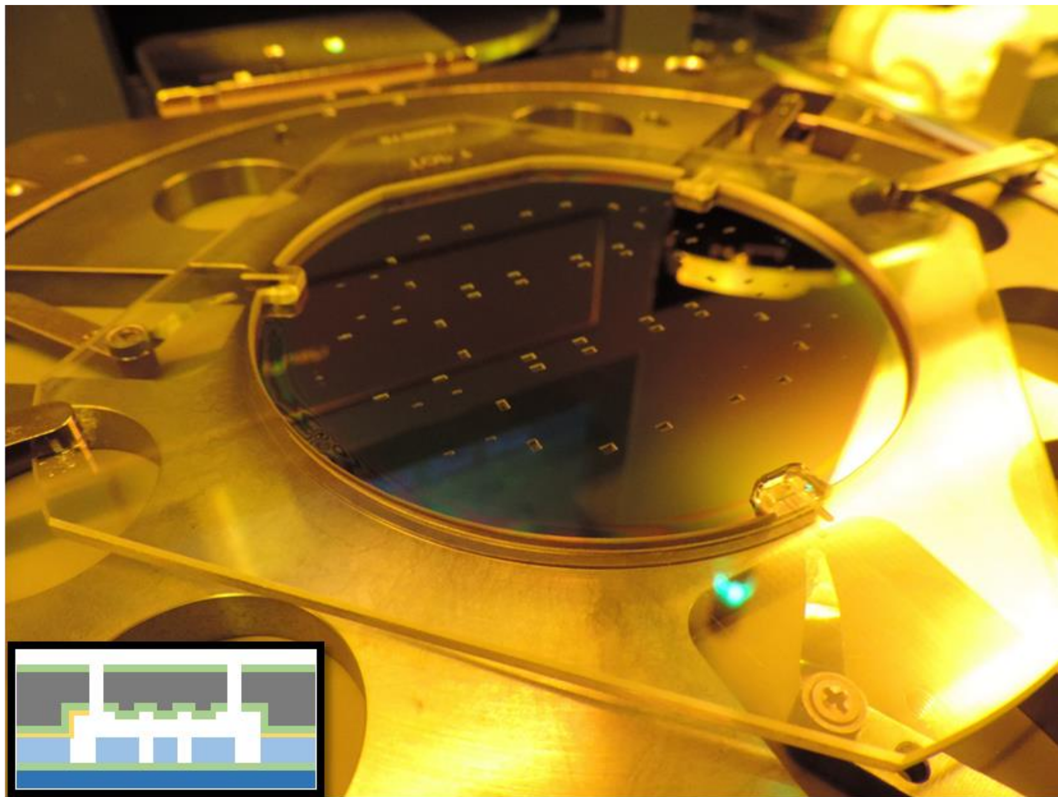

Figure 3.13. The eutectic bonding process.

After the bonding step, the stack wafer is cut to the die sizes. Dicing before the handle layer removal provides better uniformity. Later, handle layer removal must be performed. 100 μm handle layer is etched with DRIE thinning recipe. Again, an alumina wafer is used for helium sealing. Then, the buried oxide of the bonded stack is removed with a BHF solution for releasing the suspended masses on the device.

In that step, BHF will also etch the isolation layer on top of the substrate wafer but, it is not enough to etch all the isolation layer because the isolation layer is thicker than the buried oxide. Moreover, since the buried oxide will cover the isolation layer, it will take time for BHF to reach the isolation layer. However, this process is a wet etch step that will cause stiction problems in the suspended mass. Therefore, after the releasing process, the drying part needs additional steps. When the rinse of the wafer is done, the wafer is washed with the isopropanol alcohol and then with the methanol. After that, the methanol will be evaporated on the hot plate at 80 °C. After all these fabrication steps, the chip is ready for the capacitive enhancement process and then testing.

Before post-processing and characterization, the problems in the fabrication processes and possible sources of it will be discussed. Although the fabrication processes are tried to optimize for the best output, there are some problems due to the nature of the fabrication process itself. First of all, a DRIE recipe that can handle 400 microns deep etch is optimized (Figure 3.14). Different etch and passivation cycles, pressures, coil, and platen powers are ramped for the best output. The main problem behind this task is a complete etch up to the buried oxide for the 12 microns gaps without corrupting the sidewalls of the critical gaps.

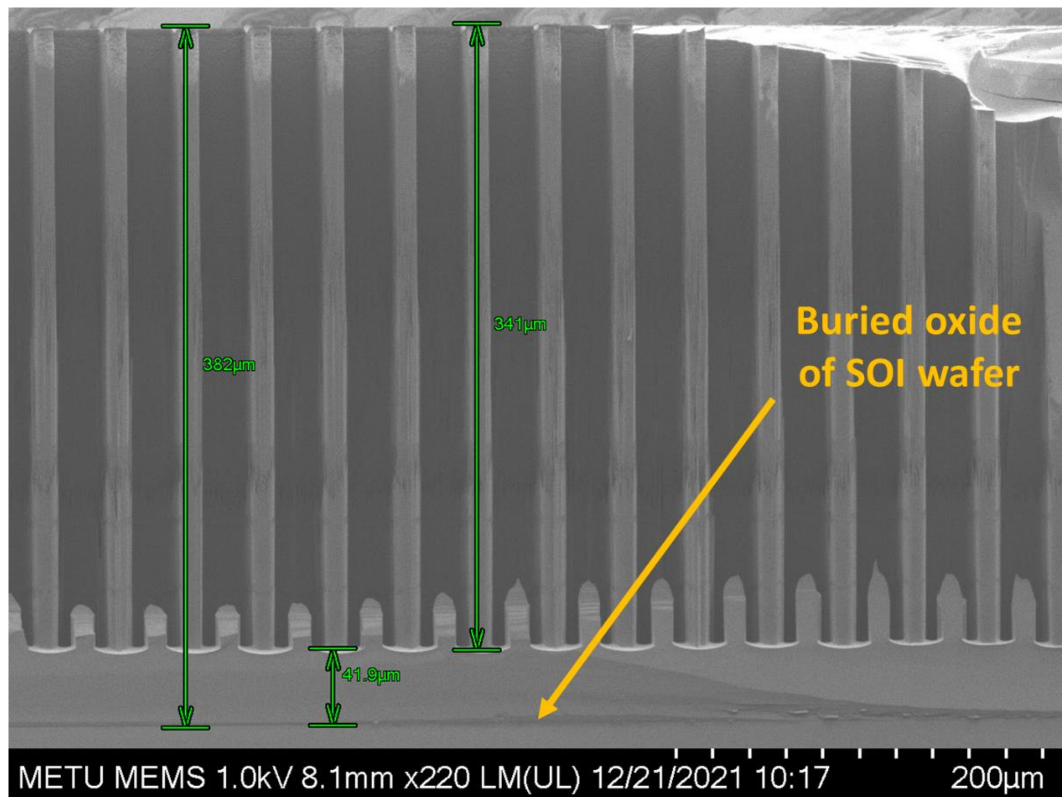

Figure 3.14. DRIE deep narrow etches optimization.

However, after some point realizing deep etches is really hard without sacrificing the aspect ratio. To maintain that ratio, platen power is ramped with a trade-off selectivity. Since the wider gaps etch faster, they reach the buried oxide before the narrow ones. When the high platen powers are exerted, the ions in the plasma are accelerated so powerful that the mechanical etching part starts to etch the buried oxide at the bottom. In Figure 3.15, the end-off buried oxide in the wider gaps after the device etch is completed can be observed. This issue causes a problem in the thinning step. Normally, the buried oxide protects the device from etching while performing thinning. However, if the buried oxide is removed, the device starts to be etched. That may lead to deviations of the designed parameters, even a failure in the device. In Figure 3.16, protection of buried oxide difference in the sense fingers can also be observed. While the upper fingers are thicker due to buried oxide protection, the lower fingers are got thinner in the handle layer removal step.

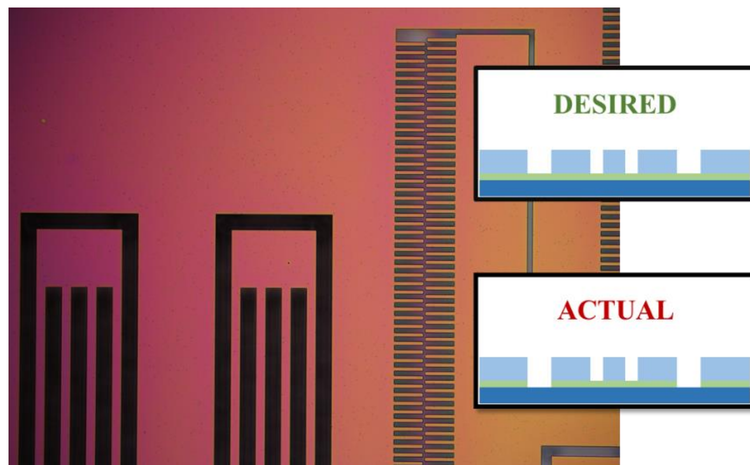

Figure 3.15. End of buried oxide in the wide gaps after the device etch is completed.

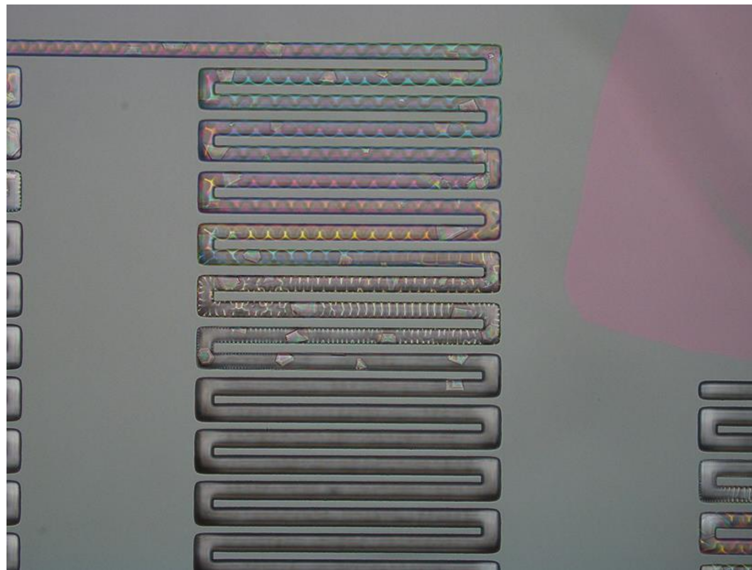

Figure 3.16. Protection of buried oxide difference in the sense fingers.

Beside from end of the buried oxide problem, realizing deep etches requires extended etch durations. After some point, the ramped etch cycles start to defeat the protection layer of the deposition cycle. As a result of this, the side walls break down and the capacitive gaps get wider than designed. Figure 3.17 shows an SEM image from the drive fingers which has designed 20 microns thickness and 24 microns gap before the enhancement process. The sidewall breakdowns can be seen clearly, also. Moreover, in Figure 3.18 a cross-section view of a bonded stack can be visualized.

The designed value for the width of the drive mode springs is 50 microns. These thinned structures lead to deviations in the resonance frequencies and loss of performance due to widened and damaged sidewalls in the capacitive gaps.

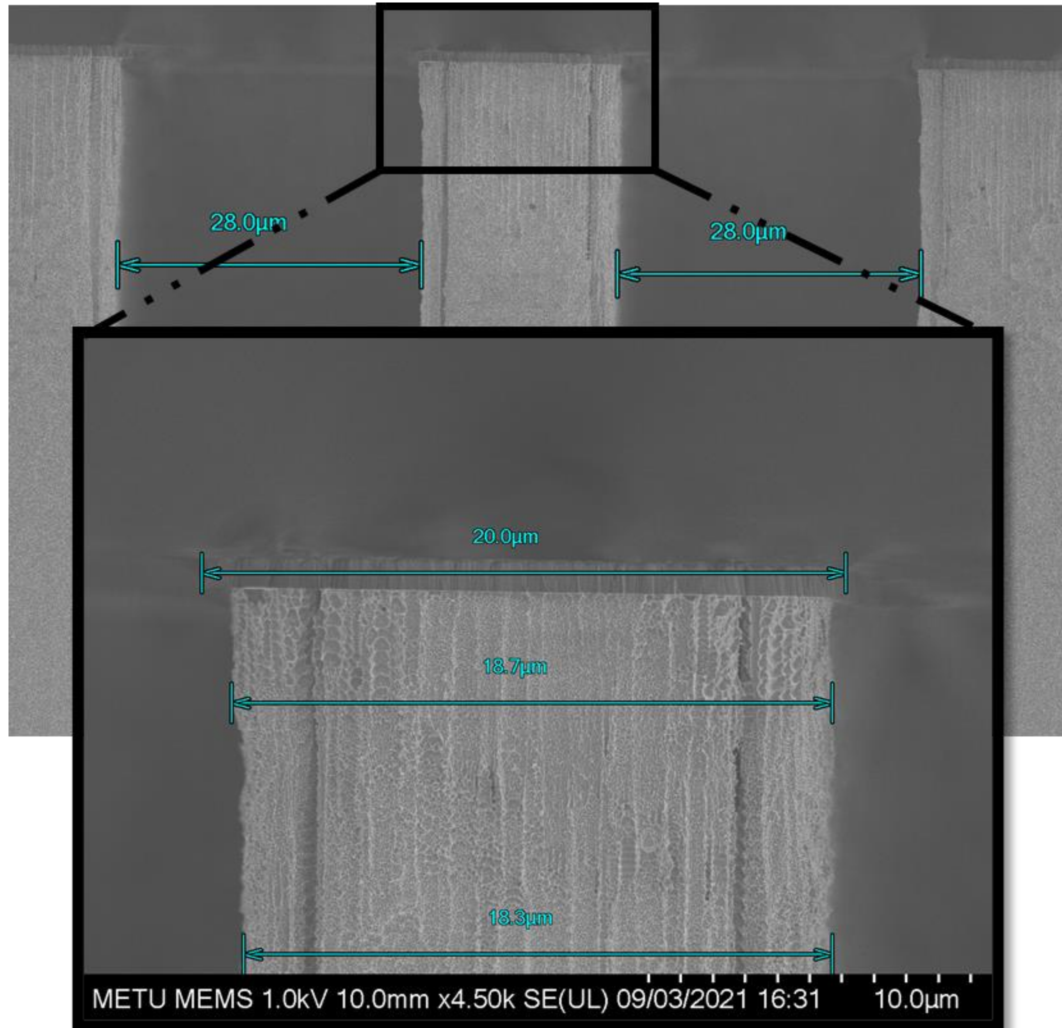

Figure 3.17. An SEM image from the drive fingers.

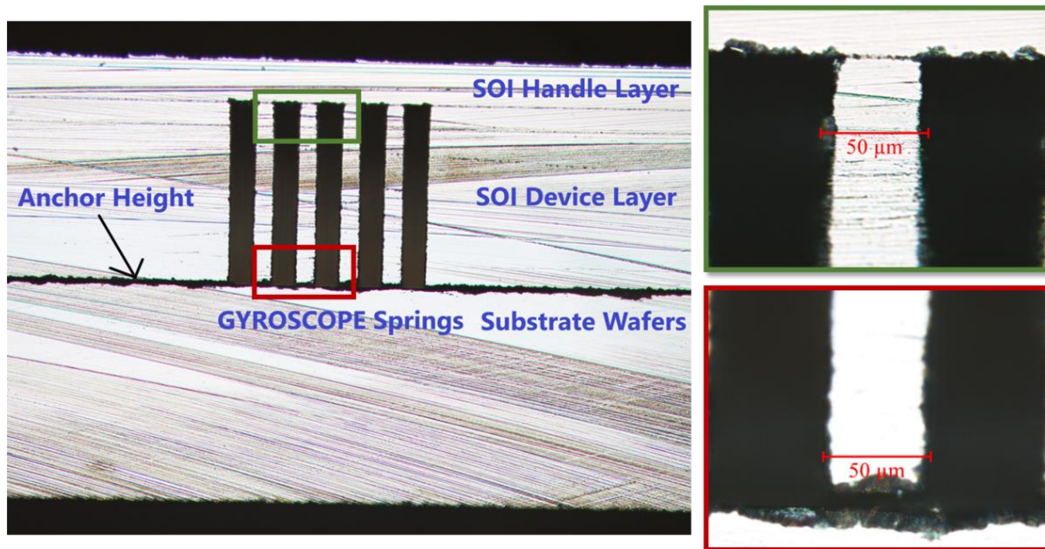

Figure 3.18. A cross-section view of a bonded stack.

Another problem for the fabricated gyroscope is being large in terms of footprint. To have higher proof mass, the structure is designed to be bigger than the commercial gyroscopes. However, that is another source of the problem. The crack propagation is usual for such large devices especially in the high-temperature change steps which are eutectic bonding and handle layer removal steps. That leads to decrease in the yield which is, in turn, failed gyroscopes. Therefore, an optimization in the bonding step is realized because it has a great impact on the distribution of temperature and stress. Au/Si eutectic bonding is selected for having low process temperature, low resultant stress, high strength of bonding, being less sensitive to the particles, and surface roughness [31], [32]. The bonding process is analysed in terms of material composition and thickness, adhesion layer, deposition technique, and pressure. Table 3.1. summarizes trials of bonding with different parameters. The bonding regions of all these trials were investigated by splitting the samples with a razor blade. The sputtering deposition technique is preferred due to being practical and spitting issues in the evaporation. TiW is tried for being a good adhesion layer of the gold. However, TiW act as a great diffusion barrier, also and that leads to discontinuities in the metal connections. The thickness of the materials is decided as 50/300 nm Cr/Au by investigating the overflows in the Au/Si eutectic alloy. The presence of bond

pressure is advantageous because it increases the bond uniformity [33]. However, a decrease of it is unavoidable from 3.5 MPa to 1.7 MPa because of having a relatively thin handle layer. Since the SOI wafer has only 100 microns thickness in the handle layer, high contact forces propagate cracks on the handle layer which leads to failure in the device. Besides from these, it is experienced that surface pre-treatments also play an important role in the bond quality. The native oxide on the surface of the silicon substrates is removed with fresh a BHF (1:5) solution which is in turn high improvements in the bonding process [34].

Table 3.1. Bonding trials with different parameters.

Material	**Thickness (nm)**	**Dep. Technique**	**Temperature (˚C)**	**Duration (min)**	**Pressure**
Cr/Au	30/200	Sputtering	400	20	3.5 MPa
Cr/Au	50/300	Sputtering	400	20	3.5 MPa
Cr/Au	60/400	Sputtering	400	20	3.5 MPa
Cr/Au	30/200	Evaporation	400	20	3.5 MPa
TiW/Au	50/400	Sputtering	400	20	3.5 MPa
Cr/Au	50/400	Sputtering	400	20	3.5 MPa
Cr/Au	50/400	Sputtering	400	20	2.5 MPa
Cr/Au	50/300	Sputtering	400	20	1.7 MPa

In Figure 3.19, quality of the bonding process is shown after the razor blade test. The fracture point of the bonded stack indicates the quality of the process. The fracture point should be silicon itself, not the bond region, to have a better-quality bonding. Moreover, the devices that are processed with the developed bonding recipe are tested in Dage 4000 Bond Tester by applying a shear force to one of the bonded wafers. Figure 3.20 illustrates the quality measurement setup of the bonding process. The result of the selected recipe bonding strength is up to 26.88 MPa which points to a low-quality bonding and needs further optimization.

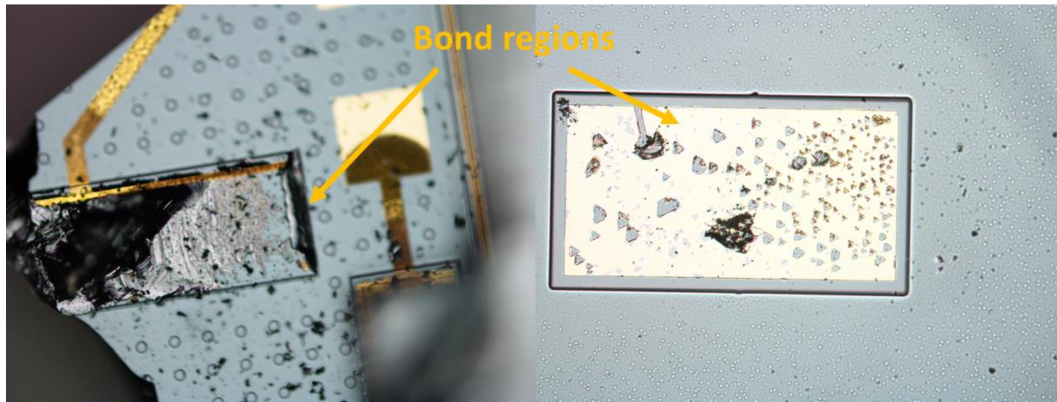

(a) (b)

Figure 3.19. Different fracture points after the razor blade test, (a) indicates a stronger bond and (b) indicates a weaker bond.

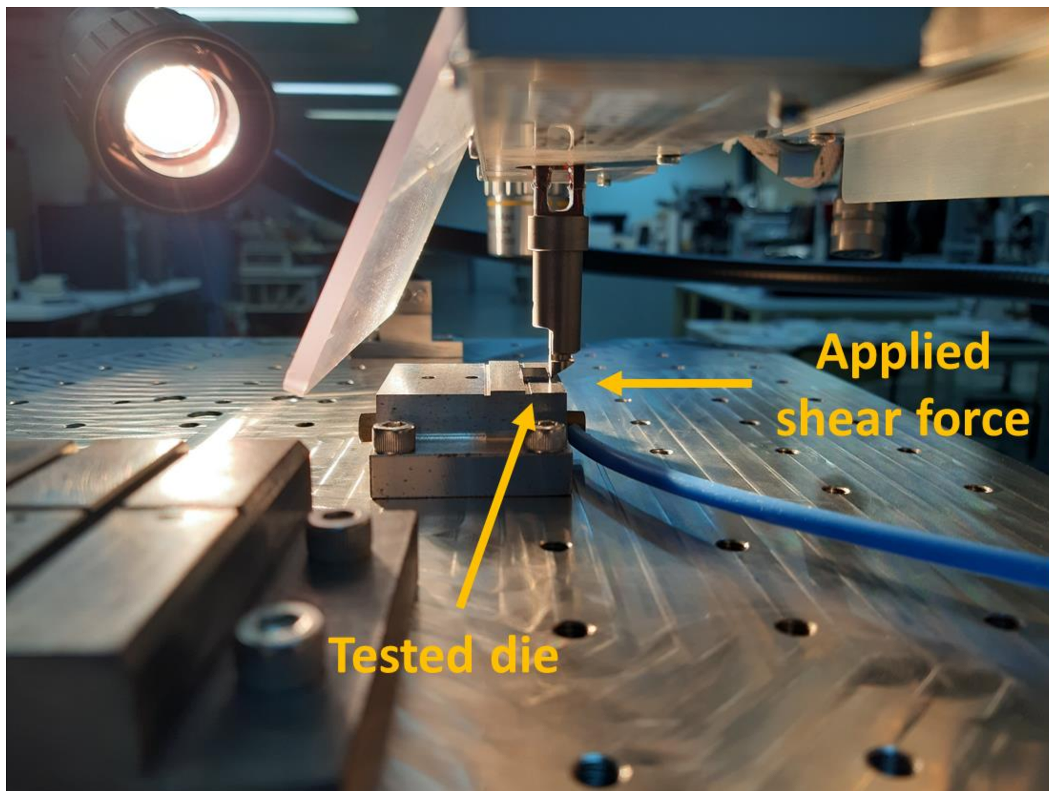

Figure 3.20. Quality measurement setup of the bonding process.

All these problems can be solved with a change in the fabrication process or further optimization of them. A new SOI wafer that has a thicker handle layer and a buried

oxide layer can solve the thinning capacitive fingers and bonding uniformity problems. Moreover, the DRIE recipe can be reoptimized for narrow deep etches to decrease the sidewall breakdowns. The frequencies and widened capacitive gaps can be designed again by considering the undercuts in the DRIE device layer etch. Although all of these solutions are possible, they all need extra time and effort.

3.5 Summary

In this section, the design parameters of the gyroscope and fabrication steps are presented. The use of double-folded springs, the idea behind using them is explained. Electrostatic compensation and tuning electrodes are described. The necessity of the gyroscope to fine-tuning the frequencies is presented. Moreover, FEM simulations of the modal analysis of the gyroscope are shown with the related results. Besides from that, the overall fabrication steps are explained in a detailed way with their problems in it.

CHAPTER 4

CAPACITIVE ENHANCEMENT PROCESSING

In this chapter, the capacitive enhancement process is presented. In Section 4.1 the capacitive enhancement methodology is explained with the designed mechanism. The enhancement method for the drive and sense mode capacitances are discussed and presented with the schematics. Finally, Section 4.2 summarizes the capacitive enhancement processing.

4.1 Capacitive Enhancement Methodology

As it can be understood from CHAPTER 1, in-process methods consist of additional fabrication steps or some advanced fabrication methods. That may lead to further complexity in the process flow or compatibility problems for the fabrication processes. On the contrary, optimization of DRIE processes can be more convenient. However, this time the reachable aspect ratio is much more limited. Besides from these, post-process methods require additional functional elements which are an actuator and a fix mechanism. These elements may cause an increase in the chip footprint. Moreover, fixed electrodes need to be movable temporarily to enhance them later. This time the structure will suffer from stability and insertion loss problems. Furthermore, although electrostatically pull-in structures seem functional and practical, there will be floating potentials that may lead the approach to be used in limited fields. That problem can be solved with a fix mechanism, most probably micro-welding, but, this time the need for high voltages in the device again constrains the available fields. Hence, a novel method is tried to realize a capacitive enhancement process which can be applied in broad regions. Different from MEMS actuators, an external actuator which is joined with a lever mechanism is used for the capacitive enhancement procedure. Figure 4.1 illustrates the capacitive enhancement

methodology. While a holder gripping the device with vacuum, movable electrodes are pushed via suspended capacitive enhancement pins.

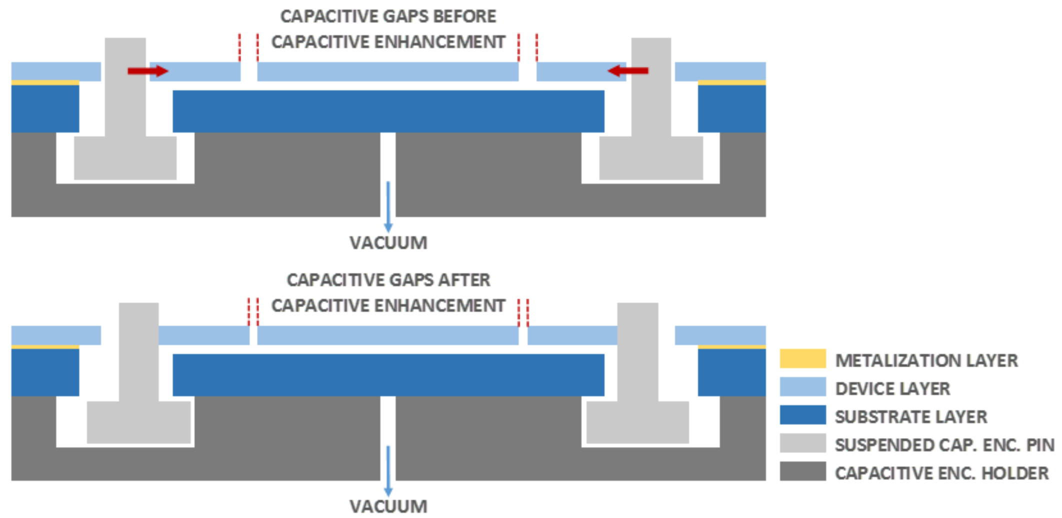

Figure 4.1. Capacitive Enhancement Methodology.

In Figure 4.2, external actuators which are used in the mechanism can be seen. Physik Instrumente N-565 linear stages are selected in terms of design requirements. Their 3 nanometers minimum incremental motion and 0.5-nanometer encoder resolution provide the system highest precision. Moreover, it can travel up to 26 millimeters (±13 mm in both directions) and supply a maximum of 10 Newton force [35].

Figure 4.2. Physik Instrumente N-565 Linear Stage [36].

The connection between the piezo actuators and movable electrodes is realized with a lever mechanism. Figure 4.3 shows the designed lever mechanism. Similar to the gyroscope design, the mechanism has double-folded springs which limits the direction of motion. As stated in CHAPTER 3, flexures behave like a roller due to their different stiffness in different axes. Three pivot points which are formed by weakening the material, are designed to be bendable for the mechanism. While anchor and two carts are fixed in the middle, the remaining parts are suspended. The length of the lever beam and position of the pivot connections to it provides the system additional resolution which is nearly 1:18. Although that feature decreases the total generatable force, the resolution of the system increases to the order of Angstroms.

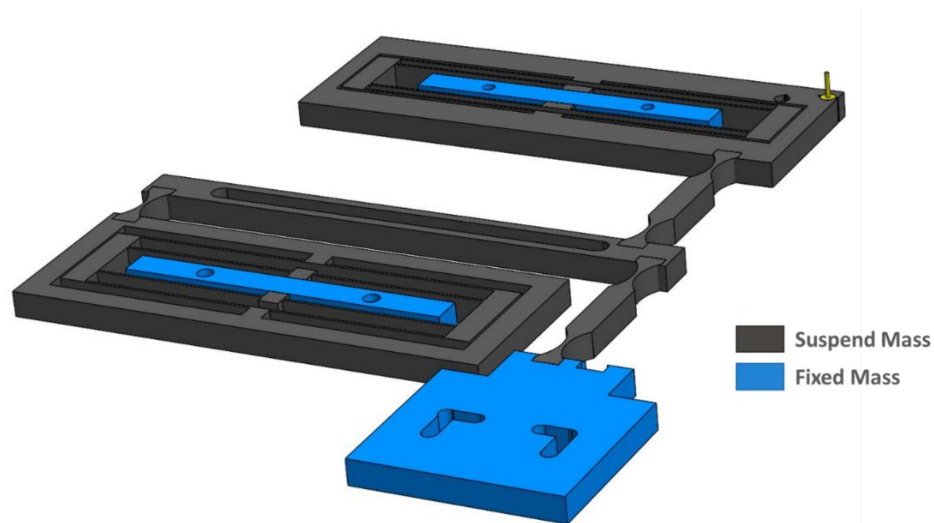

Figure 4.3. Designed lever mechanism.

The motion of linear stages is transferred to the one cart by contact. The other cart transmits the reduced displacement with a 0.8-millimeter diameter pin which is in contact with the movable electrodes. As it can be seen in Figure 4.4, all movable electrodes have two contact points. Two independent lever mechanism is connected on the same electrode and manipulated from different points. That feature not only provides a stable engagement but also allows to rotate the fingers so that their position can be adjusted in 2-DOF. That two-point assembly is mirrored to the other

side of the device so that two enhancement processes can be done at the same time while positioning them with respect to each other. The overall designed system can be seen in Figure 4.5.

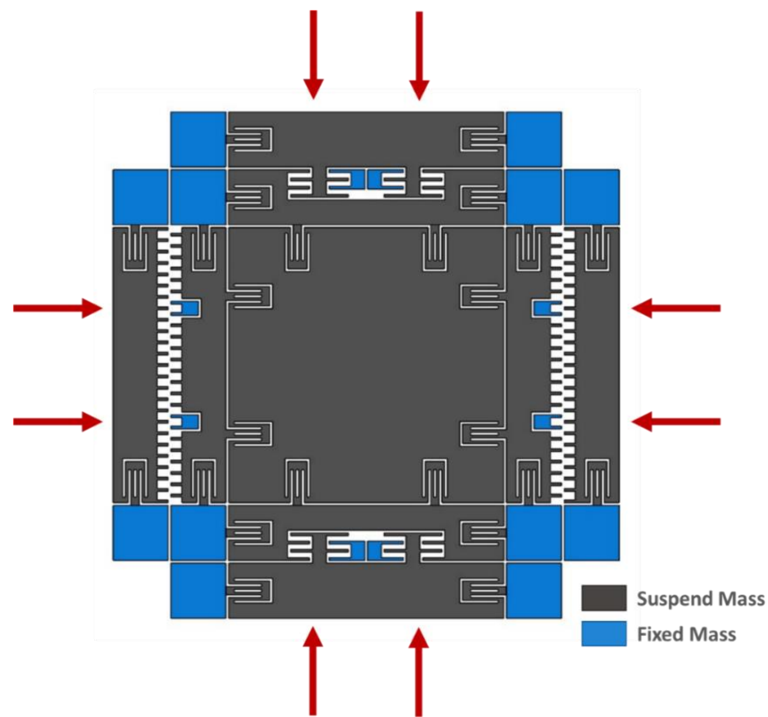

Figure 4.4. A simplified version of the designed gyroscope showing the contact points.

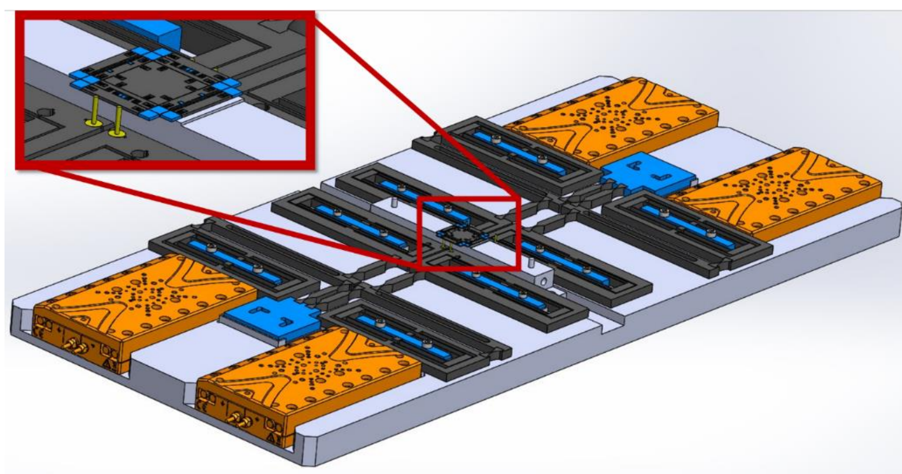

Figure 4.5. The overall assembly design of capacitive enhancement mechanism.

The lever mechanism is manufactured by wire electrical discharge machining (EDM). 5 millimeters thick aluminium 7075 plates are used for that. Figure 4.6 illustrates the overall manufactured system with the assembled piezo motors.

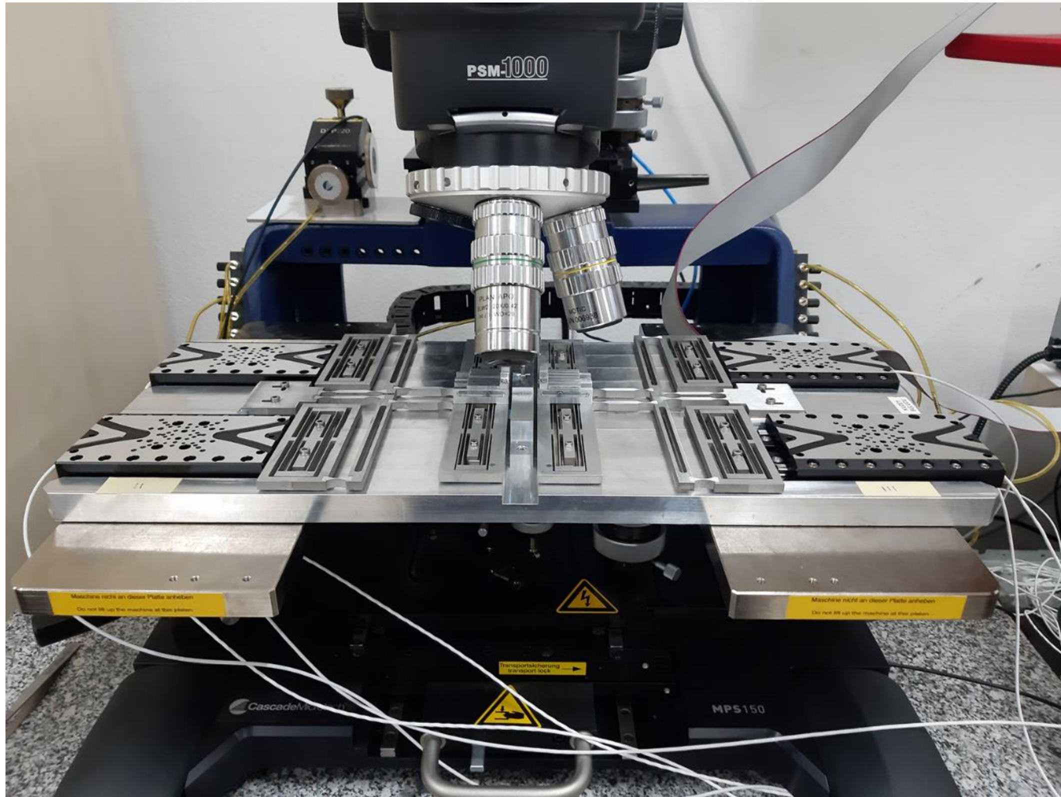

Figure 4.6. Overall manufactured system.

The capacitive enhancement process also includes the fix mechanism. Thermally conductive and electrically isolative epoxy is used to anchor the movable electrodes after the positioning. Loctite Staycast 2850ft black epoxy with CAT24LV is selected for that purpose [37]. The properties of low viscosity and fast cure time in the room temperature play a major role right after the conductivity parameters.

4.1.1 Sense Mode Capacitive Enhancement

The capacitance change is inversely proportional to the square of the capacitive trenches for the varying gap-type fingers. Therefore, the performance of the sensor is dependent quadratically on that trench. Similarly, the electrostatic spring effect is

inversely proportional to the capacitive trenches, but this time with a degree of three. Therefore, the frequency tuning capability range can be arranged by increasing or decreasing the capacitive gaps.

Capacitive gaps are designed to be 25 microns so that long varying gap electrodes with 400 microns deep etches can be ensured. Otherwise, the etch can be stopped before reaching buried oxide due to the aspect ratio limit. That capacitive gaps are designed to be pushed 23 microns so that the working capacitive gaps can be 2 microns.

Positioning adjustment of the electrodes is carried out by capacitance measurement as can be seen in Figure 4.7. For that purpose, two fixed adjustment electrodes are located on each movable electrode. A signal generator supplies to that fixed adjustment electrodes a 40 kHz sine wave which is far away from the primary natural frequencies of the structure. After pushing the movable electrodes, the capacitance value of movable mass is observed. At that moment, epoxy can be applied for fixing the movable electrodes. While epoxy is curing, a fine adjustment can be performed by equalizing the right and left capacitances. Reading two different points of capacitance allows to correct the rotation of engagement. Therefore, whether the engagement procedure is straight can be assured.

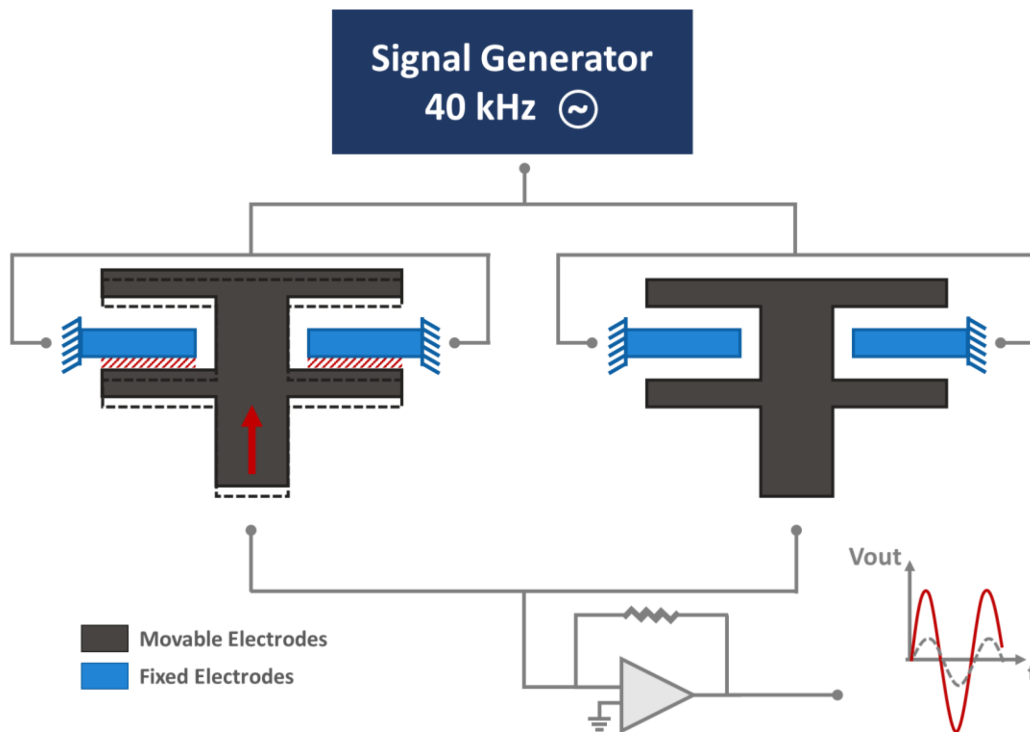

Figure 4.7. Capacitive enhancement positioning adjustment for sense mode.

It is also possible to correct opposite movable electrodes that are attached to the same proof mass. In that way, capacitive imbalances which are originated from the non-uniform trench gaps can be improved. DRIE leads to the issue of capacitive imbalance because trench widths of the structure cannot be etched uniformly. That problem is amplified in thicker devices. Fabricated capacitive gaps become wider than the designed values. As a result, the electrostatic spring effect operates stronger in one direction. That leads to pulling the proof mass stronger in that direction constantly and creating asymmetrical results. Therewith, adjusting the opposite movable electrodes enables to improve capacitive imbalance which has an unavoidable impact on the performance of the gyroscopes. Besides, the Angstrom level adjustment resolution is far better than the traditional lithography and etch resolutions. Micromachining tolerances are quite poor especially for the deep trench etches. Achieving better than %10 tolerances are quite difficult [25]. That leads to poor performances due to wider capacitive gaps and resonance shifts owing to

different spring beam widths. The capacitive enhancement method can also compensate these errors up to some level.

4.1.2 Drive Mode Capacitive Enhancement

The enhancement of the drive mode provides the system to generate superior forces as the capacitive gaps are decreased. Therefore, the system can reach the designed vibration amplitudes with much lower drive signals. Coriolis signal is a weak signal which is generally lower than the drive signals so lowering the drive signals decreases the feed-through capacitances which in turn provides better noise performances [38]. Besides from that, the number of fingers that can be fitted in the designed structure can be increased due to the finger gaps can be much narrower. That feature allows locating nearly 1.35 times greater number of fingers in the current design.

The capacitive gaps after the enhancement process are designed to be 2 microns. On the other hand, the maximum achievable aspect ratio is nearly 1:40 for the MEMS CENTER Facilities. That ratio is much lower in the deep etches which is 400-micron depth in this thesis because of that reason the minimum etchable capacitive trenches are designed to be 12 microns which is 6 times wider than the enhanced gaps. Therefore, the total force can be increased up to 8 times.

Position adjustment of the drive fingers are similar to the sense mode enhancement. However, this time the displacement of the movable fingers is greater which is nearly 60 microns. Figure 4.8 illustrates the capacitive enhancement positioning adjustment for drive mode.

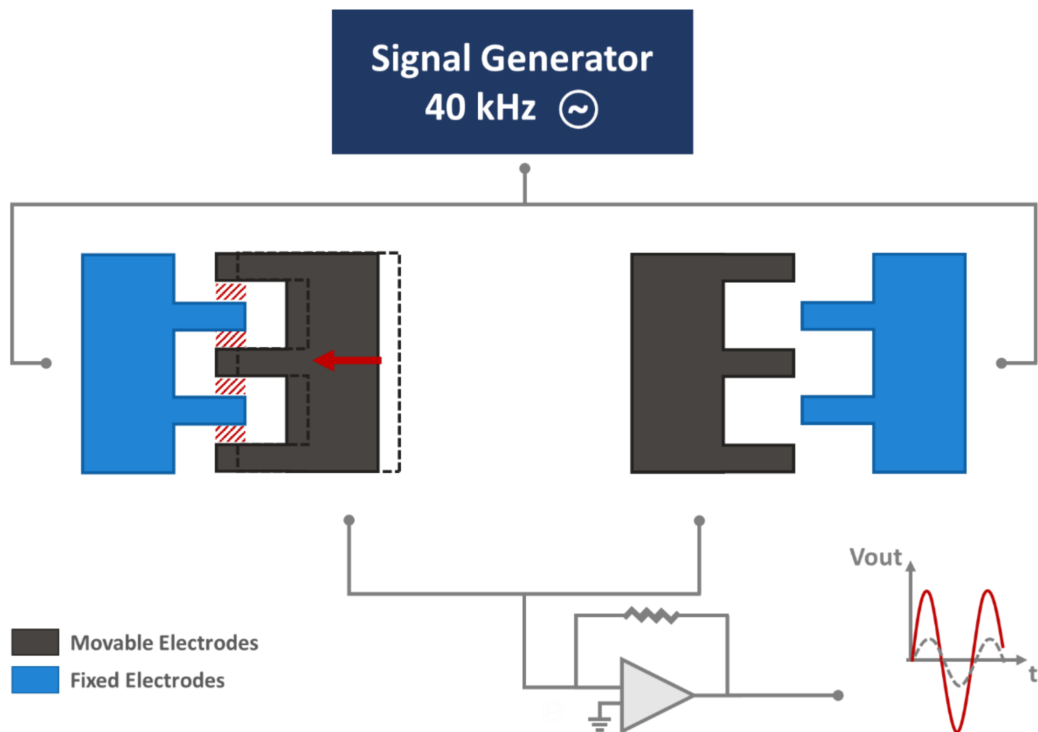

Figure 4.8. Capacitive enhancement positioning adjustment for drive mode.

4.2 Summary

In this chapter, it is presented the methodology of capacitive enhancement process. The designed lever mechanism that will help to enhance the capacitance is shown. Besides from that, the enhancement process in the drive and sense mass is presented. It is shown that, while the generated force in the drive mode can be increased up to 8 times, in the sense mode the capacitance values can be increased 15 times. Moreover, the difference between electrodes due to poor tolerances can be suppressed up to some level.

CHAPTER 5

TEST RESULTS

In this chapter, test setup preparations and performed test and improvement results are presented. In Section 5.1, the preparation of the device after the fabrication step is shown. The test setup of the characterizations of the device is explained and the result of frequency responses of the devices are plotted. In Section 5.2, capacitive enhancement application of the devices is demonstrated with the constructed setup. The improvements of the results after the capacitive enhancement process are investigated. Lastly, in Section 5.3, frequency response tests after capacitive enhancement process is presented.

5.1 Read-out Electronics and Characterization Test Setup

The fabricated devices are attached on a PCB with a Loctite EA 1C white epoxy on a 110 °C hot plate. That PCB has pins for each metal connection and also through holes on it to enable capacitive manipulation. The surface finish of the PCBs is electroless nickel immersion gold (ENIG) so that the wire bonding process can be realized with Delvotec 5610 Ball Bonder. Figure 5.1 illustrates the fabricated device and PCB connected to each other with the wire bonder.

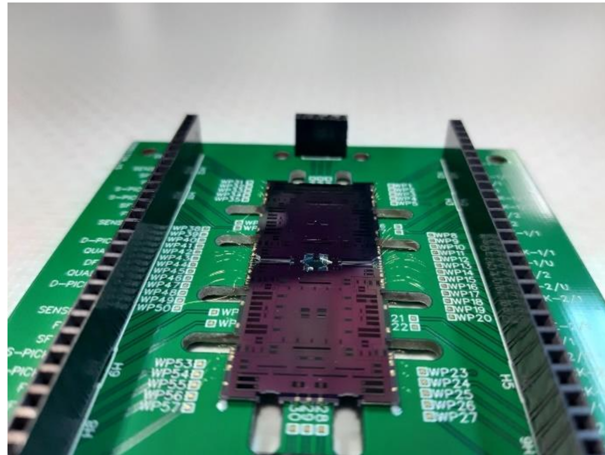

Figure 5.1. Fabricated device connected to the device PCB.

The most effective method for the system characterization of the resonant devices is realizing a frequency response test [39]. Therefore, another PCB that can be attached directly to the device PCB is designed for the frequency response tests. Figure 5.2 shows the designed PCB with integrated LF353 opamps, 1MΩ resistors, and 150 nF capacitors. These electronic circuit elements form trans-z circuits on the PCB and are directly connected to the related drive and sense electrodes.

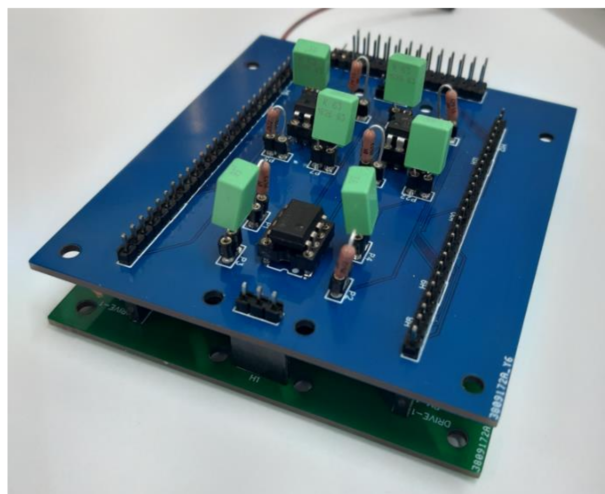

Figure 5.2. Characterization PCB and related electronic circuit units on it.

Figure 5.3 clarifies the constructed test setup for the resonance characterization with a schematic. Keysight E5061B network analyzer connected to the drive and drive pick electrode after the trans-impedance amplifier. At the same time, the Agilent

E3631A power supply supplies the proof mass voltage. The device is excited with a selected frequency range as a result, capacitance is changed due to the response of the system. That change is amplified and converted into voltage output by trans-impedance amplifiers [39]. That setup is also applicable for the sense mass which can be exited via parallel plates. The drive and pick of the drive can be carried out by the two oppositely oriented sense mass.

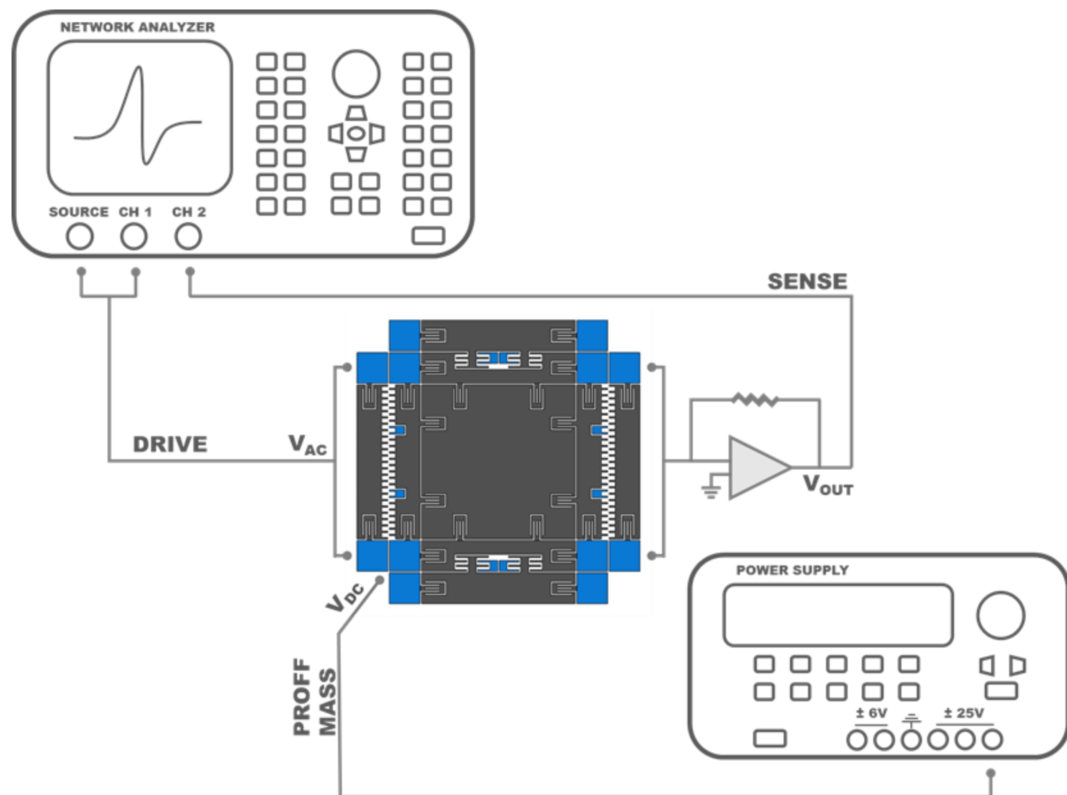

Figure 5.3. Schematic view of a characterization setup.

The constructed characterization setup can be seen in Figure 5.4. The device PCB which is connected to the characterization PCB placed in a vacuum chamber so that the response of the system can be visualized better. Two power supplies that are connected in series run the opamps on the characterization PCB and supply the proof mass voltage which is in the range of 0-100V. The network analyzer draws the phase and magnitude graphs by using the drive and drive pick signals.

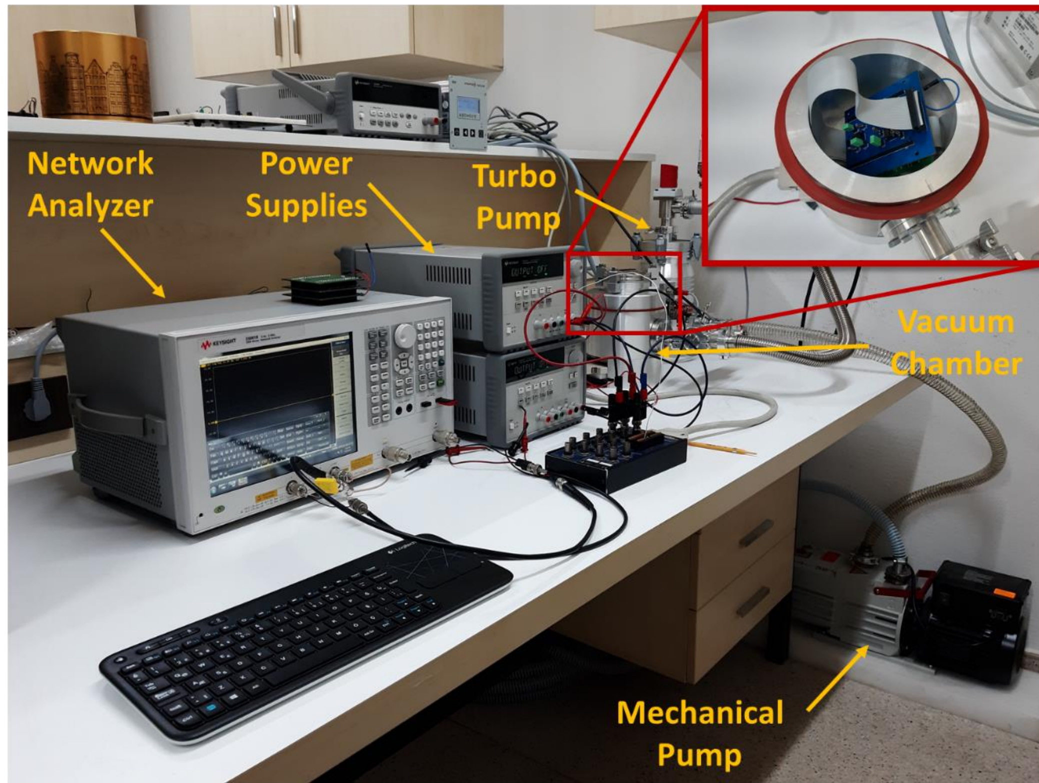

Figure 5.4. Characterization setup.

The frequency response tests are realized in the range of 0.075 mTorr with 40 Volts proof mass voltage. The drive resonance frequencies of the fabricated devices deviate between 5578-6265 Hz. Figure 5.5 illustrates the drive mode frequency response of device-2 gyroscope-2. The resonance frequency of the related mass is 5930.625 Hz. As indicated in Figure 3.5, the designed drive mode frequency is 7756.8 Hz. The difference between designed and fabricated frequencies is nearly 2 kHz. That is mostly due to the thinning of the spring beams while performing DRIE etches. The undercut is nearly 6-8 microns thinned the beams which lead to such a dramatic decrease in the resonance frequencies.

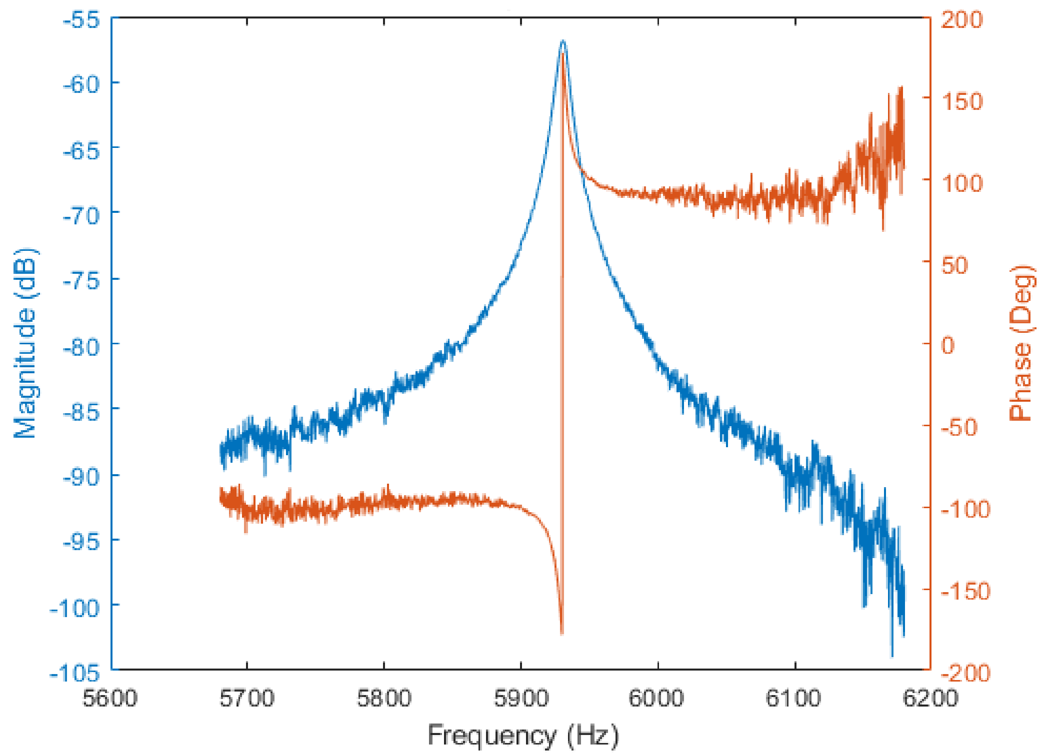

Figure 5.5. Drive mode frequency response of Device-2 Gyroscope-2.

Besides from that, the quality factors of the tested devices are between 700-800 which is quite lower than expected. The main reasons behind this issue are low-quality eutectic bonding, lack of coupling with the other mass, temporary bonding of the device to the device PCB. It should be noted that, the designed double mass gyroscope suffers from lack of coupling mechanism due to a mistake in the lithography mask. Therefore, the eutectic bonding step should be optimized, a new mask with the updates should be designed and a strong bond to the package should be performed to achieve higher values of quality factor.

5.2 Capacitive Enhancement Application

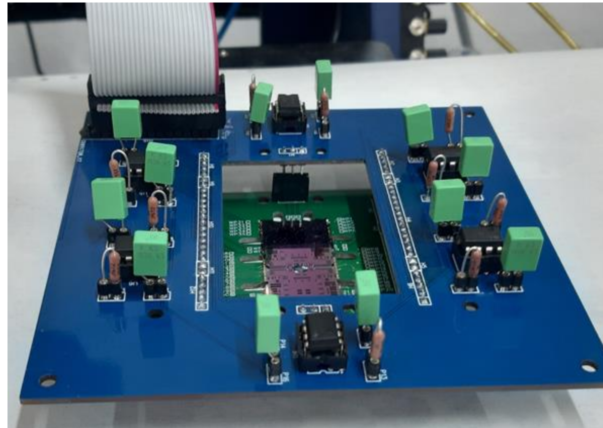

Figure 5.6. Designed capacitive enhancement PCB with the related electronic component attached.

The capacitive enhancement process is realized right after the primary characterization results. This time a dedicated capacitive enhancement PCB is connected to the device PCB. Figure 5.6 shows the capacitive enhancement PCB with the related electronic components attached. Notice that, there are six trans-impedance amplifiers for each enhancement process for a double mass gyroscope. The middle of the PCB is cut out for the visualization of the enhancement process under the microscope. Figure 5.9 shows the overall capacitive enhancement setup. The capacitive enhancement mechanism is placed on a microscope table to visualize the enhancement process. DC power supply runs the trans-z circuits on the capacitive enhancement PCB which is directly connected to the related movable masses and picks. Keysight 3300B Series waveform generator applies the same AC signal to the right and left picks and the capacitance is read from the movable masses. The capacitance value is generated on the Hewlett Packard 35665A dynamic signal analyzer screen with a power spectrum. It can also be observed from the Pintek PS-200 oscilloscope. Piezo motors are controlled by a computer with the help of their controllers. The position of the enhancement pins increased step by step with the piezo motors and capacitance is increased as a result of this. That capacitance increase can be monitored with the DSA.

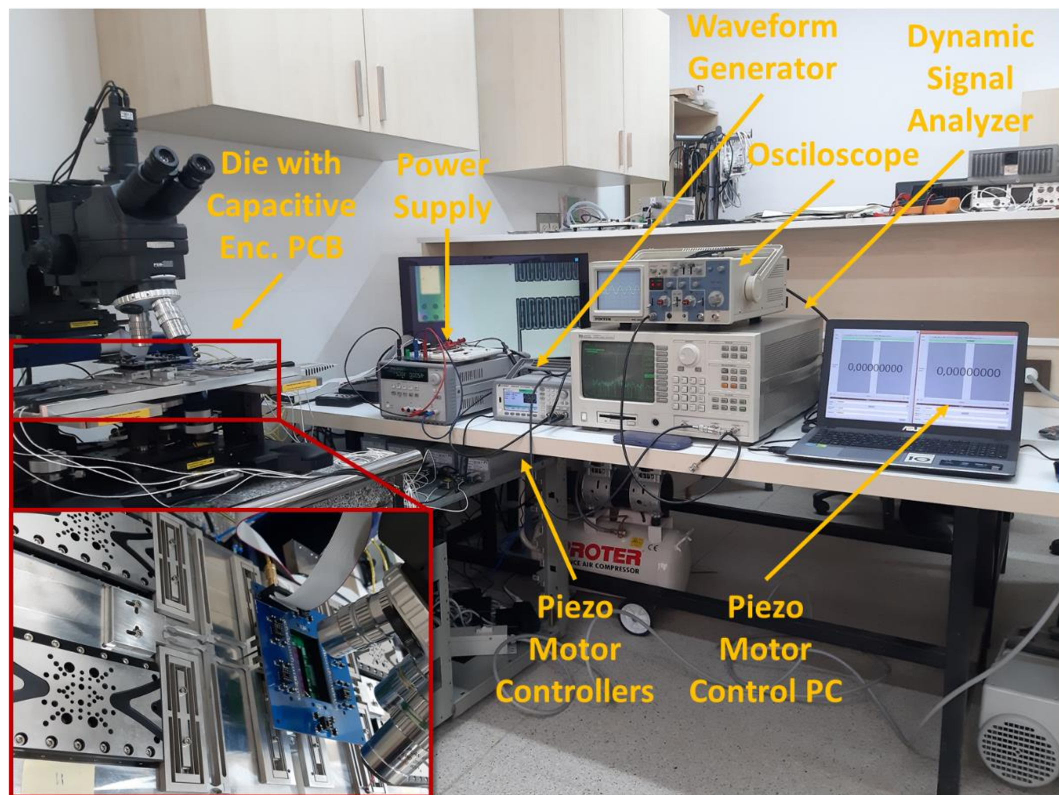

Figure 5.7. Overall capacitive enhancement setup.

The capacitive enhancement process is realized with the help of the constructed setup. Figure 5.8 shows that the capacitive gap decreases in the sense mass. The movable mass is pushed with piezo motors and increases in the capacitance are recorded. Later, epoxy is applied on top of the movable mass springs. Loctite EA 1C white epoxy is applied to the device because of having a faster cure time rather than Loctite Staycast 2850ft black epoxy. Then, a fine adjustment with minor displacements is realized to balance right and left sense picks.

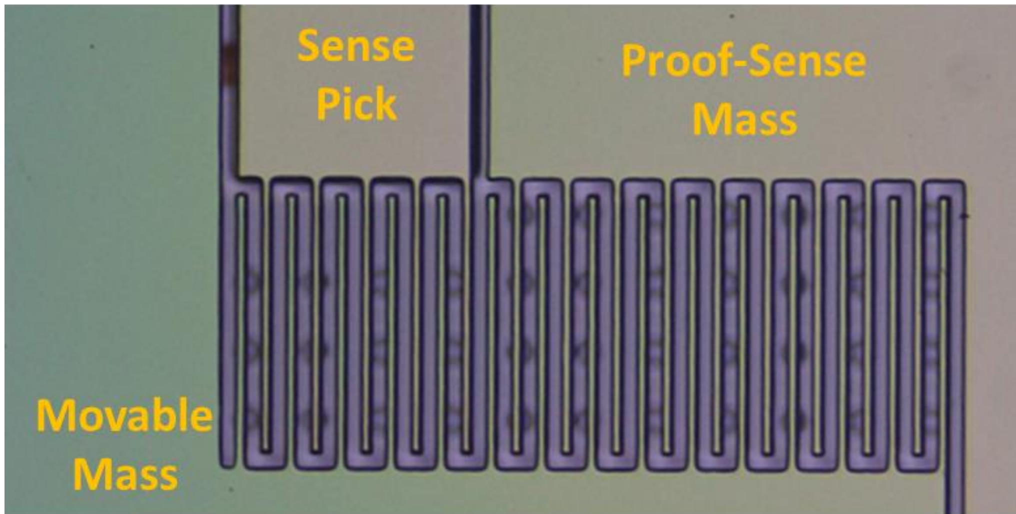

(a)

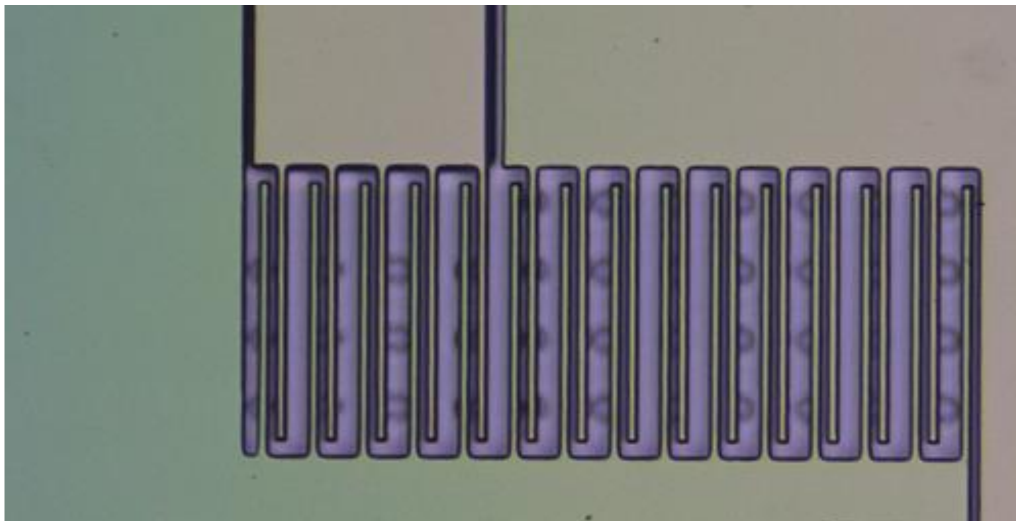

(b)

Figure 5.8. Capacitive enhancement of the sense fingers. (a) before capacitive enhancement, (b) after capacitive enhancement.

Figure 5.9 illustrates the increase in the capacitance of a sense mass. The capacitance between the sense picks and movable mass is increased from -11.0581 dBVrms to -3.6381 dBVrms which results in nearly 11.5 times increased capacitance with approximately 1.4 microns engaged capacitive gap.

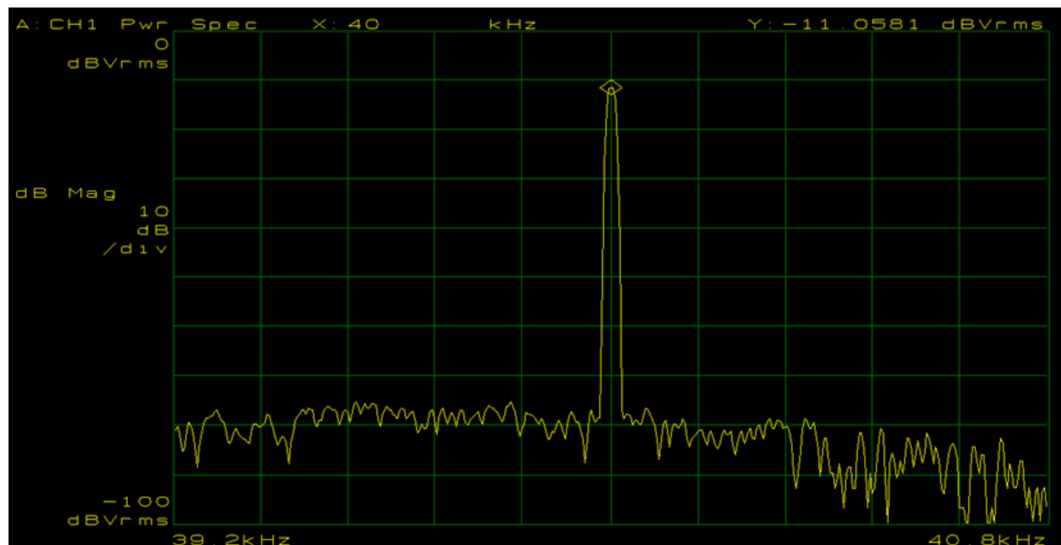

(a)

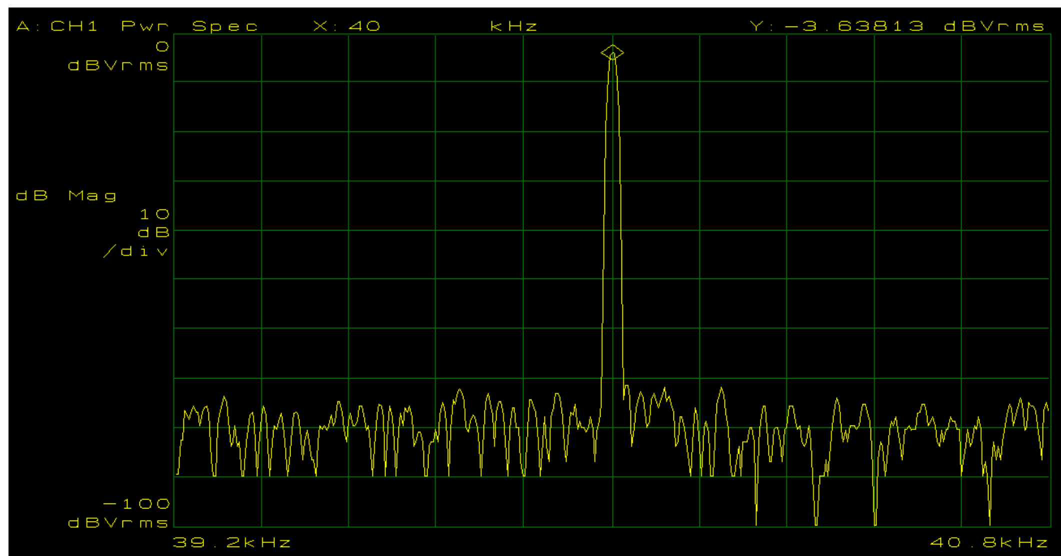

(b)

Figure 5.9. Capacitance increase visualization of the sense mass. (a) Before the enhancement process, (b) after the enhancement process.

Despite the increase in the capacitance, the enhancement process also generates an unbalanced capacitance between the fingers. Therefore, a balance step is also realized right after the enhancement of the capacitance. For that purpose, the waveform generator supplies inverted AC signals to the related picks and the current that is generated due to capacitance kills each other. If one of the picks has a higher capacitance, the voltage that is generated by the capacitance will increase and point

out the capacitive unbalance between the electrodes. Figure 5.10 shows the elimination of unbalanced capacitance. As it can be seen, the capacitance difference is decreased from -26.2914 dBVrms to -35.2678 dBVrms which is very close to the initial balance of the electrodes before the enhancement process. The overall power spectrum results of the capacitive enhancement process can be seen in Table 5.1.

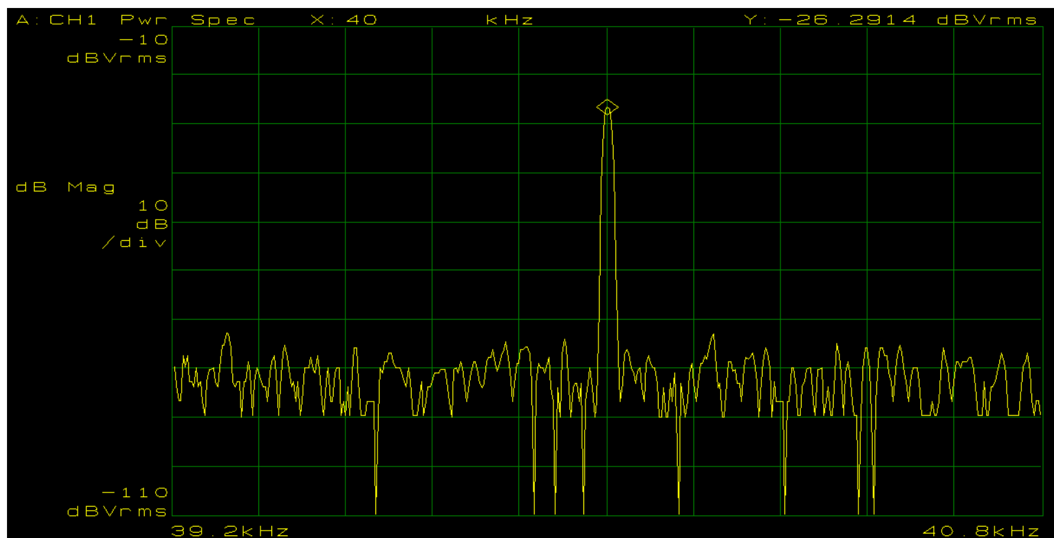

(a)

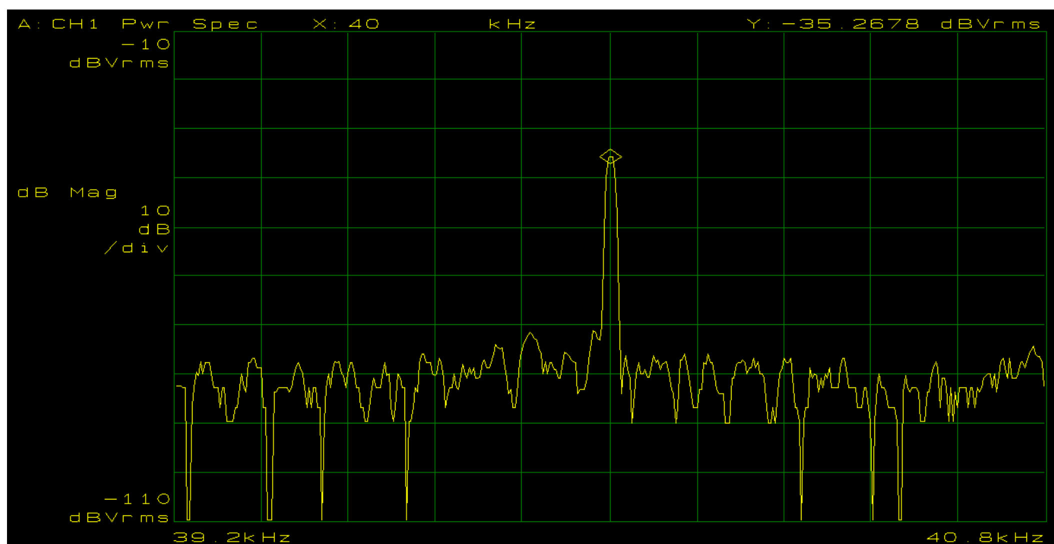

(b)

Figure 5.10. Balance of capacitive enhancement. (a) After the enhancement process unbalanced capacitance, (b) after balancing operation.

Table 5.1. Capacitive enhancement results of the sense mass 2/1 with 40 kHz, 0.1 V_{pp} AC signal.

Process Steps	Power Spectrum (dBVrms) Applied AC Signal	
	Identical	Inverted
Before Cap. Enc. Process	-11,05	-36,78
Capacitive Enhancement	-4,21	-26,29
Capacitive Balance	-3,63	-35,26

The drive mode capacitive enhancement is similar to the sense mode. However, this time the displacement is nearly 50 microns. The enhancement of the drive mode can be seen in Figure 5.11. Initially not engaged drive fingers are pushed and engaged their working position.

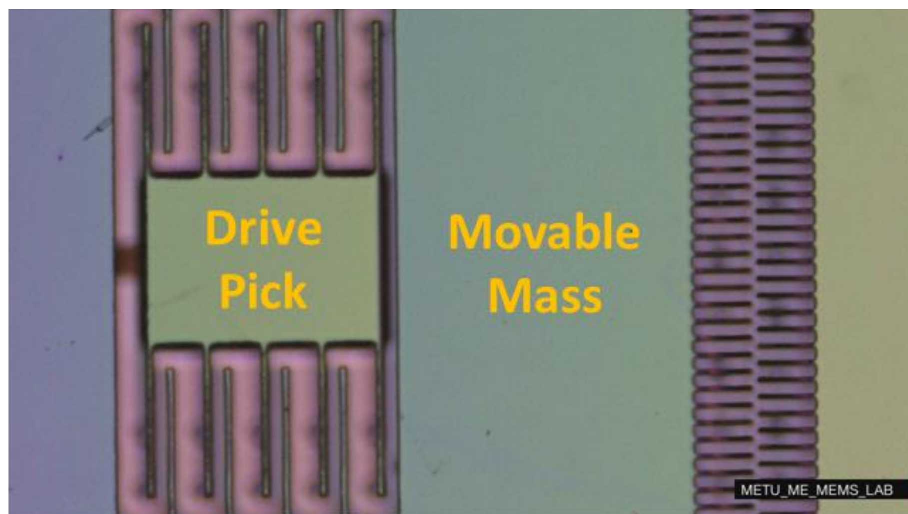

(a)

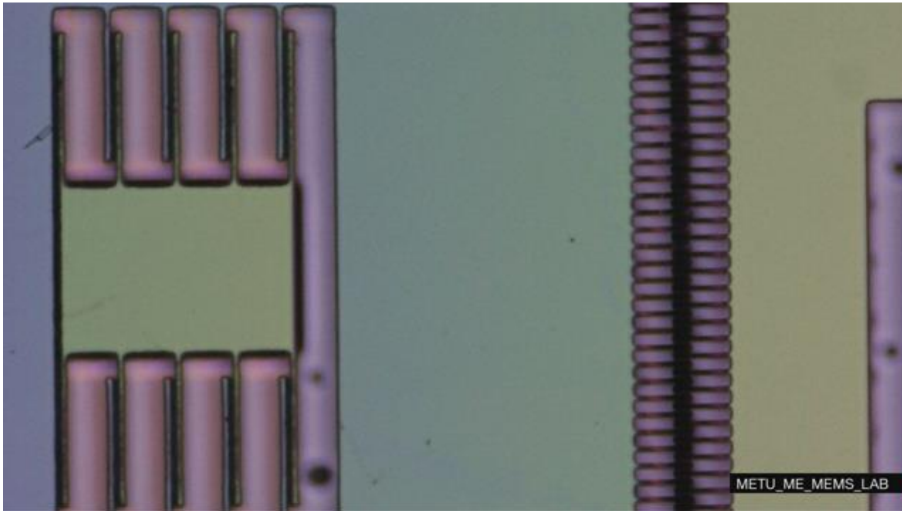

(b)

Figure 5.11. Capacitive enhancement of the drive fingers. (a) before capacitive enhancement, (b) after capacitive enhancement.

Although it is expected to have 2 microns capacitive gap after the engagement process, excessive undercut leads to increase in the capacitive gap which limits the capacitance between the drive fingers. Figure 5.12 illustrates the difference of designed and fabricated drive mode comb fingers. Therefore, the capacitance increase monitored barely, due to wider capacitive gaps and higher parasitic capacitances in the structure.

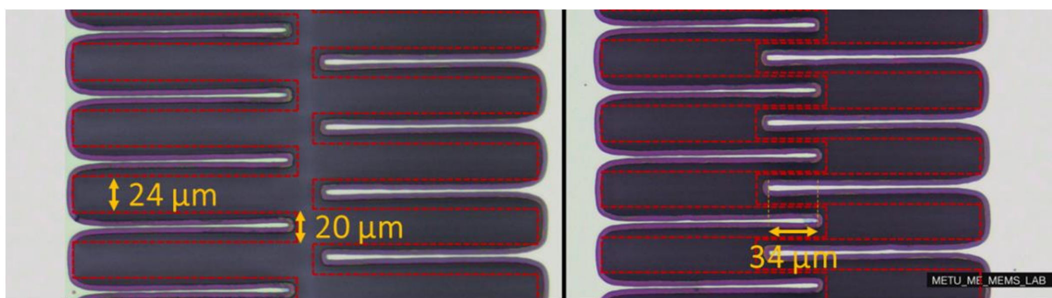

Figure 5.12. The difference of designed and fabricated drive mode comb fingers.

5.3 Characterization After Capacitive Enhancement

The characterization tests are realized after the capacitive enhancement process. These tests also ensure the suspended masses are still working after the enhancement

because application of the epoxy may lead undesired stictions. Figure 5.13 shows that the drive mode frequency response test results under 40 V proof mass and 0.225 mTorr. The results show that output signal increase nearly 16.5dB. However, comparing these results in the drive mode may not be proper because the before enhancement process fingers are not engaged and the actuation mechanism behaves completely different.

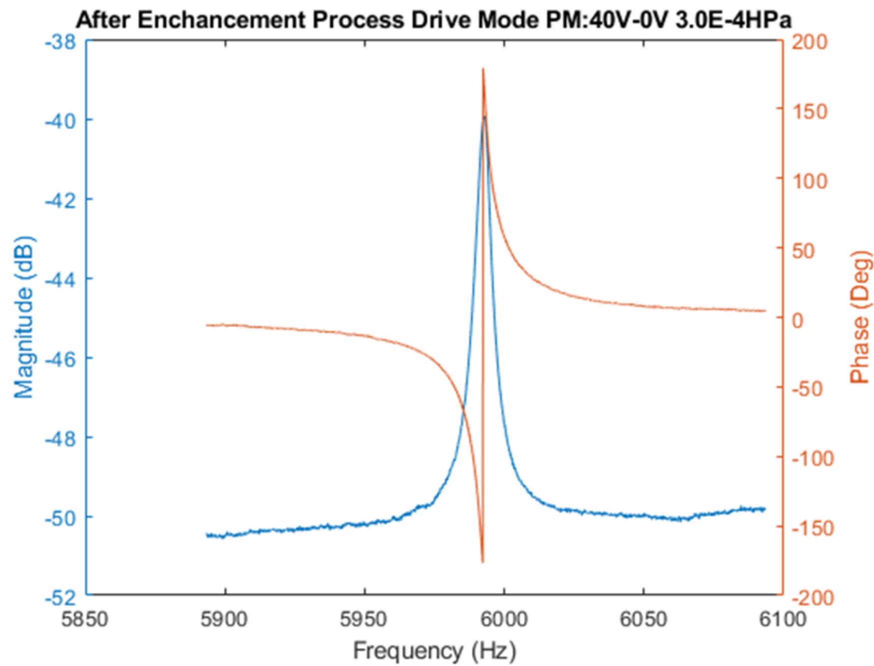

Figure 5.13. Drive mode frequency response test results after capacitive enhancement process under 40 V proof mass and 0.225 mTorr.

Figure 5.14 shows that the frequency response test results of the sense mode after capacitive enhancement process under 25 V proof mass and 0.345 mTorr. Since the capacitive gap is really wide before capacitive enhancement process, the frequency response test cannot be applied because of the weak signals. Therefore, there are not any available comparison in terms of frequency response test.

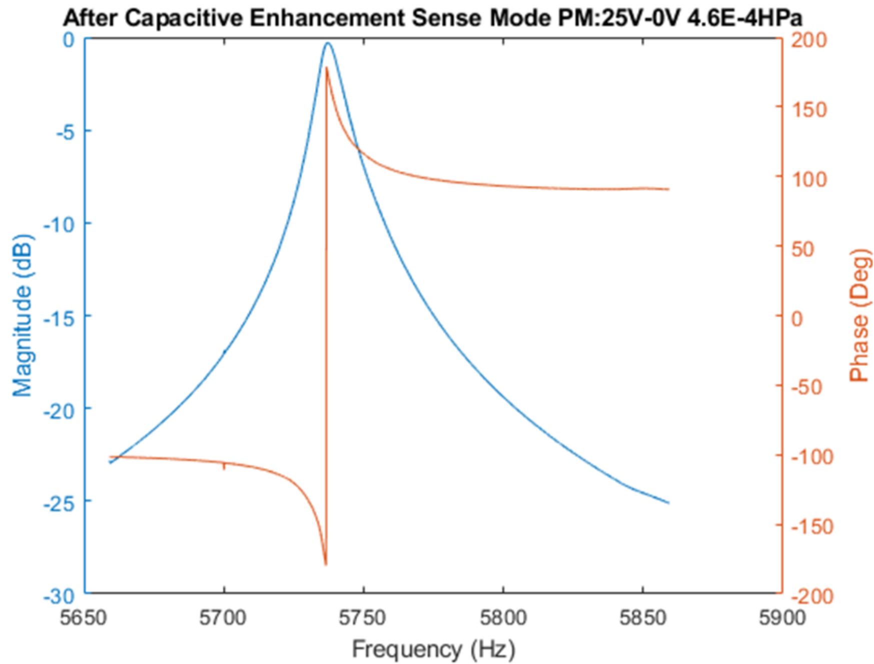

Figure 5.14. Sense mode frequency response test results after capacitive enhancement process under 25 V proof mass and 0.345 mTorr.

In conclusion, test setup preparations, performed tests and improvement results are presented in this chapter. It is achieved that the capacitance increase in the sense mode is approximately 11.5 times than the initial capacitance. Moreover, after the enhancement process the fingers are balanced by checking right and left sense picks. Besides from these, the capacitive enhancement is realized in the drive electrodes, also. However, excessive undercut in the fingers limits the maximum achievable capacitance in that mass. That undercut is tolerated in the sense fingers by increasing the displacement of the sense movable mass. It can be overcome with further optimization for the drive mass. First of all, excessive undercut can be solved with increasing the buried oxide in the SOI wafer as stated in CHAPTER 3 fabrication steps. The current buried oxide cannot endure the power of 400 microns etching as a result of this, the whole body is exposed to the etch gas during the handle layer removal step. That creates a huge problem in the spring beams and the finger widths. Secondly, the fingers of the drive can be designed with zero or even negative gap by analysing the nominal undercut [3]. Therefore, the capacitive gap can be arranged

even if lower than the 2 microns. To sum up, Table 5.2 summarize the achieved parameters of the gyroscope. Moreover, it also compares these values with specific works in the literature. Ref. [40] shows the fabricated parameters of a double mass gyroscope which is similar to this work. On the other hand, in the third column, there is a capacitive enhanced work (Ref. [6]) which has nearly the same capacitance value in the sense electrodes while having 5 times smaller footprint rather than the Ref. [40]. The forth column averages standard parameters of a double mass gyroscope from Ref. [40] to be able to make a comparison of achieved parameters in this thesis. The fifth column shows the parameters if these standard dimensions are scaled up 10 times. This time while the proof mass increases 1000 times, the capacitance value is limited with the capacitive gaps and increased 10 times. Lastly, the sixth column proves the capacitive enhancement improvements by showing the achieved parameters. As it can be seen (Table 5.2), the achieved gyroscope has far more capacitance and proof mass than literature works by having a larger structure with capacitive enhancement. However, that massive structure also increases the footprint of the device.

Table 5.2. Comparison of achieved parameters.

Parameter	**Ref. [40]**	**Ref. [6] with Cap. Enc.**	**Standard Dims. (Averaged from [40])**	**Scaled Dims. (10X)**	**This Work 10 X with Cap. Enc.**
Device Thickness	30 µm	25 µm	40 µm	400 µm	400 µm
Chip area	~7.5 mm^2	1.5 mm^2	10 mm^2	1000 mm^2	1000 mm^2
Sense Cap.	4.82 pF	4.9 pF	~5 pF	50 pF	~ 240 pF
Sense finger gap	1.1 µm	1 µm	1 µm	12 µm	~1.4 µm
Drive comb gap	1.1 µm	-	1 µm	12 µm	~5.5 µm (ex. thinning)
Weight of PM	0.27 mg	-	0.20 mg	200 mg	~86.5 mg

CHAPTER 6

CONCLUSION AND FUTURE WORKS

This research reported a novel capacitive enhancement process to achieve higher capacitance values by overcoming the aspect ratio limitations. Capacitive enhancement is realized in both drive and sense fingers and their improvements are demonstrated. Firstly, a double mass gyroscope which is coupled with a diamond shape coupling is designed. A mathematical model is generated to decide the parameters of the gyroscope. Then FEM analyses are studied and compared with the mathematical model. The design of the gyroscope is optimized according to that FEM results. The designed gyroscope is fabricated in METU MEMS Center with the available devices. Later, the fabricated devices are attached to the designed PCBs that will enable the post-processing and characterization. Capacitive gaps are reduced to the operating positions by post-processing and the improvements of the gyroscope are examined. Based on the results from this research can be summarized as follows:

1. The dynamics of the gyroscope are investigated. As a result of this, a mathematical model is generated and design parameters are decided. Decreasing the mechanical noise was the objective. This leads to an increase in the proof mass. To increase the proof mass larger footprint, 48 mm x 21 mm, with a 400-micron thick device is designed. The design is supported and optimized with FEM analyses.
2. The necessity of a thicker device limits the capacitive gaps which create the need for capacitive enhancement. The gyroscope design is adapted to post-processing. Therefore, normally fixed electrodes are designed suspended and the substrate wafer is etched thoroughly to enable the manipulation of the electrodes.

3. 400 microns thick device require optimization for the deep structure etches. A new DRIE recipe is generated for that purpose. For achieving such deep structures platen power is increased as a result of this, the selectivity of the etch decreased, and buried oxide could not endure. That creates excessive undercut in the handle layer removal step so that the performance of the gyroscope is affected, negatively. The equivalent undercut is calculated 6-8 microns by comparing the results with the FEM analyses.
4. The capacitive enhancement processing setup is constructed and the post-process is performed. As a result, sense finger capacitive gaps are decreased from 32 microns to 1.4 microns with 11.5 times increase in capacitance. In the drive mass, initially not engaged drive fingers are pushed up to 50 microns which provides higher than 34 microns overlap area. However, the improvement in the drive fingers is really low due to the excessive undercuts. That problem is obviated in the sense fingers by pushing further than designed. Besides from these, those fingers are capacitively balanced after the enhancement in case of skewed displacement in the enhancement process.

Although the capacitive enhancement of the device is performed, the drive mode enhancement needs further research for the improvement of the performance of the gyroscope. Beside from these, to achieve further improvement in the following topics should be performed:

1. The excessive undercut can be solved with a new SOI that has a thicker buried oxide layer. Moreover, the fingers of the drive mass can be designed with zero or even negative gaps by analysing the nominal undercut.
2. The capacitive enhancement process is not easy to apply on all of the masses without trouble because it is highly dependent on the user. The overall enhancement mechanism can be optimized with the minimization of user contact. An alignment mechanism can be attached to the system and the epoxy application can be changed with the fixing mechanisms in the literature.

3. For the improvement of the performance of the gyroscope quality factor should be increased. For that purpose, low-quality eutectic bonding should be optimized, the coupling mechanism between the drive masses should be connected with the new mask and packaging should be performed to achieve higher values of quality factor.
4. The electrostatic compensation and tuning electrodes should be activated to achieve higher sensitivity of the device.
5. DRIE recipe should be optimized further for the minimization of sidewall breakdowns. Scallop removal operations can be further performed for better improvement.

REFERENCES

[1] S. Sonmezoglu, S. E. Alper, and T. Akin, “An automatically mode-matched MEMS gyroscope with wide and tunable bandwidth,” *J. Microelectromechanical Syst.*, vol. 23, no. 2, pp. 284–297, 2014, doi: 10.1109/JMEMS.2014.2299234.

[2] K. J. Owen, B. VanDerElzen, R. L. Peterson, and K. Najafi, “High aspect ratio deep silicon etching,” *Proc. IEEE Int. Conf. Micro Electro Mech. Syst.*, no. February, pp. 251–254, 2012, doi: 10.1109/MEMSYS.2012.6170138.

[3] T. Furuhata, T. Hirano, K. J. Gabriel, and H. Fujita, “Sub-micron gaps without sub-micron etching,” *Proceedings. IEEE Micro Electro Mech. Syst.*, pp. 57–62, 1991.

[4] T. Hirano, T. Furuhata, K. J. Gabriel, and H. Fujita, “Design, Fabrication, and Operation of Submicron Gap Comb-Drive Microactuators,” *J. Microelectromechanical Syst.*, vol. 1, no. 1, 1992.

[5] F. Ayazi and K. Najafi, “High aspect-ratio combined poly and single-crystal silicon (HARPSS) MEMS technology,” *J. Microelectromechanical Syst.*, vol. 9, no. 3, pp. 288–294, 2000, doi: 10.1109/84.870053.

[6] D. Reuter, A. Bertz, D. Billep, D. Scheibner, W. Dötzel, and T. Gessner, “In-process gap reduction of capacitive transducers,” *Sensors Actuators, A Phys.*, vol. 126, no. 1, pp. 211–217, 2006, doi: 10.1016/j.sna.2005.09.033.

[7] S. Pourkamali, G. K. Ho, and F. Ayazi, “Low-impedance VHF and UHF capacitive silicon bulk acoustic-wave resonators -Part I: Concept and Fabrication,” *IEEE Trans. Electron Devices*, vol. 54, no. 8, pp. 2024–2030, 2007, doi: 10.1109/TED.2007.901405.

[8] R. Abdolvand and F. Ayazi, “An advanced reactive ion etching process for very high aspect-ratio sub-micron wide trenches in silicon,” *Sensors*

Actuators, A Phys., vol. 144, no. 1, pp. 109–116, 2008, doi: 10.1016/j.sna.2007.12.026.

[9] E. Pyatishev, Y. Enns, I. Komarevtsev, M. C. Wurz, and A. Glukhovskoy, “A micromechanical gyroscope with bistable suspension of microdrive,” *2017 24th Saint Petersbg. Int. Conf. Integr. Navig. Syst. ICINS 2017 - Proc.*, pp. 1–3, 2017, doi: 10.23919/ICINS.2017.7995646.

[10] E. J. Ng, C. F. Chiang, Y. Yang, V. A. Hong, C. H. Ahn, and T. W. Kenny, “Ultra-high aspect ratio trenches in single crystal silicon with epitaxial gap tuning,” *2013 Transducers Eurosensors XXVII 17th Int. Conf. Solid-State Sensors, Actuators Microsystems, TRANSDUCERS EUROSENSORS 2013*, vol. c, no. June, pp. 182–185, 2013, doi: 10.1109/Transducers.2013.6626732.

[11] E. N. Pyatishev, Y. B. Enns, A. N. Kazakin, R. V. Kleimanov, A. V. Korshunov, and N. Y. Nikitin, “MEMS GYRO comb-shaped drive with enlarged capacity gradient,” *2017 24th Saint Petersbg. Int. Conf. Integr. Navig. Syst. ICINS 2017 - Proc.*, pp. 1–3, 2017, doi: 10.23919/ICINS.2017.7995647.

[12] D. Galayko, A. Kaiser, L. Buchaillot, B. Legrand, D. Collard, and C. Combi, “Design, realization and testing of micro-mechanical resonators in thick-film silicon technology with postprocess electrode-to-resonator gap reduction,” *J. Micromechanics Microengineering*, vol. 13, no. 1, pp. 134–140, 2003, doi: 10.1088/0960-1317/13/1/319.

[13] C. Acar and A. M. Shkel, “Post-release capacitance enhancement in micromachined devices,” *Proc. IEEE Sensors*, vol. 1, no. July 2014, pp. 268–271, 2004, doi: 10.1109/icsens.2004.1426153.

[14] E. N. Pyatishev, Y. B. Enns, R. V. Kleimanov, I. M. Komarevtsev, and A. N. Kazakin, “Increasing the capacity of micromechanical gyroscope comb actuator using bistable suspension,” *25th Saint Petersbg. Int. Conf. Integr.*

Navig. Syst. ICINS 2018 - Proc., pp. 1–3, 2018, doi: 10.23919/ICINS.2018.8405903.

[15] W. C. Chen, M. H. Li, W. Fang, and S. S. Li, "Realizing deep-submicron gap spacing for CMOS-MEMS resonators with frequency tuning capability via modulated boundary conditions," *Proc. IEEE Int. Conf. Micro Electro Mech. Syst.*, pp. 735–738, 2010, doi: 10.1109/MEMSYS.2010.5442301.

[16] M. Nowack *et al.*, "Micro arc welding for electrode gap reduction of high aspect ratio microstructures," *Sensors Actuators, A Phys.*, vol. 188, pp. 495–502, 2012, doi: 10.1016/j.sna.2011.12.026.

[17] S. R. Kuppireddi and O. Sorasen, "Electrostatic actuation gap reduction method and analysis for square plate resonator on SOI substrates," *2013 Symp. Des. Test, Integr. Packag. MEMS/MOEMS, DTIP 2013*, no. April, pp. 16–19, 2013.

[18] N. Van Toan and T. Ono, "Capacitive silicon resonator structure with movable electrodes to reduce capacitive gap widths based on electrostatic parallel plate actuation," *Proc. IEEE Int. Conf. Micro Electro Mech. Syst.*, vol. 1, pp. 1245–1248, 2014, doi: 10.1109/MEMSYS.2014.6765874.

[19] E. J. Ng *et al.*, "Stable pull-in electrodes for narrow gap actuation," *Proc. IEEE Int. Conf. Micro Electro Mech. Syst.*, pp. 1281–1284, 2014, doi: 10.1109/MEMSYS.2014.6765883.

[20] X. Li, J. Bao, Y. Huang, Y. Ling, Y. Zheng, and Y. Du, "A 9.45 MHz micromechanical disk resonator with movable electrodes for gap reduction," *Sensors Actuators, A Phys.*, vol. 243, pp. 66–70, 2016, doi: 10.1016/j.sna.2016.03.010.

[21] M. Y. Elsayed and F. Nabki, "870 000 Q-Factor Capacitive Lamé Mode Resonator With Gap Closing Electrodes Enabling 4.4 kΩ Equivalent Resistance at 50 V," *IEEE Trans. Ultrason. Ferroelectr. Freq. Control*, vol. 66, no. 4, pp. 717–726, 2019, doi: 10.1109/TUFFC.2019.2892227.

[22] S. Sönmezoğlu, “A HIGH PERFORMANCE AUTOMATIC MODE-MATCHED MEMS GYROSCOPE,” Middle East Technical University, 2012.

[23] K. Azgın, “HIGH PERFORMANCE MEMS GYROSCOPES,” Middle East Technical University, 2007.

[24] E. Tatar, “QUADRATURE ERROR COMPENSATION AND ITS EFFECTS ON THE PERFORMANCE OF FULLY DECOUPLED MEMS GYROSCOPES,” Middle East Technical University, 2010.

[25] S. E. Alper, “MEMS GYROSCOPES FOR TACTICAL-GRADE INERTIAL MEASUREMENT APPLICATIONS,” 2005.

[26] C. Liu, *FOUNDATIONS OF MEMS*. 2012.

[27] R. G. Budynas and J. K. Nisbett, *Shigley's Mechanical Enginering Design*, Ninth Edit. 2011.

[28] H. D. Gavcar, “COMPENSATION METHODS FOR QUASI-STATIC ACCELERATION SENSITIVITY OF MEMS GYROSCOPES,” Middle East Technical University, 2014.

[29] Ki Bang Lee and Young-Ho Cho, “Frequency tuning of a laterally driven microresonator using an electrostatic comb array of linearly varied length,” pp. 113–116, 2002, doi: 10.1109/sensor.1997.613595.

[30] A. Aydemir, “DEEP-TRENCH RIE OPTIMIZATION FOR HIGH PERFORMANCE MEMS MICROSENSORS,” MIDDLE EAST TECHNICAL UNIVERSITY, 2007.

[31] E. Jing, B. Xiong, and Y. Wang, “The bond strength of Au/Si eutectic bonding studied by IR microscope,” *IEEE Trans. Electron. Packag. Manuf.*, vol. 33, no. 1, pp. 31–37, 2010, doi: 10.1109/TEPM.2009.2035307.

[32] Y. C. Lin *et al.*, “Development and evaluation of AuSi eutectic wafer

bonding," *TRANSDUCERS 2009 - 15th Int. Conf. Solid-State Sensors, Actuators Microsystems*, pp. 244–247, 2009, doi: 10.1109/SENSOR.2009.5285519.

[33] D. Li, Z. Shang, Y. She, and Z. Wen, "Investigation of Au/Si eutectic wafer bonding for MEMS accelerometers," *Micromachines*, vol. 8, no. 5, 2017, doi: 10.3390/mi8050158.

[34] M. Haubold, Y. C. Lin, J. Frömel, M. Wiemer, M. Esashi, and T. Geßner, "A novel approach for increasing the strength of an Au/Si eutectic bonded interface on an oxidized silicon surface," *Microsyst. Technol.*, vol. 18, no. 4, pp. 515–521, 2012, doi: 10.1007/s00542-012-1440-1.

[35] "Physik Instrumente N-565 Linear Stage." https://www.physikinstrumente.com/en/products/linear-stages/miniature-linear-stages/n-565-linear-stage-with-the-highest-precision-202999/ (accessed Jan. 09, 2022).

[36] "Physik Instrumente N-565 Linear Stage." .

[37] "Loctite stycast 2850ft." pp. 0–3, 2016.

[38] C. Acar, "Robust Micromachined Vibratory Gyroscopes Automotive :," University of California, Irvine, 2004.

[39] C. Acar and A. M. Shkel, *MEMS Vibratory Gyroscopes*, no. July. 2009.

[40] G. Q. Wu, G. L. Chua, and Y. D. Gu, "A dual-mass fully decoupled MEMS gyroscope with wide bandwidth and high linearity," *Sensors Actuators, A Phys.*, vol. 259, pp. 50–56, 2017, doi: 10.1016/j.sna.2017.03.027.